

DESIGN AND CHARACTERIZATION OF PASSIVE WIRELESS STRAIN SENSOR

by

KE SUN

A thesis submitted in partial fulfillment of the requirements for the degree of

MASTER OF SCIENCE
in
MECHANICAL ENGINEERING

UNIVERSITY OF PUERTO RICO
MAYAGÜEZ CAMPUS
2006

Approved by:

David Serrano, ScD
Member, Graduate Committee

Date

Fredrick A. Just Agosto, PhD
Member, Graduate Committee

Date

Manuel Toledo-Quiñones, PhD
Member, Graduate Committee

Date

Yi Jia, PhD
President, Graduate Committee

Date

Mario Ierkic, PhD
Representative of Graduate Studies

Date

Paul Sundaram, PhD
Chairperson of the Department

Date

ABSTRACT

In order to predict and avoid disasters due to the structure failure, reliable strain information is necessary to be monitored in real time. Existing strain sensing technologies offer outstanding performance in terms of the resolution and time response. However, these technologies require either physical connection of signal communication, battery power supply or expensive equipments for acquiring strain information. These limitations make existing strain sensing technologies unsuitable for structures such as aircraft and vehicle.

A novel passive wireless strain sensor has been developed in this research to overcome the limitations of existing strain sensing technologies. The sensor employs a planar inductor which is series connected to an interdigital capacitor to eliminate the wire connection for power supply and data transmission. The sensor is activated by electromagnetic wave and the resonant frequency of the sensor is interrogated remotely with a single loop antenna by monitoring the frequency response of the voltage across it. The sensor was modeled and the strain effect on resonant frequency of the sensor was investigated. The prototype sensor and the rudiment of a hand-held reader circuit were designed and fabricated. By carrying out an efficient and systematic multi-objective optimization method, the sensor geometric size can be minimized, and strain sensitivity, quality factor and reading distance can be maximized. Experiments for measuring the dielectric permittivity of piezoelectric polymer based on micro-strip transmission line theory were carried out in order to study its strain dependent dielectric permittivity and possibility of strain sensing enhancement. A very friendly graphic interface for real-time data display was programmed in MATLAB. The results of sensor calibration on a cantilever beam with

position-independent surface strain showed a great linearity and sensitivity. The innovative wireless strain sensing technology presented has demonstrated a great potential to extend its applications in structural health monitoring, damage detection, condition-based maintenance, failure prevention and non-destructive evaluation.

RESUMEN

Para predecir y evitar desastres debido a fallos en estructuras, es necesario monitorear en un tiempo real recursos de información confiables sobre la deformación. Tecnologías ya existentes sobre la detección de la tensión, ofrecen un desempeño sobresaliente en términos de resolución y tiempo de respuesta se refiere. Aun así, estas tecnologías requieren ya sea de una conexión física, comunicación por señales, ser abastecidas por el poder de alguna batería o de equipo costoso para poder obtener información sobre la deformación. Estas limitaciones hacen que las tecnologías ya existentes para obtener información sobre la tensión no sean aptas para estructuras como aeronaves o vehículos.

En este proyecto se desarrolló una nueva tecnología para la detección de la tensión y así superar las limitaciones que encontramos en los detectores de tensión, ya existentes. Este proyecto se desarrolló luego de haberse llevado a cabo una vasta y amplia revisión literaria. El detector emplea un inductor planar, el cual está conectado en serie a un capacitor interdigital para así eliminar la conexión de cables al suplidor de poder y transmisor de la data. El sensor es activado por ondas electromagnéticas y la frecuencia resonante del sensor es controlada remotamente con una antena de una curva, mediante el monitoreo de la respuestas de frecuencia del voltmetro a través de ella. El sensor fue modelado y se investigó el efecto de la tensión en la resonancia de frecuencia del sensor fue investigada. El sensor prototipo y el rudimento del lector de circuito de mano fueron diseñados y fabricados. Llevando a cabo un método de optimización eficiente y a su vez sistemático y con múltiples objetivos, el tamaño geométrico del sensor se puede minimizar y a su vez se puede maximizar la sensibilidad de la tensión así como el factor de calidad y la distancia de la

lectura. Se estudió la permitividad dieléctrica de la dependencia de deformación en el polimero piezoelectric (PVDF). Se llevaron a cabo experimentos para medir la permitividad dieléctrica basados en la teoría de líneas de transmisión de micro strips. Se creó una interfaz amigable para comunicarse con el circuito y para que los datos fueran interpretados en tiempo real por medio de MATLAB. Los resultados de la calibración en una viga voladiza con la tensión superficial de posición-independiente demostraron grandes linealidades y sensibilidad. La innovadora tecnología inalámbrica en sensores de tensión descrita a demostrado un gran potencial al extender sus aplicaciones al monitoreo de la condición estructural, detección de daños, mantenimiento de acuerdo a las condiciones, prevención de fallas y evaluaciones no destructivas.

To my parents

ACKNOWLEDGEMENTS

I am deeply indebted to many people who helped me pursuing and finishing this research. Initially, I would like to thank my thesis adviser, Professor Yi Jia, who gave me the opportunity to join his group in the August of 2004. I am grateful for having been offered a chance to gain direct engineering knowledge and apply my physical intuition by joining a research group where the focus is the development of novel sensors. I also feel grateful for his continuous support and encouragement that helped me overcome the disappointments that are so abundant in any experimental and theoretical problem. Finally, I must thank him for our numerous discussions on a variety of scientific, engineering, cultural, and political subjects which augmented my vision and understanding.

I would like to thank Dr. Fredrick Just for providing the equipments of the Laboratory for the experimental part of my thesis. I would like to express my special thanks to him for being a good patient teacher to explain control problems during the time I was working as a teach-assistant in his class. I would like to thank Dr. Serrano for his supportive encouragements as a member of my graduate committee. I also would like to express my thanks to Dr. Toledo-Quiñones for his explanation on the reader design.

I would also like to thank my family. Their love and understanding helped me through the most difficult time of this work.

The Grant from NSF 0549338 provided the funding and the resources for the development of this research.

Table of Contents

ABSTRACT.....	II
RESUMEN	IV
ACKNOWLEDGEMENTS.....	VII
TABLE OF CONTENTS	VIII
LIST OF TABLES.....	XI
LIST OF FIGURES.....	XII
NOMENCLATURE	XIV
1 INTRODUCTION.....	1
1.1 ENGINEERING STRAIN-STRESS RELATIONSHIP.....	1
1.1.1 <i>Tensile Stress and Strain</i>	1
1.1.2 <i>Compressional Stress and Strain</i>	2
1.1.3 <i>Shear Stress and Strain</i>	3
1.2 PROPOSED STRAIN SENSING SYSTEM.....	3
1.3 THESIS OVERVIEW	6
1.3.1 <i>Research Objectives</i>	6
1.3.2 <i>Thesis Organization</i>	7
2 LITERATURE REVIEW	9
2.1 PIEZO-RESISTIVE STRAIN SENSOR.....	9
2.1.1 <i>Metallic Wire/Foil Gauge</i>	10
2.1.2 <i>Piezoresistive Film Gauge</i>	11
2.1.3 <i>Semiconductor (silicon) Strain Gauge</i>	12
2.2 PIEZO-ELECTRIC STRAIN SENSOR	13
2.2.1 <i>Capacitance Strain Sensor</i>	13
2.2.2 <i>Acoustic Wave Strain Sensor</i>	15
2.2.3 <i>Piezoelectric Strain Sensor</i>	16
2.3 PIEZO-MAGNETIC STRAIN SENSOR.....	16
2.3.1 <i>Inductance Strain Sensor</i>	17
2.3.2 <i>Piezomagnetic Strain Sensor</i>	18
2.4 PIEZO-RESONANT STRAIN SENSOR.....	19
2.4.1 <i>Nanowire Strain Sensor</i>	19
2.4.2 <i>Cavity Strain Sensor</i>	20
2.5 PIEZO-OPTICAL STRAIN SENSOR.....	21
2.5.1 <i>Fiber Optic Strain Sensor</i>	21
2.5.2 <i>Optical Surface Strain Image</i>	25
2.6 DISCUSSIONS.....	28
3 INTERDIGITAL CAPACITOR.....	30
3.1 INTERDIGITAL CAPACITANCE ANALYSIS	30
3.1.1 <i>Approximation Model</i>	30
3.1.2 <i>Analysis Approaches</i>	32
3.1.3 <i>IDC Model</i>	34

3.1.4	<i>Geometry Dependent Capacitance</i>	37
3.1.5	<i>Strain Dependent Capacitance</i>	39
3.2	DISCUSSIONS	44
4	PLANAR SPIRAL INDUCTOR	46
4.1	INDUCTIVE POWERING	46
4.1.1	<i>Introduction</i>	46
4.1.2	<i>Inductive Powering</i>	49
4.2	PLANAR SPIRAL INDUCTOR.....	53
4.2.1	<i>Inductance Approximation</i>	53
4.2.2	<i>Strain Effect on Inductance</i>	57
4.3	OPTIMIZATION OF SENSOR DESIGN	59
4.3.1	<i>Optimization of Inductive Powering</i>	60
4.3.2	<i>Consideration on Strain Sensing</i>	67
4.3.3	<i>Multi-objective Optimization</i>	69
4.3.4	<i>Design Results and Discussions</i>	71
5	SENSITIVITY ENHANCMENT	74
5.1	STRAIN-DEPENDENT PERMITTIVITY	74
5.2	EXPERIMENT INVESTIGATION	79
6	SENSOR FABRICATION	84
6.1	PATTERN DESIGN	84
6.2	MATERIALS	85
6.3	SENSOR FABRICATION	86
7	SENSOR READER DESIGN	91
7.1	POWER SUPPLY	91
7.2	TRANSMITTER	92
7.3	RECEIVER	93
7.4	DATA ACQUISITION AND DISPLAY	94
8	SENSOR CHARACTERIZATIONS	96
8.1	LOADING SYSTEM SETUP	96
8.1.1	<i>Beam Bending Behavior</i>	96
8.1.2	<i>Beam Design</i>	97
8.1.3	<i>Bending Test Setup</i>	98
8.2	SENSOR PERFORMANCES CHARACTERIZATION.....	100
8.2.1	<i>Distance and Angle vs. Resonant Frequency</i>	100
8.2.2	<i>Strain vs. Resonant Frequency</i>	101
8.2.3	<i>Environment Related Effects</i>	103
9	CONCLUSIONS REMARKINGS	104
9.1	BRIEF THESIS SUMMARY	104
9.2	RESEARCH CONTRIBUTIONS.....	105
9.3	FUTURE WORKS AND RECOMMENDATIONS	107
	REFERENCES	109
	APPENDIX A. PROGRAM FOR PERMITTIVITY CALCULATION	113

APPENDIX B	PROGRAMS FOR SENSOR OPTIMIZATION	115
APPENDIX C	PROGRAMS FOR DATA DISPLAY INTERFACE.....	117
APPENDIX D	CIRCUIT DIAGRAM OF READER.....	123

List of Tables

Tables	Page
TABLE 2.1 Gauge factors $[(\Delta R/R)/\epsilon]$ for piezoresistive strain-gauge materials	13
TABLE 4.1 Optimal design results for maximizing the power on sensor.....	63
TABLE 4.2 Optimal design results for maximizing the power on sensor.....	63
TABLE 4.3 Optimal design results for maximizing the Q -factor on PSI.....	66
TABLE 4.4 Optimal design results for minimizing sensor dimension.....	68
TABLE 4.5 Multi-objective optimization sample results.....	72
TABLE 6.1 Single-sided Pyralux AC product offerings.....	86
TABLE 6.2 Pyralux AC materials properties.....	86

List of Figures

Figures	Page
Figure 1.1 Tensile stress and strain.....	2
Figure 1.2 Compressional stress and strain.....	2
Figure 1.3 Shear stress and strain.	3
Figure 1.4 A schematic of proposed passive wireless strain sensor.	4
Figure 1.5 An embodiment of an LC measurement system.....	5
Figure 1.6 Frequency response of the impedance across the reader antenna.	5
Figure 2.1 Fundamental of strain sensing principle.....	9
Figure 2.2 Wire/foil strain gauge.....	10
Figure 2.3 Thick film (left) [3] and thin film (right) [5] piezoresistive strain gauge.	12
Figure 2.4 Differential capacitance readout strain sensor [14, 15].	14
Figure 2.5 Schematic principle of SAWs wireless strain sensor.	15
Figure 2.6 Basic structure of piezoelectric strain sensor.	16
Figure 2.7 Solenoid inductive sensor and wireless reading [11].	17
Figure 2.8 Schematic of the magnetoelastic sensor [13].	18
Figure 2.9 Diagram and photograph of resonator construction [16].	20
Figure 2.10 A schematic of FOBG sensing concept [17].	22
Figure 2.11 Typical EFPI sensor [19].	23
Figure 2.12 Conventional (left) and Stabilized (right) EFI fiber optic strain sensor [20].	23
Figure 2.13 3-dimensional DIC surface strain measurement system [28].	26
Figure 2.14 Schematic diagram of basic LPC instrumentation.	27
Figure 3.1 A schematic view of the interdigital capacitor simplification.....	31
Figure 3.2 A half unit cell model of the proposed multilayer interdigital capacitor.	35
Figure 3.3 The equivalent circuit of the multilayer interdigital capacitor.	35
Figure 3.4 Splitting of the proposed four-layered IDC [34].	36
Figure 3.5 Capacitance as a function of l - η and r	38
Figure 3.6 Three possible positions of the IDC on the bending beam.....	39
Figure 3.7 Strain effects on the capacitance value of IDC in parallel configuration with $\lambda=400\mu\text{m}$, $\eta=0.9$, $l_C=40$ mm, and $N_C=40$	41
Figure 3.8 Strain effects on the capacitance value of IDC in perpendicular configuration with $\lambda=400\mu\text{m}$, $\eta=0.9$, $l_C=40$ mm, and $N_C=40$	42
Figure 3.9 Strain effects on the capacitance value of IDC in the random angle configuration with $\lambda=400\mu\text{m}$, $\eta=0.9$, $l_C=40$ mm, and $N_C=40$	42
Figure 3.10 The capacitance change vs. η and r	45
Figure 4.1 Equivalent diagram for magnetically coupled reader coil and sensor.....	49
Figure 4.2 Equivalent circuit diagram of the inductively coupled reader and sensor.....	51
Figure 4.3 Frequency response of the voltage on the reader antenna coil with sensor.....	53
Figure 4.4 Layout of four turns square spiral inductor.	54
Figure 4.5 Calculated inductances vs. varying fill ratio ρ at $d_{avg}=61$ mm.	56

Figure 4.6 Comparison of calculated inductances with varying d_{avg} at $\rho=0.3$	56
Figure 4.7 PSI deformation on bending beam a) before and b) after deformation.	58
Figure 4.8 Strain effects on the inductance value of PSI with $w_L=1000\mu\text{m}$, $g_L=1000\mu\text{m}$, $d_{out}=78\text{ mm}$, and $N_L=8$	59
Figure 4.9 Magnetic field strength vs. distance with $I_I=0.16\text{ A/m}$ at $N_R=1$	61
Figure 4.10 Q versus w_L at $N_L = 4.5321$ and versus N_L at $w_L = 741.6971\mu\text{m}$ with $d_{in} =$ 32.9177mm and $g_L = 50\mu\text{m}$	66
Figure 4.11 Schematic of a preference-based multi-objective optimization procedure.	69
Figure 5.1 Tensor directions.	75
Figure 5.2 Transmission line test fixtures.....	81
Figure 5.3 Experimental Setup.	82
Figure 5.4 The variation of the dielectric constant with the increasing temperature.....	82
Figure 5.5 The variation of the dielectric constant with the increasing stress.....	83
Figure 6.1 Sensor prototype patterns.	85
Figure 6.2 Illustration on the sensor fabrication using photolithography.	89
Figure 6.3 Fabricated sensor prototypes.	90
Figure 7.1 Fabricated power supply circuit.	92
Figure 7.2 Prototype of the transmitter circuit.....	93
Figure 7.3 The output signal of the Miller integrator.	94
Figure 7.4 Fabricated current and voltage amplifier circuit with coil antenna.....	94
Figure 7.5 Data acquisition board.....	95
Figure 7.6 Data display interface programmed in MATLAB.....	95
Figure 8.1 Test beam design.	98
Figure 8.2 White Derlin beam with position independent surface strain.	98
Figure 8.3 Sensor calibration setup.....	99
Figure 8.4 Sensor calibration setup.....	99
Figure 8.5 Sketch for distance and resonant frequency investigation.	100
Figure 8.6 Distance vs. resonant frequency.....	100
Figure 8.7 Sketch for angle and resonant frequency investigation.	101
Figure 8.8 Angle vs. resonant frequency.	101
Figure 8.9 Frequency shift vs. surface strain with sensor at parallel direction.....	102
Figure 8.10 Frequency shift vs. surface strain with sensor at perpendicular direction.....	102
Figure 8.11 Frequency shift vs. surface strain with sensor at 45°	103

NOMENCLATURE

Symbol	Unit	Name
a	Meter	Wire radius of loop coil
A	Meter ²	Area
c	Meter	Distance from neutral axis to beam surface
C	Farad	Capacitance
d	Meter	Diameter of loop coil
e	GPa	Young's modulus
E	Volts per Meter	Electrical field strength
f	Hertz	Frequency
F	Newton	Force
g	Meter	Width of air gap
G	Meter Newton	Bending moment
h	Meter	Thickness
H	Ampere per Meter	Magnetic field strength
I	Ampere	Electrical current
j	-	Complex operator
J	Meter ⁴	Moment of inertial of beam cross-section
k	-	Coupling coefficient
K	-	Constant coefficient
l	Meter	Length
L	Henry	Inductance
M	Henry	Mutual inductance
N	-	Number of turns or electrodes
p	Watt	Power
P	Coulomb meter	Polarization
Q	-	Quality factor
R	Ohm	Resistance
r	-	Thickness over the wavelength of IDC
S	Joule per kelvin	Entropy per unit volume
T	Second	Period
V	Volt	Electrical voltage
v	Meter per Second	Speed
w	Meter	Width
x	Meter	Distance
Y	Meter ³	Section modulus of beam
Z	Ohm	Impedance
α	Coulombs per meter	Charge density
β	-	Phase constant
δ	Neper per meter	Dielectric losses
ε	Farad per Meter	Dielectric permittivity

Symbol	Unit	Name
Ψ	Weber	Total magnetic flux
γ	-	Complex propagation constant
η	-	Metal ratio
Φ	Joule	Thermodynamic potential per unit volume
Φ_B	Weber	Magnetic flux
λ	Meter	Spatial wavelength
μ_0	Henrys per Meter	Free space magnetic conductivity
ω	Hertz	Angular Frequency
ρ	-	Fill ratio of PSI
τ	-	Strain
σ	Newton per Meter ²	Stress

1 INTRODUCTION

Strain-stress relationships can determine very important physical quantities in engineering, such as axial forces, bending moment, torque, pressure, acceleration, and temperature. To practically assess the stress state in a specimen, strain must be measured. The motivation of the research is to develop a strain sensor, which could provide a passive detection and wireless communication at a low cost for long term strain measurement. In this chapter, we start with the basic engineering strain-stress relationships, an overview on this project and then the organization of the thesis.

1.1 Engineering Strain-Stress Relationship

Strain is known as the change of the shape or geometry produced by applied loads. The loads are defined by the general term stress. Instead of getting deep to the inside of the deformed material, the stress and strain this part will be seeing from the engineer's point of view based on the analysis of the common phenomenon in mechanical deformations. Three most basic types of stress and strain will be delineated.

1.1.1 Tensile Stress and Strain

Tensile force is shown in Figure 1.1 as a load applied to a sample of material so as to elongate or pull apart the sample. In this case, the stress is defined as

$$\text{Tensile stress} = F/A \qquad 1.1$$

where F is the applied force in N and A is the cross-sectional area of the sample in m^2 . The unit of stress is N/m^2 (Pa) in SI unit.

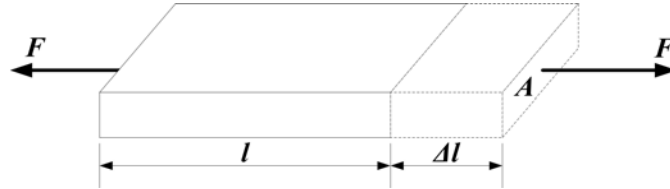


Figure 1.1 Tensile stress and strain

The strain in this case is defined as the fractional change in length of the sample

$$\text{Tensile strain} = \Delta l / l \quad 1.2$$

where Δl is the change length and l is the original length of the sample in m. Always strain is thus a unitless quantity.

1.1.2 Compressional Stress and Strain

As shown in Figure 1.2. The compressional stress is defined similarly as tensile stress

$$\text{Compressional stress} = F / A \quad 1.3$$

where F is the compressional force in N and A is the cross-sectional area of the sample in m^2 .

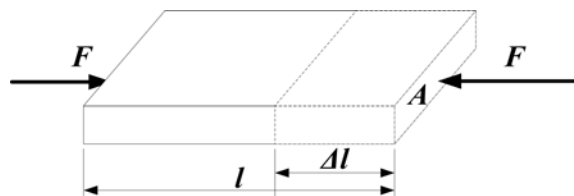


Figure 1.2 Compressional stress and strain

The resulting strain is also defined as the fractional change in length as

$$\text{Compressional strain} = \Delta l / l \quad 1.4$$

where Δl is the change in length and l is the original length of the sample in m.

1.1.3 Shear Stress and Strain

Figure 1.3.a) shows the nature of the shear stress. In this case, the force is applied as a couple not along the same line, tending to shear off the sample that separates the force arms. The stress is again

$$\text{Shear stress} = F/A \quad 1.5$$

where F is the Shear force in N and A is the cross-sectional area of the sample in m^2 .

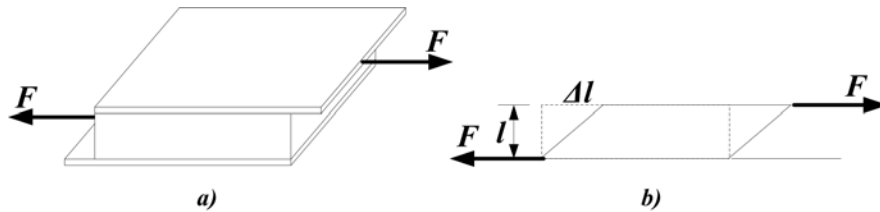


Figure 1.3 Shear stress and strain.

The shear strain in this case is defined as the fractional change in dimension of the sheared sample. The shear strain is shown by taking a cross-sectional view on the sample shown in Figure 1.3 b).

$$\text{Shear strain} = \Delta l/l \quad 1.6$$

where Δl is the change in length in m and l is the width of the sample in m.

1.2 Proposed Strain Sensing System

A novel passive wireless sensor to be developed for strain monitoring is an interdigital capacitor with a series-connected planar spiral inductor. These two components work together as an LC resonator whose resonant frequency is designed to change correspondingly with a change in the strain state that the sensor measures. The interdigital

capacitor (IDC) and the planar spiral inductor (PSI) are prepared on a thick flexible Pyralux from DuPont (Figure 1.4).

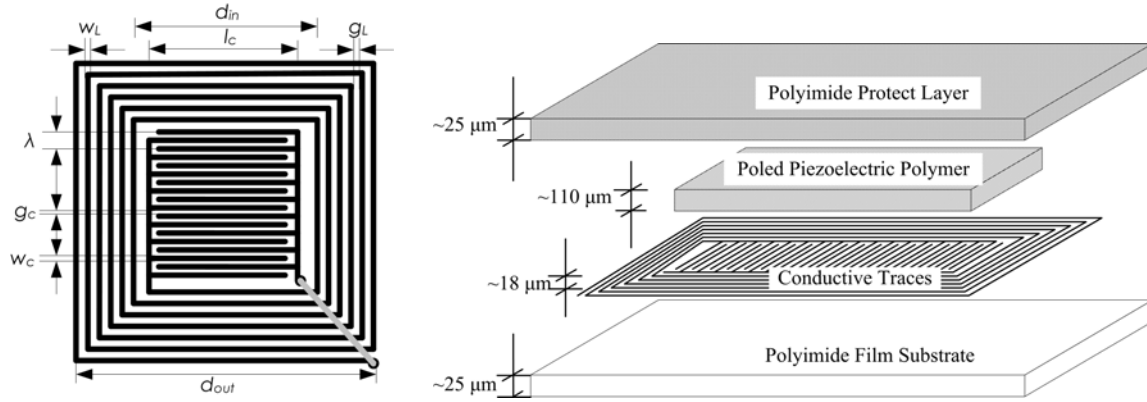


Figure 1.4 A schematic of proposed passive wireless strain sensor.

In Figure 1.4, eight geometric variables of the sensor are identified. The multi-layered structure of the sensor is also shown in the figure with the substrate and sensitive enhancement piezoelectric polymer above the conductive side of the interdigital capacitor.

The sensor can be attached to any kind of material, and it is easy to embed into non-conductive material especially in laminated or dielectric materials. The frequency response of the sensor is remotely detected by monitoring the impedance across the terminals of the wide bandwidth reader antenna which actually also plays the role as a power transmitter by sending out oscillating magnetic field. A schematic view of the entire sensing system is shown in Figure 1.5.

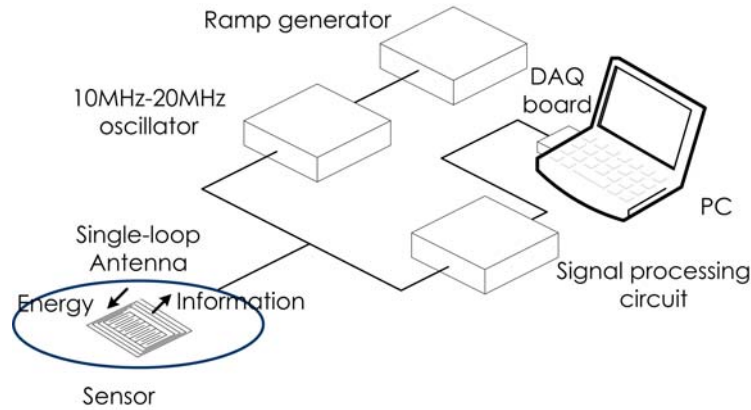


Figure 1.5 An embodiment of an LC measurement system.

The resonant frequency will be changed with the strain-dependent interdigital capacitance due to the geometry distortion of the electrodes induced by the geometric deformation of the material under test. The strain sensitivity can be enhanced with additional piezoelectric polymers attached to the conductive side of the sensor. The dielectric properties of the piezoelectric polymer, which plays another important contribution on the change of the capacitance, are altered because of the polarization established in the polymer once the polymer is exposed to the strain field.

Figure 1.6 is a sketch of the measured impedance spectra from the sensor antenna at different self-resistance (R_S) of the sensor.

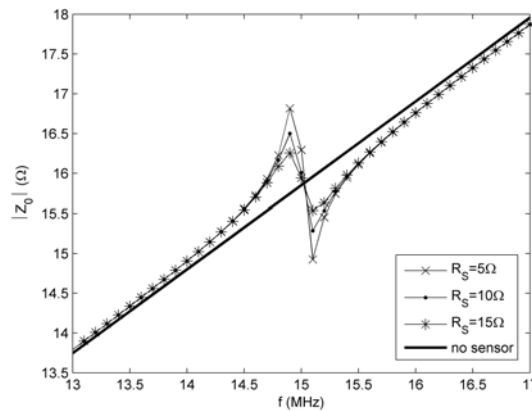


Figure 1.6 Frequency response of the impedance across the reader antenna.

The resonant frequency of the sensor is defined as the point where a sudden change appears in the frequency response of the impedance. This resonant frequency is changed when the sensor is exposed to the strain field.

The advantage of this method is that the sensor can be non-obtrusively added to the structures or systems for which it is being used and monitored. Meanwhile, no physical connections for power supply or data acquisition is required. Other advantages of this method include:

- (1) No line of sight being required between the reader antenna and the sensor;
- (2) The ability of the entire sensor to be embedded in a nonconductive material;
- (3) The ability to embed the capacitive element in a conducting material with the inductive element being placed away from the surface of the conductive material;
- (4) No additional antenna is required except that the sensor and the antenna are in 90 degrees, and
- (5) No wire is required to add new sensors.

1.3 Thesis Overview

1.3.1 Research Objectives

The primary objective of the proposed project is to conduct basic research into the strain sensing mechanism of the proposed passive wireless sensor in order to develop a novel strain microsensor and to fabricate associated electronics for remote power and wireless data acquisition.

Specifically, the proposed project:

- Investigated and modeled the strain effect on the sensor;
- Designed and fabricated prototypes of proposed sensors and sensor reader;
- Tested the strain sensitive material (PVDF film);
- Characterized and calibrated the sensor performance.

To fulfill these objectives, the sensor was carefully architected and prototyped, and data acquisition and processing circuit for sensor system were designed and fabricated. The programmings to facilitate the sensor geometric optimization and extract the strain information by the analyzing of the frequency signal were also developed in MATLAB.

1.3.2 Thesis Organization

The existing strain sensing technologies will be widely reviewed in Chapter 2. Modern techniques involved in strain sensing will be compared with sensing principles and various applications. In Chapter 3, strain sensing mechanism in interdigital electrodes will be explored. Design considerations of interdigital capacitor will be discussed and simulated by analyzing all the contribution of geometry properties to the change of the capacitance. Chapter 4 concentrates on planar spiral inductor. The design of the antenna will be simulated and the working performance together with the interdigital capacitor, such as quality factor, resonant frequency, etc. will be optimized by carrying out nonlinear multi-objective geometric optimization. After this, strain sensitive coating material will be investigated and the sensor performance with the coating applied will be studied in Chapter 5. Chapter 6 describes the sensor fabrication with basic MEMS techniques. Design of the hand-held sensor reader with the ability to activate the sensor and measure the strain dependent resonant

frequency remotely will be dedicated in Chapter 7. Experimental setup and sensor characterization will be discussed in Chapter 8. Finally, this work will conclude with a discussion of the thesis contributions and future work on the possibility of the improvements in Chapter 9. Developed programming codes in MATLAB and circuit diagrams will be shown in Appendixes.

2 LITERATURE REVIEW

Strain sensing technology has become one of the most critical areas required for structural health monitoring (SHM), damage detection, condition-based maintenance, failure prevention and non-destructive evaluation, because strain is one of the key performance parameters that affects the life of mechanical components and civil structures. Stress, fatigue strength, material internal damage and load-history of structure, can be interpreted from strain information. Strain sensors can be classified in various ways, contact and non-contact, wire and cordless, passive and active, absolute and relative, etc, depending on the classification purpose. This review is organized according to how the strain effects are converted into other signals which can be processed (Figure 2.1). Strain sensors are divided into piezo-resistive, piezo-electric, piezo-magnetic, piezo-resonant and piezo-optic strain sensors. The purpose of this chapter is to outline the newly developed technologies of strain sensing in the last fifteen years. Advantages of our proposed sensor will be highlighted.

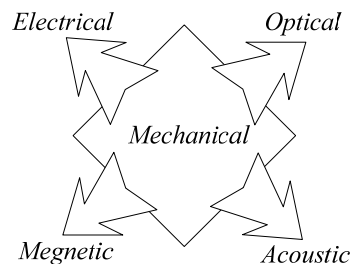


Figure 2.1 Fundamental of strain sensing principle.

2.1 Piezo-resistive Strain Sensor

Piezo-resistance is known as a phenomenon that the electrical resistances of the elements or the materials are changed when they are mechanically deformed. In this way, by

measuring the resistance, the strain on the elements or materials can be determined. Piezo-resistive sensor, the most commonly used strain sensor, comes in many different types designed for working in different temperature ranges with various sizes and accuracies.

2.1.1 *Metallic Wire/Foil Gauge*

After nearly 70 years of the found of metallic wire/foil gauge principle, application in measurement has been widely spread for sensing dynamometric quantities or geometric quantities. Although some arising and promising technologies are merged to the market, still about 50% of all the sensors rely on the strain gauge principle [1]: the change of the electrical resistance of the foil wire is proportional to the applied strain. Comparing to the fragility and high cost of optical strain sensor, and complexity and high requirement of the capacitance and inductance strain sensor, metallic foil wire strain gauges make us enjoy the benefits of low cost, easily configuration, simple measurement circuits and etc.

Typically, the metallic wire/foil gauge consists of a very fine wire or metallic foil, mounted on a resin backing film called carrier. The applied load results in the change of the gauge length and the corresponding strain is measured in terms of the electrical resistance of the wire/foil, which varies linearly with strain.

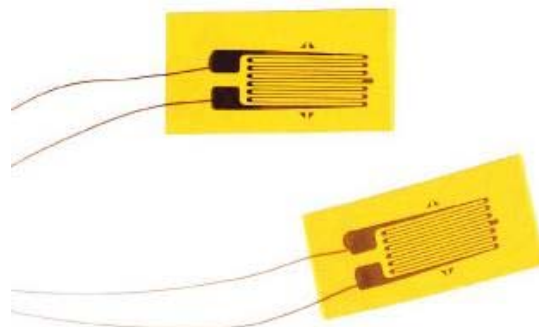


Figure 2.2 Wire/foil strain gauge.

Common strain gauge has relatively low gauge factor which ranges from 2 to 6, a nominal resistance values from 30 to 3000 Ω , and shows temperature dependent gauge factor and resistance as well. The hysteresis of the adhesive material between the sensor gauge and the object limits the application of the strain sensor for high accuracy requirement applications. Therefore, three primary design considerations for the success of applications are working temperature, the nature of the strain to be detected, and the stability requirements.

2.1.2 Piezoresistive Film Gauge

Piezoresistive film gauges have been quickly expanded their share to make the transverse strain exactly from the underlying object to the strain gauge. The effect of bulk resistivity change in some elastic materials when they are subjected to deformation was noticed 30 years ago. The gauge factor is much increased primarily by the piezoresistive effect in piezoresistive film gauge instead of the geometry effect ($\Delta L/L$) in foil/wire gauges. The piezoresistive effect is not only referred to the change of the resistance with deformation but deeply defined as the change of the bulk resistivity ($\Delta\rho/\rho$) in the material. For metal foil gauge, the gauge factor is about 2 and the geometry effect contributes around 1.6 to the total. We can see the geometry factor is the major contribution to the sensitivity of the foil/wire strain gauge. The gauge factor in piezoresistive thick film gauge is about 10 with a geometric factor less than 1.4. Greater gauge factor up to 100 can be realized by adding various metal oxides into the thick film resistor materials. Moreover, elimination of solder joints and mechanical connections improves reliability and quality compared to foil/wire strain gauges.

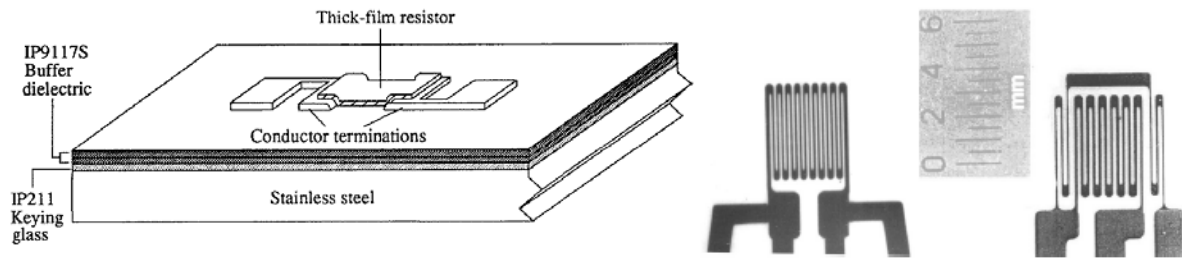


Figure 2.3 Thick film (left) [3] and thin film (right) [5] piezoresistive strain gauge.

Normally, thick films can handle higher voltage and higher current than thin films. Besides, thick films are relatively inexpensive even depositing expensive precious metals. On the other hand, thick films technology is more difficult to automate and the resolution and accuracy of thick film sensors are less attractive than thin film technology.

2.1.3 *Semiconductor (silicon) Strain Gauge*

Piezoresistance effect of germanium and silicon was discovered at Bell Telephone Laboratories in the early 1950's. These semiconductor-based strain gauges exhibit much larger resistance changes than their metallic counterparts. This large effect of strain in the electrical properties occurs because strain changes the electronic energy band structure of silicon without significant alteration of the shapes of the silicon crystal. Strain that decreases the energy of the electrons and valleys in the direction of current flow decreases the resistance in that direction.

In spite of the larger strain sensitivities, the widespread use of silicon gauges has been limited, due, mainly, to the large TCR. An alternative method for minimization of the thermally-induced apparent strain is developed by Hany R. Tamim et al in 1991 [8].

Although the polysilicon strain gauge shows a poor strain gauge factor, it is still attractive with their low temperature dependence.

TABLE 2.1 Gauge factors $[(\Delta R/R)/\epsilon]$ for piezoresistive strain-gauge materials

Sensing Material	Gauge Factor
Metal foil [1]	1~2
Metal oxide thick film [3]	10
Modified oxide thick film [2]	100
Ni-Ag alloy thin film [4]	2.2~2.4
Pd-Cr alloy thin film [6]	1.3
Multilayer alloy thin film [7]	3
Polysilicon [31]	13~15
Silicon [30]	40~200

2.2 Piezo-Electric Strain Sensor

Piezo-electric here used to describe another kind of strain sensor operating based on the phenomenon that electric charges are changed or generated with the applied strain, which are also the fundamental that is used to catalog this strain sensor into two major kinds: one is based on a capacitance elements and the other is based on piezoelectric materials.

2.2.1 *Capacitance Strain Sensor*

There are hundreds of variations of capacitance sensors in use today, which are all based on the concept of charge transference sensing. Simply, by varying the dielectric properties of the material and the geometric properties of the electrodes during the applied strain, transference of the charge on the electrodes can be measured and consequently the strain can be decided.

Capacitive MEMS strain sensors consist of three amplifying buckled beams with comb fingers positioned at the structural center for sensitivity improvement. They are described by Suster et al [10]. The generated differential capacitance readout is due to the change in the overlap area instead of the distance between electrodes [9] (Figure 2.4).

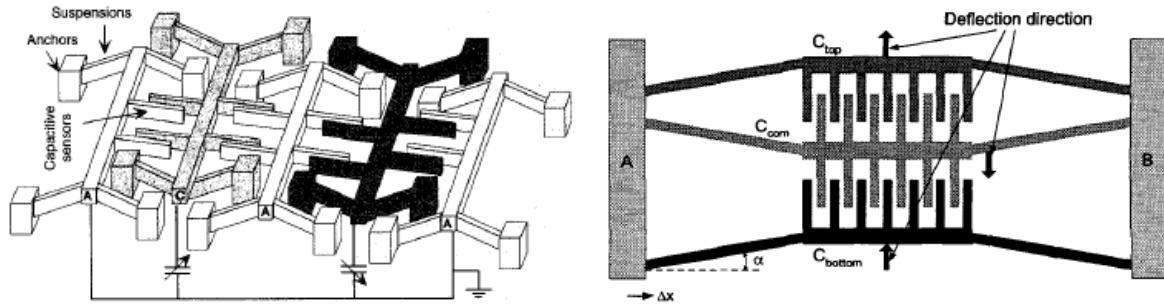


Figure 2.4 Differential capacitance readout strain sensor [14, 15].

As discussed in previous section of piezo-resistive strain sensor, it is known that the conventional strain sensors made of metal foils and semiconductor piezoresistive elements suffers from a large temperature dependence, turn-on drift, poor time stability and limited sensitivity, thus inadequate for high-performance applications. Although it is shown that piezo-resonant and piezo-optical strain sensors are demonstrated to achieve a high performance by converting an input strain to a change in the device resonant frequency or optical signal, they are undesirable for low voltage and low power integrated systems and relatively high cost. MEMS capacitive strain sensors are attractive due to the higher sensitivity, minimum temperature dependence and turn-on drift, low noise, large dynamic range, potential integration abilities, and low cost, which make capacitive strain sensors widely used in harsh environment and microsystems.

2.2.2 Acoustic Wave Strain Sensor

The simplest type of SAW strain sensor, illustrated in Figure 2.5, consists of two interdigital transducers working as resonators or delay lines on a piezoelectric substrate. Consequently, the voltage applied to the left IDTs causes electric field in the gaps between the electrodes. The piezoelectric effect couples these fields to mechanical stresses which act as sources of SAWs, and the SAWs travel out of the transducer. At the output transducer on the right, the field associated with the incident wave induces voltage on the electrodes, and hence a corresponding voltage appears on the output electrodes. Strain effect in the deformed substrate that changes the SAW characteristics by varying the acoustic line can be measured.

For a wide variety of sensor applications, a fixed wired connection between the sensor and the evaluation unit can not be established. Usage of slip-rings and brushes, however, cause additional mechanical and electrical problems (i.e., interruptions, noise, etc.), making these methods unusable in reliable systems. In last ten years, passive SAW devices working on the wireless sensing are published firstly as radio sensors for its store of the energy of RF radio signals. For radio sensor applications, the SAWs devices electrically connected to an antenna, instead of an AC excitation, to realize a wireless strain sensing (Figure 2.5).

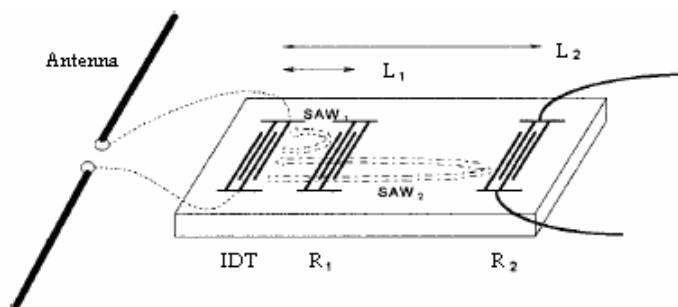


Figure 2.5 Schematic principle of SAWs wireless strain sensor.

2.2.3 Piezoelectric Strain Sensor

Fundamental principles, constitutive equations and standards of piezoelectric materials were discussed in [16-19]. Basically, the piezoelectric strain sensor is constructed with a sheet of piezoelectric material and two electrodes at each side of it. Typical construction of piezoelectric strain sensor is sketched in Figure 2.6. Strain affects the charge value on the top and bottom electrodes and then makes an electric output from the lead wire.

Compared to other commercialized strain sensors, piezoelectric strain sensors have some critical advantages: wide dynamic range which makes piezoelectric strain sensor in highly vibrating structures, free of noise, linearity, wide frequency range even some high frequency, long service life, no external power which makes piezoelectric strain sensor been used as powerless and passive sensing elements, etc. On the other hand, since piezoelectricity always comes with pyroelectricity, which is one of the most important drawbacks of the piezoelectric sensor because of the temperature dependency of piezoelectric materials.

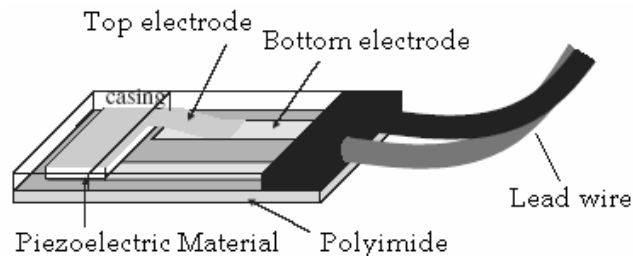


Figure 2.6 Basic structure of piezoelectric strain sensor.

2.3 Piezo-Magnetic Strain Sensor

Piezo-magnetic strain sensor here used to describe another kind of sensor operating based on the phenomenon that magnetic field are changed or generated with the applied

strain. Basically, piezo-magnetic sensors can be cataloged into two major types: one is based on an inductance element and the other is based on piezomagnetic materials.

2.3.1 Inductance Strain Sensor

Inductance strain sensor operates under the most common electrical principle of inductance. Generally, the inductive strain sensor consists of a coreless, hollow, multi-turn inductor whose termini are soldered to a fixed bulk capacitor so as to form an LC resonator. When the strain applied is changed, the area of the enclosed cross section or the effective length of the solenoid is geometrically changed, which leads a variation in the value of inductance and consequently the resonant frequency is shifted. A solenoid sensor and wireless detecting system based on this principle are illustrated in Figure 2.7.

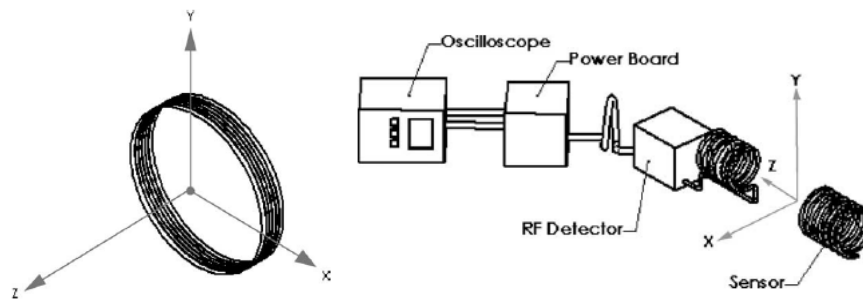


Figure 2.7 Solenoid inductive sensor and wireless reading [11].

The influences of temperature, humidity and pressure are non-negligible for inductive strain sensors based on LC resonant circuits, since the temperature influences the inductance by changing the wire length and the resistance of the wire, the pressure alters the electrical relative permittivity of the capacitance, all of which will definitely change the resonant frequency of the circuit. Hence, necessary corrections are critical to get accurate

measurement. However, this element offers a possibility of remote sensing and wireless reading by inductive coupling.

2.3.2 Piezomagnetic Strain Sensor

Piezomagnetic effect is a linear magnetomechanical effect analogous to the linear electromechanical effect in piezoelectric materials. Generally, piezomagnetic and magnetostriction effects occurs in most of ferromagnetic materials analogous to piezoelectric and electrostriction in most of the ferroelectric materials [12].

Since magnetic flux is generated when it is deformed and detected remotely, a magnetism-based remote strain query sensor is proposed by Dimitris et al in 2000 [13]. Typical measurement setup is shown in Figure 2.8. The strain can be wirelessly detected by sending an interrogation magnetic field from the drive coil to the sealed-sensor and the modified magnetic field can be captured by the pick-up coil with the resonant frequency information.

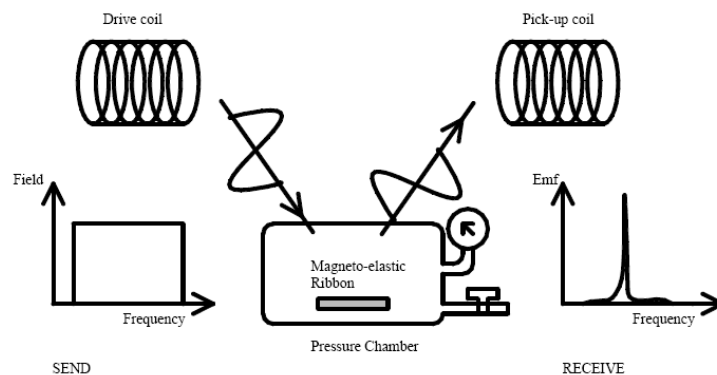


Figure 2.8 Schematic of the magnetoelastic sensor [13].

Piezomagnetic strain sensor cooperating with resonant frequency interrogation shows suitable properties for battery-free and remote strain sensing. This sensor shows as good

sensitivity, wide dynamic and frequency response range, linearity, and suffers the same temperature dependence as the piezoelectric counterpart. Moreover, uncertainty includes EMI from the environments.

2.4 Piezo-Resonant Strain Sensor

Piezo-resonant strain sensor has a special electromechanical property, which is that the resonant frequency changes with the change of applied strain directly when it is connected to some special circuits. Basically, since the sensor works at high (or ultrahigh) frequency, typically in RF range, the concerned strain information can be interrogated remotely and wirelessly in frequency domain.

2.4.1 Nanowire Strain Sensor

With the development of nanoelectromechanical system (NEMS) and nanomaterials, strain sensors begin to possibly have geometric dimensions as small as they can.

A microscale strain sensor, based on the studies about the frequency dependent response of carbon nanotubes to mechanical deformations since 1990s, is developed for its sensitivity of the resonant frequency to the applied strain and insensitivity to temperature. The simplest nanostructure is a single carbon nanotube string (or nanowire, formed with amorphous metal atoms) suspended between electrodes. Size and strain rate effects play important roles in determine the response of nanowire [31-33] and the semiconducting nanowires are studied in [14]. When a nanowire is deformed, the length and diameter are changed, and its resonant

frequency changes accordingly. Nanotube film used as strain sensor is working in the same principle [15].

The nanotube-based strain sensor has its own advantages. The sensitivities can be enhanced with reduction in tube length and tube diameter for axial strains sensing respectively. The strain resolution can reach nano-strain and the sensing capability far exceeds that of current strain sensors which enables the nanotube-based strain sensor for high accuracy applications.

2.4.2 Cavity Strain Sensor

When loads are applied and slightly deform a cavity's shape, the resonant frequency of the cavity is changed. This is known as the mechanical oscillator. There are many types of these resonant structures. A metal cylinder passive coaxial cavity shown in Figure 2.9 is presented in [16].

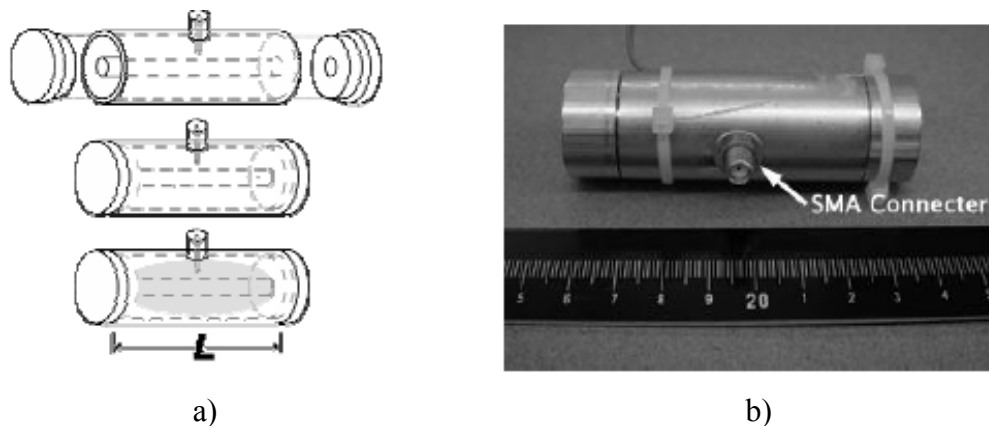


Figure 2.9 Diagram and photograph of resonator construction [16].

When the sensor is strained, the inner dimensions of the cavity will change proportionally to the applied strain, which will result in a shift in the resonant frequency of the cavity. The

resonant frequency can fall into the RF range like nanowire, which can be transmitted to the sensor and coupled via an attached antenna, based on the properly dimensions of the cavity.

2.5 Piezo-Optical Strain Sensor

In the last two decades, the optical sensor is probably the most popular method for measuring strains. Their main advantages are simplicity, the absence of the loading effect, and relatively long operating distances. They are insensitive to magnetic field and electrostatic interferences, which make them quite suitable for many sensitive and nondestructive evaluation (NDE) applications. Currently, basic technology has been substantially improved. Some more complex and sophisticated products have been developed.

2.5.1 Fiber Optic Strain Sensor

2.5.1.1 Fiber Optic Bragg Gratings Strain Sensor

The Bragg Gratings based fiber optic strain sensor is fabricated by writing gratings on the core of an optical fiber. Fiber optic Bragg grating (FOBG) strain sensors are extensively used to measure strains as an alternative to strain gauges. Essentially, when a broadband light is launched into a fiber core to pass through a Bragg grating, a narrowband light at the Bragg resonance wavelength are reflected back by the periodic refractive index variation. This optical fiber is then typically attached to or embedded into the surface of the structure. Basic operating concept of FOBG can be described as below. When the fiber grating is expanded or compressed the grating period expands or contracts changing the spectral filter response of the grating. The strain measurement is done by measuring the corresponding spectral shift in

the peak position of the reflection band from the FOBG by spectrum analysis. This sensing principle of the FOBG strain sensing system is shown in Figure 2.10 below [17].

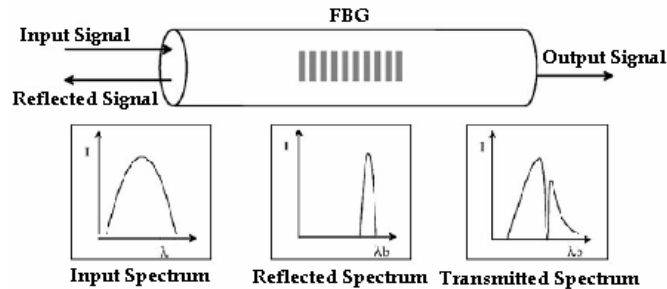


Figure 2.10 A schematic of FOBG sensing concept [17].

2.5.1.2 EFPI Fiber Optic Strain Sensor

The so called extrinsic Fabry-Perot interferometric (EFPI) FOS is thought to possess small size high sensitivity, and immune to electromagnetic (EM) interference, which can be modified for distributed or multi-parameter measurement [18]. Simply, a cavity is employed in EFPI strain gauge, which works as a frequency filter whose transmission frequency is intimately related to the length of the cavity. The simplest configuration of a popular EFPI for strain measuring is shown below in Figure 2.11. The sensor consists of two mirrors (two optical fiber ends) facing each other. One fiber, used as input-output fiber, and the other one, used purely as a reflector, are aligned by using a tube and together form an air gap which acts as a Fabry-Perot (FP) cavity with length d . When the laser light is guided into the EFPI sensor, a portion of the light is reflected from each internal mirror generating an interference effect in the input-output fiber. The phase shift directly affects the relative intensity of the reflected lights. Depending on the amount of refractive index change or change in sensor cavity length due to perturbation, the reflective intensity will sweep through maximum and

minimum interference effects. The strain can be decided by processing the reflected signal [19].

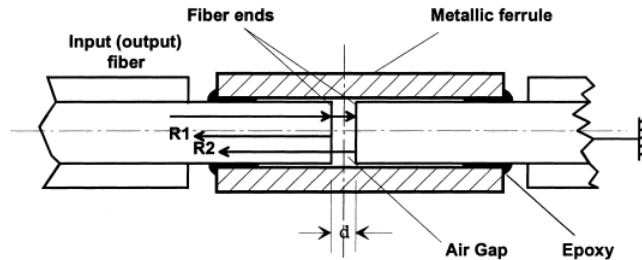


Figure 2.11 Typical EFPI sensor [19].

2.5.1.3 Fizeau Interferometric Fiber Optic Strain Sensor

Similarly as the EFPI, extrinsic Fizeau interferometric (EFI) FOS is employed for small strain measurement. The sensing principle of EFI is described the same as EFPI. By vary the length of the cavity enclosed by two fibers, thereby altering the phase difference between the references and sensing reflections, strains in the tube housing the two fibers can be determined. The difference of EFI and EFPI is that, instead of using the other single-mode fiber as the reflector, EFI employs a multimode fiber (Figure 2.12). Investigation on measuring strain induced by elastic stress SAW fields using EFI is held by Tran et al in 1992 [20].

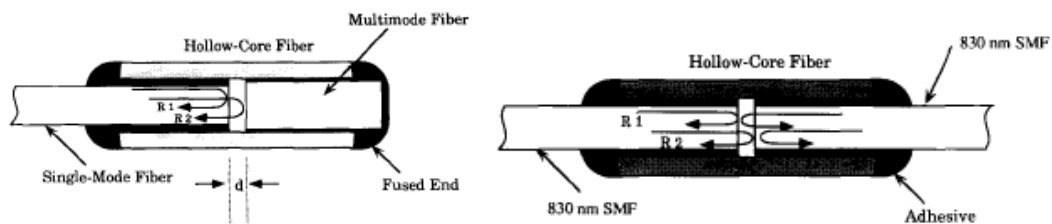


Figure 2.12 Conventional (left) and Stabilized (right) EFI fiber optic strain sensor [20].

2.5.1.4 Sagnac Interferometric Fiber Optic Strain Sensor

Sagnac interferometers have been principally used to measure rotation [21], as optical gyros in aerospace and navigation [22], optical filters [23] and frequency discriminators [24], and disturbance sensors (e.g., intrusion detection) [25]. It is also possible to use the Sagnac interferometer to accomplish strain sensing and measurement tasks. An invention of fiber optic sensing system is carried out by Udd et al in 1990 [26], which allows the magnitude and location of a time varying disturbance (e.g., strain) to be determined along a single fiber by using the Sagnac interferometer based configurations that operate in dual-sensing mode which allows position independent sensing along the entire fiber loop in one mode and position dependent loop in the other.

Advantages of fiber optical strain sensors include simple setup, the absence of the loading effect, and relatively long operating distances, insensitive to magnetic field and electrostatic interferences, which make them quite suitable for many sensitive and nondestructive evaluation (NDE) applications with more accuracy requirements. However, the applications of this kind of strain sensor are limited by the cost of the optical fiber and corresponding equipments, and the complexity of both the hardware and software configurations. Although this fiber optical strain sensor is designed for large area monitoring (e.g., intrusion detection for military bases, airport, critical facilities), long-distance power supply to each module and information collection from each sensing loop are among the constraints for the prevalence of the fiber optical strain sensor.

2.5.2 Optical Surface Strain Image

Experimental optical methods have been developed for surface displacement measurements in solid mechanics. The application of computer vision techniques for non-contacting and full surface measurement provides a simpler, more effective and more consistent way to obtain the surface roughness, stress and strain information by digital image processing than any other strain sensing method. Techniques for strain measurement development based on image processing, especially in these five years since 2000, are briefly reviewed in this section.

2.5.2.1 Digital Image Correlation Strain Sensor

Digital image correlation (DIC), an optical method to measure deformations on the objective surface, is developed in early 1980's. Two-dimensional correlation using white or laser speckles is applied to obtain the deformation via comparison of digital video images of the undeformed and deformed configurations [27].

Basically, the strain measurement is simply done by determining the displacements of selected points or grids on the surface of the deformed specimen (Figure 2.13), which can be inks, laser scans or light emitting diodes. The conceptual simplicity is attractive based on the highly developed techniques in computer vision, intricate algorithm, software programming and digital signal process. Following all these, this DIC method is becoming mutual as one of the promising uncontact sensing approaches with which strain can be continuously measured.

The calculation process depends on the complexity of the forming and the number of the shots. After this process, surface strain can be calculated based on photogrammetric

equations. Improvement of the system accuracies can be realized by increasing the number and the resolution of photographs and the positioning resolution.



Figure 2.13 3-dimensional DIC surface strain measurement system [28].

2.5.2.2 Photoelastic Strain Sensor

Photoelastic stress analysis is a powerful full-field non-contact optical method for determining stresses and load paths in components or structures. A quick and simple approach to photoelastic analysis involves applying a photoelastic coating to the under test devices. Photoelastic coating is a thin, transparent plastic of uniform thickness which, when bonded to the surface of a test part and viewed with polarized light, produces a full-field indication of the strains present in that under load surface. The principle of this method is based on the law of reflection and birefringence in the optically anisotropic material induced by stress or deformation. Although photoelasticity has often been described as a stress effect, it could also instead be a strain phenomenon, since plane stress and plane strain are closely related although not exactly the same. By applying the principle of refraction, photoelasticity, and a series of optical filters, the strain/stress distribution in solid can be analyzed visually.

After the improvement of high-resolution digital cameras and powerful image processing hardware and software, researchers begin to enjoy the photoelasticity in engineer applications. Existing polariscopes have been modified to record the fringe patterns directly as digital images, then transferring the digital images to computers for analysis.

2.5.2.3 Luminescent Strain Sensor

A new experimental stress analysis technique that measures surface information, especially strain on the surface of 3D mechanical components is presented in [29]. The method, called luminescent photoelastic coating, is largely based on traditional photoelasticity. Figure 2.14 shows a schematic diagram of the basic system instrumentation, where a luminescent photoelastic coating (LPC) is applied to the specimen under test.

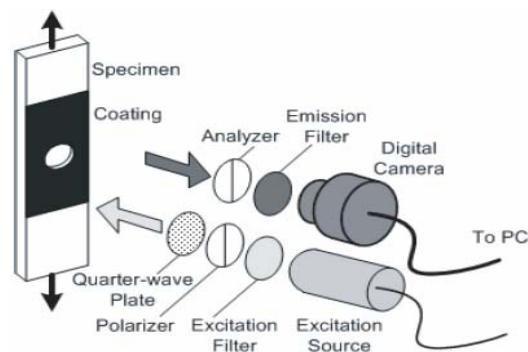


Figure 2.14 Schematic diagram of basic LPC instrumentation.

Currently, other types of luminescent coatings—pressure sensitive paints and temperature sensitive paints—are in widespread use in a variety of industries. Although LPC holds apparent advantages over traditional reflective coatings, research still needs to focus on decoupling the principle strain on complex geometries using information acquired as well as expanding the technique to dynamic and high temperature applications.

The optical strain image offers a noncontact approach for surface strain measurement. Although this method, compared to the other methods, less effective, more intricate and more costly, this method, because of its noncontact measurement, extremely immune to any forms of the environments interferences, and moreover, in high temperature strain measurement where most of the existing strain sensing approaches become invalid.

2.6 Discussions

Strain measurement has become the most critical part involved from machine working-condition monitoring to aerospace structure health inspection. Strain sensing technologies are still under a development trend to be embedded, passive, wireless and nanoscale. MEMS and NEMS technologies, which make the strain sensor small and thin enough for embedding application, will definitely have their boom continuously. The resonant technologies and telecommunication will be critical in realizing powerless and noncontact strain sensing. Simultaneously, wireless network topologies and algorithms will make the sensor network as an excellent candidate in future's strain sensing. Optical fiber and robot vision technologies will be still under attractive as the major leading candidate for their amazing performance in large-scale and full-field strain mapping. However, conventional strain sensing technologies are being improved to have more accuracy, resolution, better dynamic characteristics, higher resolution, reliability and less expensive for mutual applications. The demand of nondestructive evaluation and inbuilt sensing methods contributes greatly on the strain sensing society targeted toward optimizing the embedding sensor. Researches are kept on looking for integrated sensing systems, in which a particular demand for multi-functional

sensor dusts is required, that are capable of detecting several concerned parameters without crosstalk interference. Following this development in miniaturized sensor dusts, sensor arrays and sensor network will gain more attentions for industrial, business and military applications with a combination with advanced signal processing techniques, such as fuzzy logic and pattern recognition. Two-way communication is becoming critical in certain particular applications, which offers a function for data collection, analysis and control as well at the same time.

Eventually, strain sensing is about to become digitalized, minimized, embedded, integrated, passive, wireless and low-cost in the foreseeable future. Following this conclusion and foreseen to the development of the strain sensing, a novel strain sensing which provides most of the desired properties listed above, are proposed and explored in this thesis.

3 INTERDIGITAL CAPACITOR

This chapter starts with the construction of the proposed passive strain sensor and the physical model of the interdigital capacitor as the strain sensing element. After the exploration of the geometry dependent capacitance of the interdigital capacitor, the strain sensing principles of the interdigital electrodes are disclosed and exhaustively explained. Aiming to have minimized size and improved sensitivity, design considerations of the geometric dimensions of the interdigital capacitor are discussed. Meanwhile, the performance of the optimized interdigital capacitor is simulated.

3.1 Interdigital Capacitance Analysis

Interdigital electrodes (IDEs) are one of the most commonly used periodic structures for sensor applications. Recently, the advanced applications such as non destructive testing (NDT), microelectromechanical system (MEMS), telecommunication, biosensing, chemical sensing and piezoelectricity involve interdigital electrodes in various ways. Before we get into the proposed strain sensing principle, approximation model of interdigital capacitor will be briefly illustrated.

3.1.1 Approximation Model

A schematic description of the regularly repeating geometry of the IDEs sensing element is shown in Figure 3.1. The IDEs consist two series of electrodes with opposite polarities

positive and negative on each finger. Practically, the operation of the IDC itself involves an application of a differential voltage across the two electrode terminals.

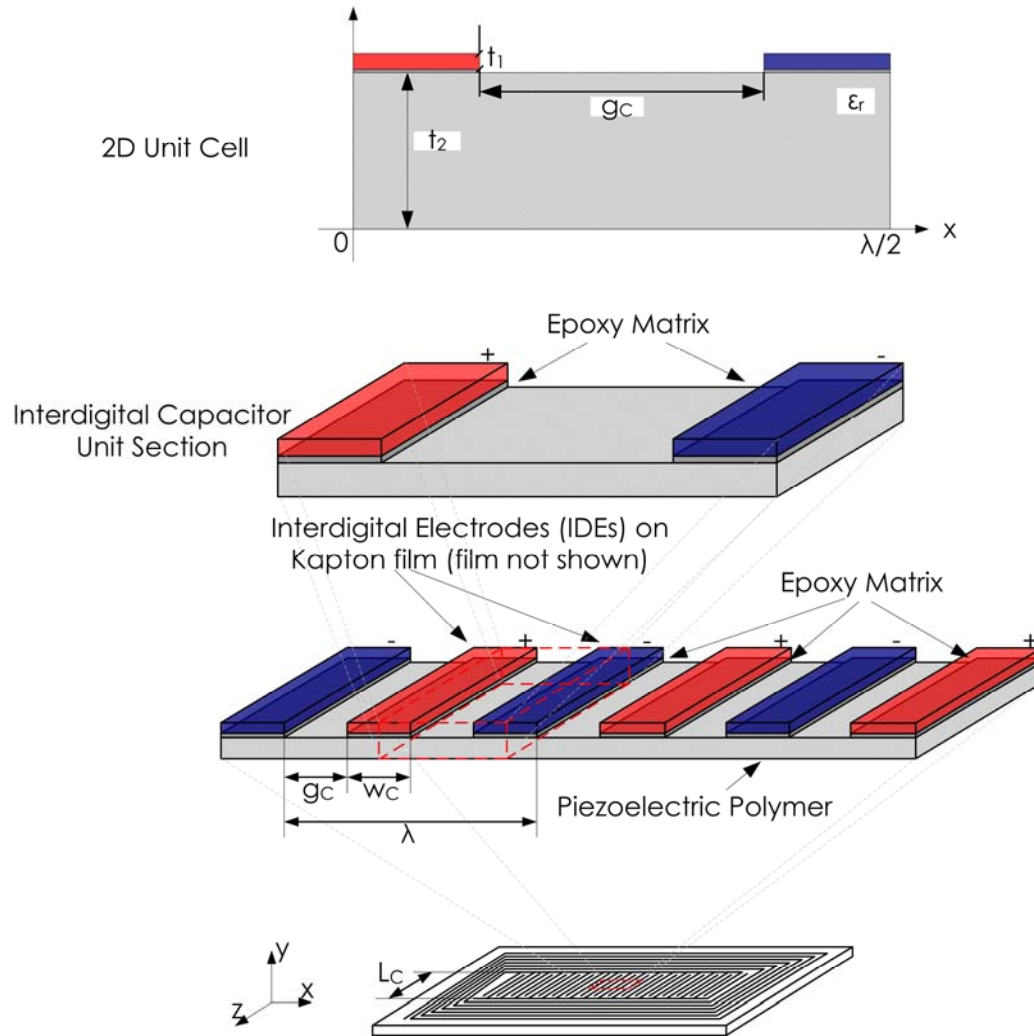


Figure 3.1 A schematic view of the interdigital capacitor simplification.

Investigation of the potential field in the system conjunction with the system geometry successfully reveals symmetry property in the IDC and helps to disassemble the overall system into repeating cells with identically the same physical behavior. By effectively and reasonably ignoring the parasitic influence on the IDEs finger edges and ends, the analysis of the IDC is simplified. As shown in Figure 3.1, a single IDE in x-direction is broke up into

two parts in the middle of the finger along the z-coordinate. This half-finger corresponds to the other half-finger on the opposite IDE. Now, under this assumption, the entire IDC is predigested into a single half-unit cell as a straightforward model. However, this is still a 3-D problem for electrical field.

Following with the electric field symmetry conditions, the physical connection between the conductive traces and the piezoelectric polymer layer is identical along the z-direction. These unvarying boundary condition and electrostatic condition make the electric field of the unit cell uniform along the z-direction. Although the practical application of the epoxy (e.g., nonuniform thickness, leakage, conductivity etc.) induces an inhomogeneous physical boundary condition to the problem, carefully operation of the epoxy with a neglectable thickness compared to the piezoelectric polymer will decrease the error of this approximate model. Without varying material properties along z-direction, the IDC unit cell model will be 2 dimensional which possesses only x- and y-direction. This 2-D IDC unit cell analysis has been referenced in plenty of literatures [57-64]. In each of these repeating 2-D unit cell in IDC, the electric field, the piezoelectric polarization field and the capacitance can be treated the same. Thus, analysis of the electrostatic properties of this 2-D unit cell is critical for the determination of the electrostatic properties of the entire IDC.

3.1.2 Analysis Approaches

Earlier development efforts on finding the complex impedance between interdigital electrodes were dedicated. However, this task is not a trivial one. Even 2-D approximation of the interdigital structures results in the electric field distribution that is too complex to be

described rigorously by simple algebraic expressions. The potential distribution along the sensor-material interface between the two ports is not known in advance, and depends on the material properties and geometric parameters of the structure.

Mathematical description for a so-called continuum model was developed in the 1980s and 1990s. The representation of electric potential with spatial Fourier modes falls between closed-form analytical solutions and numerical techniques to solve the conservation of charge boundary condition between electrodes. It is less expensive than traditional numerical approaches, but it does not offer analytical expressions suitable for extensive manipulation. Being limited to multiple-layer problems, the continuum model does not possess the generality of numerical techniques that allow computation of electric fields associated with arbitrary shapes [32].

Electromagnetic (EM) simulator based on finite element method (FEM) has been used extensively for calculation of transmission coefficient, impedance and capacitance matrices. Frequently used electromagnetic simulators include Agilent Momentum for unshielded numerical integration based planar analyses (Agilent® Technologies), Ansoft HFSS for 3 dimensional arbitrary frequency domain analyses (Ansoft® Corporation), CST Microwave Studio for 3 dimensional arbitrary time domain/wideband frequency domain analyses (Computer Simulation Technology) and Sonnet for shielded FFT based planar analyses (Sonnet®).

Another potentially useful approach for the calculation of 2D interdigital electrode capacitance stems from conformal mapping. Conformal mapping is one of the most frequently used approaches to transform an appropriate space region of IDC to a parallel plate capacitor geometry whose capacitance value can be calculated. Typical examples of

such analysis and analytical solutions for IDC capacitance are given by Endres et al in 1991 [33] and Igreja [34].

3.1.3 IDC Model

By symmetry, the perpendicular planes halfway between the electrodes are equipotential planes with $V=0$ which acts like an electric ground where electric field lines crossing normal to these planes shown in Figure 3.3. This holds exactly true for an infinite periodic structure whose electrodes fingers have an infinite length. In the case of a finite periodic structure, there is an error incurred by this assumption due to impacts from other cells and thus the variation in the ground planes, which especially happen closer to the boundary electrodes. Therefore, it is assumed that most of the polarization phenomena occur in a region where the variation in the ground planes is not significant. The finite length of the electrodes is much greater than the wavelength of the IDC structure so that for practical purpose they can be considered as infinity.

One can also neglect the capacitance at the side walls of the electrodes, because the thickness of the electrodes are much thinner than their width, and thus, the capacitance is specified between the upper and lower half planes. However, the thickness of the thicker electrodes in our design can not be ignored. Corrections to the equations derived by Igreja are added taking into the account of electrode thickness seen in Equations 3.1 and 3.2.

At the lower half plane of the IDC, the thickness of the substrate ($\sim 18 \mu\text{m}$) is not much smaller than the wavelength of the IDC so that the substrate can be considered as a finite layer. Since the thickness of the beam ($\sim 3 \text{ mm}$) is much greater than the wavelength, and thus

the thick beam is considered as an infinite layer. At the upper half plane, the strain sensitive layer and the protection layer are considered as finite layers, while the air layer is infinite (Figure 3.2). The calculation of either the C_I or C_E can be done based on this half unit cell model.

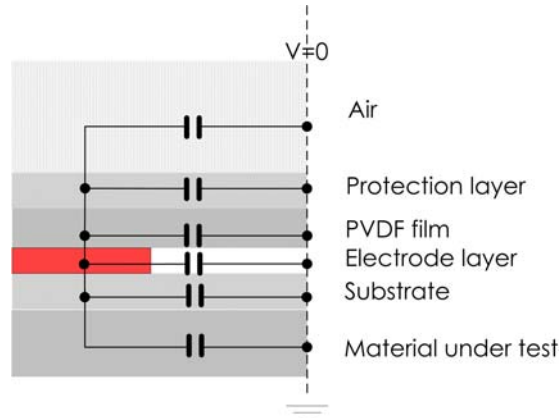


Figure 3.2 A half unit cell model of the proposed multilayer interdigital capacitor.

The total capacitance of the half unit cell C_I and C_E can be treated as a summation of five individual capacitances which are given below:

$$C_I = C_{I_air\infty} + C_{I_protectlayer} + C_{I_substrate} + C_{I_PVDF} + C_{I_substrate} + C_{I_beam\infty} + C_{gap} \quad 3.1$$

$$C_E = C_{E_air\infty} + C_{E_protectlayer} + C_{E_substrate} + C_{E_PVDF} + C_{E_substrate} + C_{E_beam\infty} + C_{gap} \quad 3.2$$

The equilibrium circuit of our proposed multilayer interdigital capacitor using the model on a testing beam is shown below in Figure 3.3.

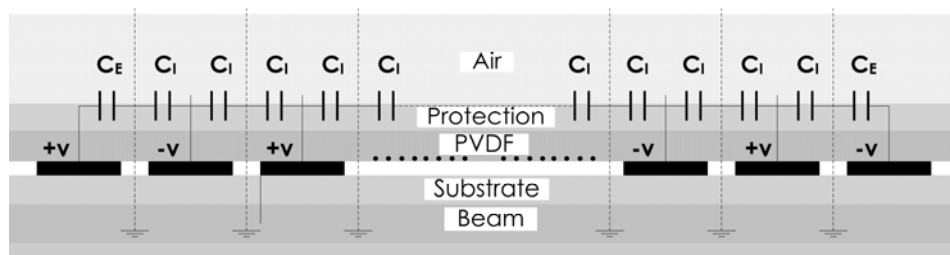


Figure 3.3 The equivalent circuit of the multilayer interdigital capacitor.

Based on the so-called partial capacitance technique, the proposed four-layered structure on the bending beam can be split into five individual layers with capacitances shown in Figure 3.4.

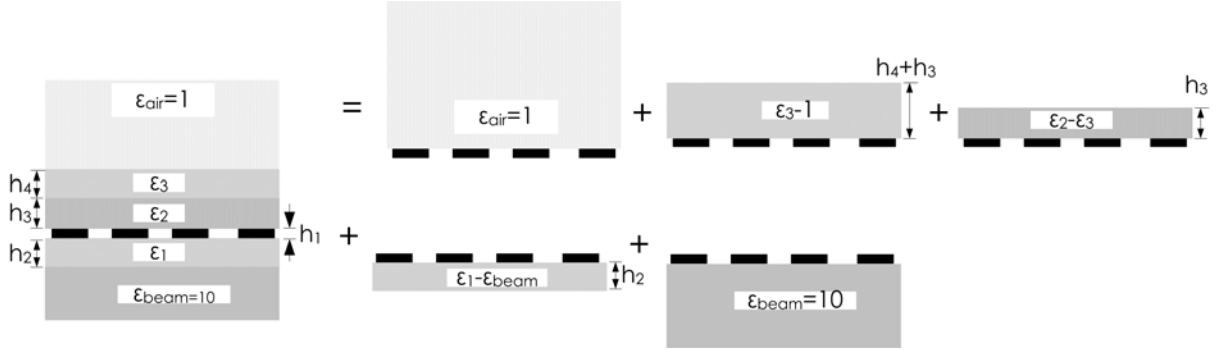


Figure 3.4 Splitting of the proposed four-layered IDC [34].

The capacitances of the IDC unit cell with infinite layer and finite layer at interior or exterior electrodes are described using a complete elliptic integral of the first kind $K[k]$. The detail calculations are shown in Table 3.1

Table 3.1 Detailed equations needed for the calculation of C_E and C_I .

	Interior electrodes	Exterior electrodes
Finite layer	$C_I = \epsilon_0 \epsilon_r \frac{\mathcal{K}(k_I)}{\mathcal{K}(k'_I)}$	$C_E = \epsilon_0 \epsilon_r \frac{\mathcal{K}(k_E)}{\mathcal{K}(k'_E)}$
	$k'_I = \sqrt{1 - k_I^2}$	$k'_E = \sqrt{1 - k_E^2}$
	$k_I = t_2 \sqrt{\frac{t_4^2 - 1}{t_4^2 - t_2^2}}$	$k_E = \frac{1}{t_3} \sqrt{\frac{t_4^2 - t_3^2}{t_4^2 - 1}}$
	$t_2 = \text{sn}(\mathcal{K}(k)\eta, k)$	$t_3 = \cosh\left(\frac{\pi(1 - \eta)}{8r}\right)$
	$t_4 = \frac{1}{k}$	$t_4 = \cosh\left(\frac{\pi(1 + \eta)}{8r}\right)$
	$k = \sqrt{\frac{v_2(0, q)}{v_3(0, q)}}$	$\eta = \frac{g_C}{g_C + w_C} = \frac{2g_C}{\lambda}$
	$q = e^{-4r\pi}$	$r = \frac{h}{\lambda}$
Infinite layer	$C_I = \epsilon_0 \epsilon_r \frac{\mathcal{K}(k_{I\infty})}{\mathcal{K}(k'_{I\infty})}$	$C_E = \epsilon_0 \epsilon_r \frac{\mathcal{K}(k_{E\infty})}{\mathcal{K}(k'_{E\infty})}$
	$k_{I\infty} = \sin\left(\frac{\pi}{2}\eta\right)$	$k_{E\infty} = \sin\left(\frac{2\sqrt{\eta}}{1 + \eta}\right)$

where $K(k)$ is the complete elliptic integral of the first kind with modulus k , k' is the complementary modulus of k , v_2 and v_3 are the Elliptic theta functions, $sn(z, k)$ is the Jacobi elliptic function of modulus k , $\lambda=2(g_C+w_C)$ is the spatial wavelength, η is the ratio between the electrode width and the unit cell width which is known as the metal ratio, and r is the ratio between the thickness of each layer and the spatial wavelength. η and r are two geometric adimensional parameters.

The total capacitance of the IDC with N_C fingers of length l_C is given as

$$C = l_C \left[(N_C - 3) \frac{C_I}{2} + 2 \frac{C_I C_E}{C_I + C_E} \right], N_C > 3 \quad 3.3$$

As noticed in Equation 3.3 and Table 3.1, the capacitance of the interdigital capacitor is a function of η and r , the thickness, length and number of electrodes, and as well as the dielectric permittivity of each layer ϵ_r .

$$C = C(\eta, r, \epsilon_r, h_r, l_C, N_C) \quad 3.4$$

This simplified and reasonable 2-D unit cell of the IDC is the basic repeat analysis model for the capacitance and the variation of the capacitance with respect to the geometry design (section 3.1.2), the applied strain (section 3.1.3) and the attached material (Chapter 5).

3.1.4 Geometry Dependent Capacitance

Effects of η and r on the value of capacitance are studied. Plots of the capacitance of different unit cell geometries indicate the variation of the capacitance with the selection of η from 0.01 to 0.99 and r from 0.05 to 0.95 at $\epsilon_r=3.5$ and $N_C=40$, $l_C=40\text{mm}$.

Calculated capacitances with respect to each selected η are plotted in Figure 3.5. It is shown that the capacitance of the IDC unit cell decreases smoothly and exponentially with

the decreasing metal ratio. The capacitance of IDC with a narrow gap and relatively wide finger is much bigger than the one with wide gap and relatively narrow finger. Moreover, as noted in the Figure 3.5, the same amount of variation in metal ratio results a more significant change when the initial metal ratio is bigger than 0.9, which means that the interdigital capacitor with a higher metal ratio shows greater sensitivity than the one with a smaller metal ratio. Therefore, in our design of the interdigital capacitor, we tend to set the metal ratio at 0.9. Furthermore, as noticed in the range 0.8-0.9 of η the change of capacitance is nonlinear. Thus, aimed on having a better sensing linearity, we are trying to avoid our design in this range.

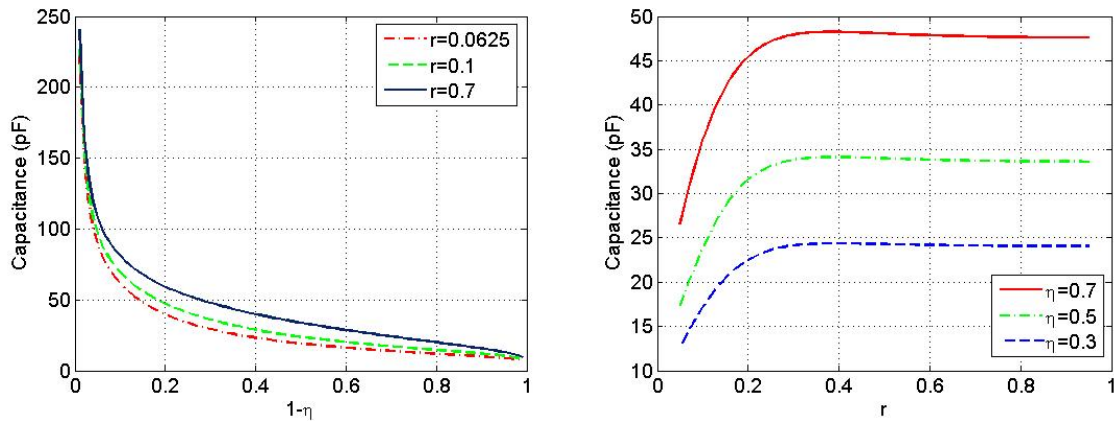


Figure 3.5 Capacitance as a function of $1-\eta$ and r .

It is shown in Figure 3.5 that the calculated capacitance of an IDC at a fixed metal ratio with respect to r . The unit cell length in our simulation is a constant. In the range from 0 to 0.35 of r , the increasing substrate thickness increases the capacitance and the capacitance reaches a maximum value at $r=0.35$. Then the capacitance tends to keep constant with the increasing r . For decreasing metal ratio, the capacitance decreases exponentially.

Based on above analysis of the geometry dependent capacitance of the IDC, it is concluded that a bigger metal ratio and a smaller unit cell length provide a higher capacitance. To achieve a larger range of capacitance and greater strain sensitivity, design of the IDC should incorporate a small unit cell with a big metal ratio. Moreover, to get a stable capacitance that is not influenced by the substrate, the thickness of the substrate must be bigger than 40% of the unit cell length. However, the variation in r can also be utilized in the strain sensing, this is because the thickness of each layer is slightly changed during the deformation. In this case, an r , which is smaller than 0.35, is desired.

3.1.5 Strain Dependent Capacitance

The IDC changes its capacitance value while being deformed. This capacitance variation depends on the relative directions between the extending direction of the IDC electrodes and the applied strain, thus the IDC shows great difference sensitivity at different directions without strain sensitive polymer, which is briefly discussed in [35]. Three possible relative positions when the IDC is attached to the bending beam including the extending directions of the electrodes parallel to the strain direction, perpendicular to the strain direction and at a random angle with the strain direction, which are indicated in Figure 3.6.



Figure 3.6 Three possible positions of the IDC on the bending beam.

Adhesive specifically for strain gage is used to make sure that the strain generated on the beam is exactly transferred from the surface of the beam into the substrate of the sensor. The

stretch strain on the top surface of the curved beam with position independent strain deforms the sensor by the same amount in two ways: varying the gap and width/length of the traces. In other words, the sensor is deformed uniformly because of the uniform strain on it.

Therefore, especially for interdigital electrodes, our simulation assumptions are:

1. The relative variations in the gap g_C , width w_C and length of the electrodes L_C due to reasonable applied strain are the same;

2. These variations subjected to the same tensile and compressive strain is nonsymmetrical, which means the sensor shows different sensitivity to the tensile and compressive strains;

3. The thickness as well as the length of the electrodes is considered to be constant during the applied strain.

In order to investigate the strain dependent capacitance of IDC, a reasonable strain range from $0 \mu\tau$ to $2500 \mu\tau$ are applied to the beam. Due to the attachment of the sensor on the beam, the beam offers a substrate which can be treated as infinity for the IDC (see Figure 3.4). Comparisons of strain effect on IDC capacitance with $N_C(= 40)$ electrodes and $L_C(= 4\text{cm})$ length for those three possible configurations are studied and results are shown below.

1. Let the sensor bent in the direction parallel to the extending direction of the linear electrodes. In this case, the length of the electrodes and the end gap are varied. Specifically, in case where the sensor substrate is deformed in an expanding shape, a tensile strain is produced in the substrate of the sensor to elongate the electrode length and enlarge the end gap. On the other hand, in case where the sensor substrate is deformed in a depressed shape, a compressive strain is produced in the substrate to shorten the electrode length and narrow

the end gap. Suppose there is no decrease in the width and thickness of the electrodes while they are being elongated. The capacitance at the electrode end gap compared to the major capacitance between the electrodes is small enough to be ignored.

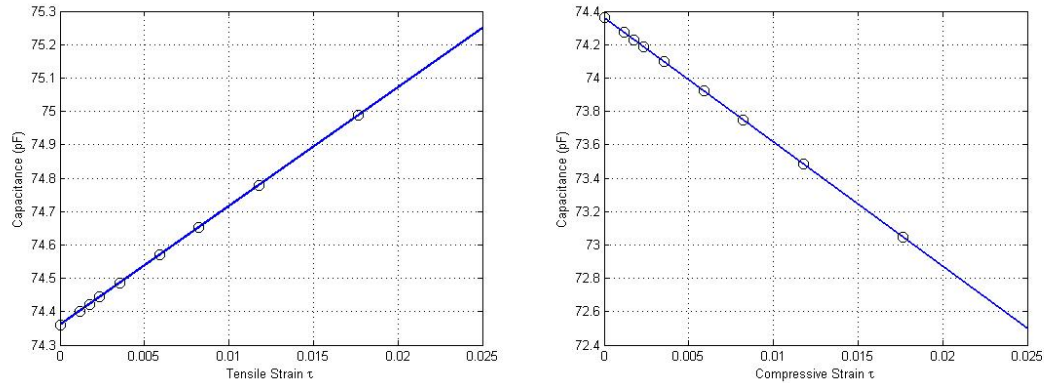


Figure 3.7 Strain effects on the capacitance value of IDC in parallel configuration with $\lambda=400\mu\text{m}$, $\eta=0.9$, $l_C=40\text{ mm}$, and $N_C=40$.

2. Let the sensor be bent in the direction perpendicular to the extending direction of the electrodes. In this case, the gap g_C between adjacent electrodes is substantially changed so that the value of IDC capacitance is changed. Especially, when the sensor is under tensile strain, the gap is widened. On the other hand, it is narrowed by the compressive strain. Because the strain on the beam would deform the electrodes and gaps the same amount, the variation in η can be ignored. As a result, the variation the capacitance of interdigital capacitor is only due to the variation in gaps between the electrodes.

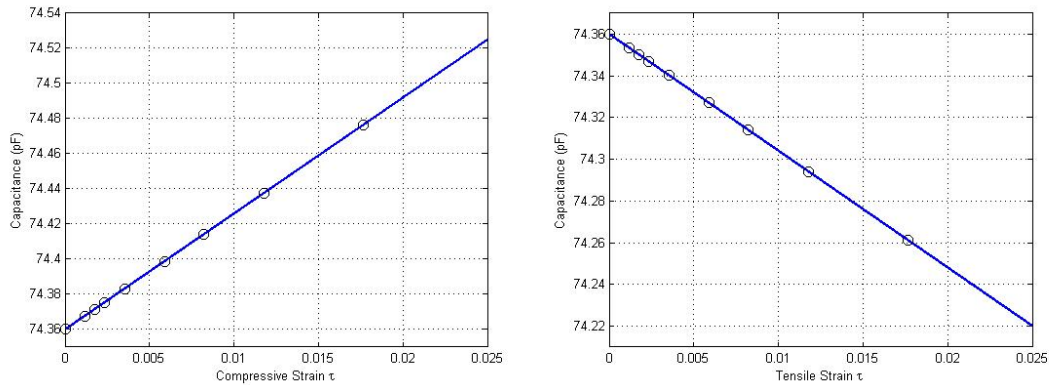


Figure 3.8 Strain effects on the capacitance value of IDC in perpendicular configuration with $\lambda=400\mu\text{m}$, $\eta=0.9$, $l_C=40\text{ mm}$, and $N_C=40$.

3. Let the sensor bent direction and the extending direction of the electrodes be a random angle (θ). Once the sensor is deformed by the applied tensile or compressive strain, length and width of electrodes, and gaps between them are changed. However, the same sensor shows great difference in the strain sensitivity with respect to different relative angles between the extending direction of the electrodes and the strain. Similarly to the two previous cases

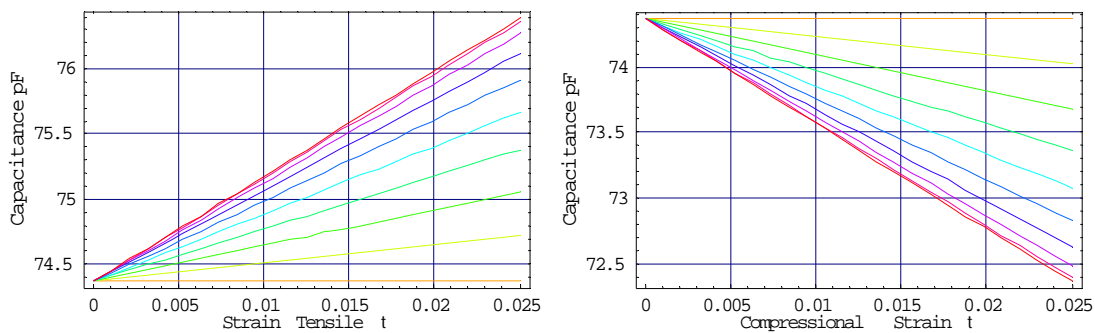


Figure 3.9 Strain effects on the capacitance value of IDC in the random angle configuration with $\lambda=400\mu\text{m}$, $\eta=0.9$, $l_C=40\text{ mm}$, and $N_C=40$.

Computer simulations are made in MATHEMATICA for the reason of special functions which are easy to implement in MATHEMATICA and schematics are made in MATLAB because of its powerful graphic function. Based on the simulation results of three sensor configurations, the strain dependent capacitance is studied. Basically, on the surface

which is deformed in an expanding shape, a tensile strain perpendicular to the extending direction of the electrodes is to widen the free space between the adjacent electrodes. The increasing free space and same ratio of increasing electrode width do not change the metal ratio η . The tensile strain decreases the capacitance when the strain direction is perpendicular to the fingers. On the other hand, on the surface which is deformed in a depressed shape, a compressive strain in perpendicular direction is to narrow the free space between the adjacent electrodes. According to Figure 3.8, the value of capacitance is increased by the tensile strain and decreased by the compressive strain, when the strain direction is perpendicular to the extending direction of the electrodes. Since the capacitance due to the thickness of the electrodes plays a small portion in the total capacitance, the change of the capacitance, or in other words the sensitivity in this direction is significantly small, which is understandable as the un-sensitive direction. As noticed in Figure 3.7, since the electrodes are parallel to the strain direction, the electrodes exhibit remarkable variation in length. Meanwhile, the free space ratio is not substantially changed as assumed so that the capacitance is significantly changed with the applied strain. Then, more general cases are simulated when the IDC electrodes are neither perpendicular nor parallel to the strain direction. From Figure 3.9, it is clearly shown that the slopes of those straight lines decrease with the increasing angle (the angle between the extending direction of the electrodes and the strain from 0° to 90°). This indicates that the interdigital electrode pattern serves the biggest strain sensitivity in an axial parallel to the strain direction and the sensitivity is greatly reduced with respect to the deformation in any other directions. Therefore, it is more effective to set up the sensor on the deformed body with IDC electrodes perpendicular to the surface strain directions in the sensor characterization. For practical application in strain sensing, several sensors can be

setup to measure the strain in different directions. Actually, the sensor shows different sensitivity under the same tensile and compressive strain, because it is easier to elongate the gaps than depress them.

3.2 Discussions

As we discussed in the previous sections, considerations have to be taken into account for an appropriate design of an interdigital capacitor without a particular strain sensitive layer as follows:

- 1) The IDC spatial wavelength which depends on the resolution of the manufacturing process of the IDC electrodes;
- 2) The geometric size of the sensor for different implementations;
- 3) The initial value of the IDC capacitance; and
- 4) The range of the change on the IDC capacitance.

Specifically, our prototyped sensor was fabricated using the normal photolithography to transfer the sensor design to the copper-clad polyimide material. The resolution of this low cost process has a limitation of gap and electrode width of about 100 μm and thus a spatial wavelength of about 400 μm . The initial value of the capacitance and the value of the planar spiral inductor decide the resonant frequency of the sensor. Together with the range of the change of the capacitance, the resonant frequency has a great influence on the design of the oscillating sweep frequency and the energy strength of the reader electronics associated with the signal conditioning of the sensor. Moreover, this change of the resonant frequency determines the sensitivity and the resolution of the sensor in an expected small strain and

large sensing range imposed by a change in the capacitance. The geometric size of the sensor can be minimized by applying geometric multi-objective optimization method in subsequence with the maximized sensitivity and the maximized interrogation distance. When this desired size is fixed, the best geometric dimensions with correspondent η and r can be found.

The relative changes in the IDC capacitance ($\Delta C/C$) are more important than the changes of capacitance. This is because the relative change offers the determination of the design of the IDC to get the best strain sensitivity and resolution. The relative capacitance change vs. the two adimensional parameters η and r are illustrated below in Figure 3.10.

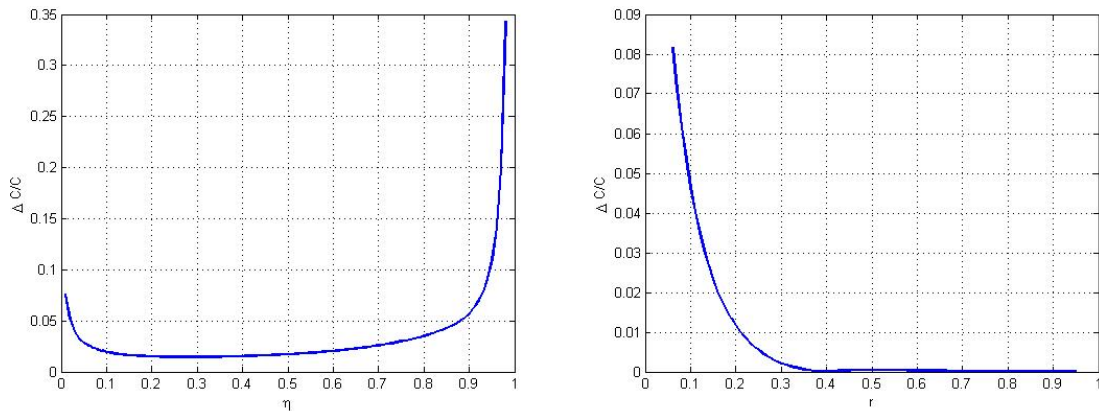


Figure 3.10 The capacitance change vs. η and r .

It is shown in Figure 3.10 that a bigger change in the relative capacitance appears at $\eta=0.99$ and $r=0.05$, which indicates that an interdigital capacitor shows a greater sensitivity at bigger metal ratio and η and small r , because small geometric deformations in the sensor result significant changes in capacitance. Therefore, in our interdigital capacitor design, the ratio η should be maximized and ratio r should be minimized.

4 PLANAR SPIRAL INDUCTOR

In this chapter, we will start with the principles that inductive power communication relies on. The energy transfer, which is based on the interaction between the planar spiral inductor on the sensor and the coil antenna on the reader, will be demonstrated. The geometry dependent inductance, strain effect on the inductance and induced power strength will be explored, and the results are used to optimize the design of both reader coil and planar spiral inductor with the aim of maximizing the communication distance, maximizing the power generation on the sensor and minimizing the geometric dimension of the sensor. At the end, the design optimization of the entire sensor will be executed using multi-objective nonlinear model.

4.1 Inductive Powering

4.1.1 Introduction

Wireless measurement circuits are established in literatures. For example, a wireless measurement acquisition system that uses existing strain gauge physically connected to a power source, microprocessor and transmitter is described by Young [37]. This system offers an stable and reliable measurement utilizing Whetstone Bridge for temperature compensation and a high frequency radio transmitter to reach a considerable distance. Similar systems have been minimized and widely used in Wireless Sensor Networks (WSNs), for example, COTS Dust [38] and Smart Dust [39] from UC Berkeley, Sensor Webs from NASA JPL project

[40], etc. Those sensor motes or dusts are made as small as coils and enable new and more proficient location for sensor placement. However, limited power source becomes a critical issue for the entire system to reach a long term performance, although researches have been addressed in the physical layer (e.g., developing lower power transmitter [41]) or MAC layer (e.g., developing energy efficiency protocols [89, 90]).

Another method of wireless measurement utilizes surface acoustic wave (SAW) on piezoelectric materials. A remote pressure measurement system based on this principle powered by RF field is introduced by Schimetta et al. in [43]. A conventional pressure sensor is connected to interdigital transducer built at one side on piezoelectric plate with two delay reflector arrays, while the SAW transponder is built on the other side which is connected to the antenna. Acoustic waves are generated and transferred along the plate due to the electromechanical coupling by sending RF signal to the antenna and producing differential voltage on the transponder. The reflected acoustic waves are reconverted back to electromagnetic pulse and retransmitted to the receiver where the pressure can be determined. Wireless measurement system with passive SAW sensor offers new and exciting perspectives for remote monitoring and control of moving parts, even in harsh environments if with suitable packaging. However, the propagation of the SAW also shows great dependent on the environment, geometric and material properties subject to environmental conditions. Those effects yield low system capacity, low bandwidth and application range. Nevertheless, SAW wireless sensors are totally passive and contain neither active element nor batteries [44].

A method of acquiring measurements without the need for physical connection to a power source is the use of passive radio frequency identification (RFID) tags [36]. This

method relies on the use of radio-frequency integrated circuits functionally coupled to sensors. Lately, a Wireless Identification and Sensing Platform, (WISP) which harvests energy from the surroundings radio-frequency-identification readers, is proposed by Philipose et al. in [45] based on traditional passive RFID systems. The wisps use ID modulation to communicate with the long range RFID antennas with their sensor data which is encoded in correlations with the ID of tags. The proposed sensor tag and data modulation is known as the α -wisps. Working with RFID protocols, the α -wisps is feasible in distributed sensing with unlimited density of readable tags and easily transmit multi-measurands from sensors. It requires no additional power supply and thus battery-free, wireless readable, and can support uniquely identified sensors. Still, the α -wisp suffers the same restrictions as the traditional RFID such as occlusion and presence of metal.

Uses of spiral inductors (different from the antenna in high frequency RF antenna) and capacitors to form resonant circuits have been used for various measurement applications. This wireless interrogation and remote powering is achieved through an inductively powered system which is generating a time varying electromagnetic field (usually in the frequency range from 300 KHz to 30 MHz [44]) based on Faraday's induction. Inductive powering is used initially and extensively in the area of RFID such as privacy and security systems to remotely power tags and then transmit the data. Moreover, it has also been used to supply power and read data in biomedical area. This method is particularly suitable for transmitting high energy for short distances as required in harsh medical and industrial environments where for example the remote module is surrounded with metal. This low frequency range generally allows the use of higher data transfer rates, which is essential if fast sensor reading or reading of multiple sensor modules is required [46].

4.1.2 Inductive Powering

The planar spiral inductor coil, together with the interdigital capacitor electrodes, forms a planar structure that can be attached to the surface or embedded to nonconductive composite materials for deformation measurement. The simplified model of the series connected PSI and IDC with a nearby reader coil for inductive powering is illustrated in Figure 4.1 as a LC resonator with self resistance. Basically, I_1 is a time variant variable which offers a property that its frequency varies in a time interval. The frequency of this current is a linear function with respect to time $\omega = \Delta\omega \cdot t + \omega_0$ ($T \leq t \leq T + \Delta t$) where T is the period of the frequency change. Once this current with a varying frequency applied to the primary coil, a varying magnetic field generated around this coil. Based on Faraday's law, induced voltage is generated on the remotely placed sensor.

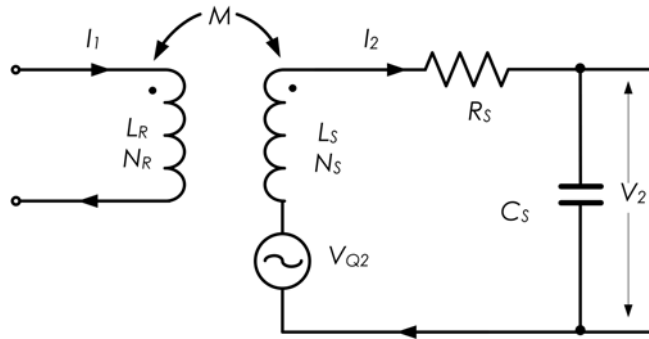


Figure 4.1 Equivalent diagram for magnetically coupled reader coil and sensor.

If the voltage u_{Q2} is induced in sensor PSI, the following voltage u_2 on IDC can be calculated [36]

$$V_{Q2} = j\omega M I_1 \quad 4.1$$

$$V_2 = V_{Q2} - j\omega L_S I_2 - R_S I_2 \quad 4.2$$

$$I_2 = j\omega C_S V_2 \quad 4.3$$

where I_2 is the current on the sensor, C_S is the capacitance of the IDC which is series connected to the PSI with an inductance L_S , R_S is the self resistance of the sensor. Therefore, solving the Equation 4.1 and 4.2 for u_2 , the voltage across the IDC becomes

$$V_2 = \frac{V_{Q2}}{1 + (j\omega L_S + R_S) \cdot j\omega C_S} \quad 4.4$$

As we assumed, a homogeneous sinusoidal magnetic field between the coupled coils, the Equation 4.1 can be expressed

$$V_{Q2} = j\omega \mu_0 A_S N_L \cdot H_{eff} \quad 4.5$$

$$V_2 = \frac{j\omega \mu_0 A_S N_L \cdot H_{eff}}{1 + (j\omega L_S + R_S) \cdot j\omega C_S} \quad 4.6$$

$$A_S = d_{avg}^2 \quad 4.7$$

$$H_{eff} = \frac{I_1 \cdot N_R \cdot d_R^2}{8\sqrt{(d_R^2/4 + x^2)^3}} \quad 4.8$$

Take Equation 4.8 and 4.7 into 4.6, we have

$$V_2 = \frac{\mu_0 \cdot N_L N_R d_R^2 d_{avg}^2 \cdot j\omega \cdot I_1}{8\sqrt{(d_R^2/4 + x^2)^3} [1 + (j\omega L_S + R_S) \cdot j\omega C_S]} \quad 4.9$$

When this planar resonance sensor enters the time-variant magnetic field of the reader antenna L_R , a change can be detected in the voltage V_0 across the reader coil. In order to clarify the change of V_0 , let us introduce the complex impedance and reflect impedance seen from the reader. The electrical behavior of the series resonant circuit on the reader in the presence of mutual inductance is like the imaginary impedance Z_s' which actually presents as a discrete component.

The equivalent circuit diagram of the series resonant circuit of the reader with the inductive coupled sensor is shown in Figure 4.2.

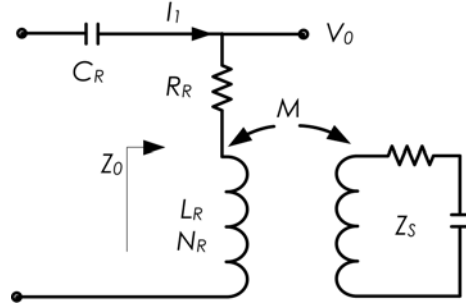


Figure 4.2 Equivalent circuit diagram of the inductively coupled reader and sensor.

In the analysis of the influence of the sensor on the frequency response of V_0 across the reader antenna, the classical approach is to eliminate the coupled reader coil and the sensor by reflecting impedances back to the reader. The total impedance of the series resonant circuit of reader with the inductive coupled sensor can be calculated

$$Z_0 = Z_R + Z'_S \quad 4.10$$

$$Z_R = j\omega L_R + R_R \quad 4.11$$

$$Z'_S = \frac{(\omega M)^2}{j\omega L_S + R_S + \frac{1}{j\omega C_S}} = -\frac{\omega^2 k^2 L_R L_S}{j\omega L_S + R_S + \frac{1}{j\omega C_S}} \quad 4.12$$

where Z_R is the reader inherent impedance, Z'_S is the reflected impedance of the sensor, R_R is the self resistance of the reader coil, C_R is the capacitance of the series connected capacitance with the antenna to maximize the current applied through the reader antenna, and k is the coupling coefficient. Therefore, we have the total impedance seen from the reader

$$Z_0 = j\omega L_R + R_R + \frac{\omega^2 k^2 L_R L_S}{j\omega L_S + R_S + \frac{1}{j\omega C_S}} \quad 4.13$$

Substitute $L_S C_S = 1/(4\pi^2 f_0^2)$ and $R_S = 2\pi f_0 L_S / Q$ into Equation 4.13, the total impedance is

given by

$$Z_0 = R_R + 2\pi fL_R \left[1 + k^2 \frac{\left(\frac{f}{f_0}\right)^2}{1 - \left(\frac{f}{f_0}\right)^2 + \frac{j}{Q} \frac{f}{f_0}} \right] \quad 4.14$$

The self-inductance of a circular loop reader antenna has the approximate low frequency inductance as below

$$L_R = \frac{\mu_0 d_R}{2} \left[\ln\left(\frac{4d_R}{a}\right) - 1.75 \right] \quad 4.15$$

The frequency response of V_0 on the reader coil is measured to monitor the impedance change due to the strain-dependent capacitance (C_S) change on the sensor. The capacitance change at a certain frequency is in the form of voltage change. However, this change in the voltage V_0 would be insignificantly small to measure. Moreover, the change of the capacitance will change the natural frequency (f_0) of the planar resonator. Therefore, instead of measuring the voltage change at certain frequency, a signal is used to generate a periodical sweep frequency range around the sensor natural frequency to measure the frequency shift. In this way, a very small variation in the impedance can be measured.

The sensor resonant frequency is decided by the voltage signals. The voltage response on the reader antenna coil verses sweep frequency without the present of sensor can be calculated by

$$V_0 = (j\omega L_R + R_R) \cdot I_1 \quad 4.16$$

The voltage response on the reader antenna coil verses sweep frequency with the present of sensor can be calculated by

$$V_0 = \left(j\omega L_R + R_R + \frac{\omega^2 k^2 L_R L_S}{j\omega L_S + R_S + \frac{1}{j\omega C_S}} \right) \cdot I_1 \quad 4.17$$

The precise measurement of the sensor resonant frequency now can be done by monitoring the frequency response of the voltage on the reader antenna. The resonant frequency of the sensor locates at the point where the voltage appears an abrupt change. However, this peak does not need to be the maximum value, because practically the environment will reduce the voltage quality which can be a lot smaller than the boundary values. It is clearly shown that in the Figure 4.3 at 15MHz, the voltage appears an abrupt change.

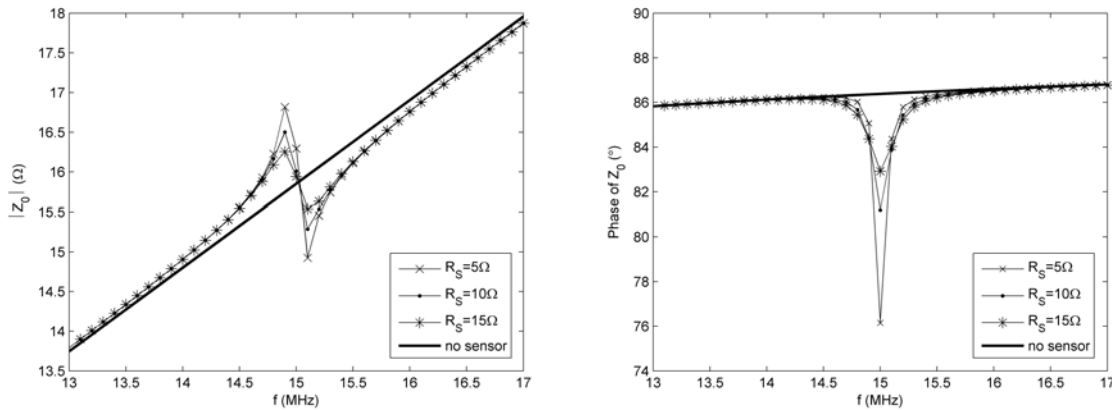


Figure 4.3 Frequency response of the voltage on the reader antenna coil with sensor.

4.2 Planar Spiral Inductor

4.2.1 Inductance Approximation

Planar spiral inductors (PSI), as small and highly integrated components, have been applied to wireless systems, since the conventional inductor consists of cores and wound

wires, which are obstacles for the integration with other devices. PSI, coupling with the primary coil, operates like a transformer based on the principle of electromagnetic induction. When an oscillating current is applied on a coil, a changing magnetic field to both primary and PSI is produced along the magnetic path in the air. In turn, an alternating voltage of the same frequency is induced in the PSI. In other words, the electrical energy is transferred from the input coil to the sensor and the strain information can be detected also from the coupled magnetic field. Square spirals are popular because of the ease of their layout. However, other polygonal spirals have also been used in circuit design. Among these, hexagonal and octagonal inductors are used widely [47]. A schematic layout of square planar spiral inductor is shown in Figure 4.4 below.

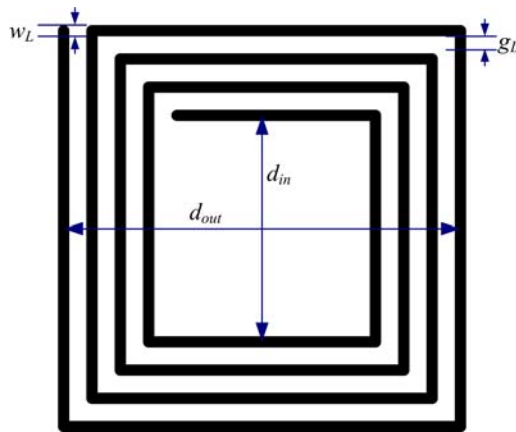


Figure 4.4 Layout of four turns square spiral inductor.

For a given shape, an planar spiral inductor is completely specified by the number of turns N_L , the track width w_L , the spacing g_L , and any of the following: the outer diameter d_{out} , the inner diameter d_{in} , the average diameter $d_{avg}=0.5(d_{out}+d_{in})$, or the fill ratio, defined as $\rho=(d_{out}-d_{in})/(d_{out}+d_{in})$. The thickness of the track t is ignored for their neglectable influence on the inductance. However, this thickness can not be neglected for the calculation of the self resistance (R_L) and the quality factor (Q).

Planar spiral inductor has been studied and modeled using lumped circuit model [48]. Although this model considered the parasitic resistors and capacitors in the substrate and between the tracks, an explicit and simple expression for the self inductance is not presented. In order to provide an inductor design directly from geometric specification, an accurate and simple expression in terms of the design variations is approximately formulated based on Wheeler's formula and concept of geometric mean distance (GMD) and arithmetic mean distance (AMD) [98, 99]. A modified Wheeler's formula, an approximation based on GMD and AMD, and an expression using data fitted monomial are presented by Mohan et al in 1999 [47]. Equations below show the calculation of self inductance especially for square PSI.

$$L = K_1 \mu_0 \frac{N_L^2 d_{avg}}{1 + K_2 \rho} \quad 4.18$$

where $K_1=2.34$, $K_2=2.75$, and $\mu_0=4\pi \times 10^{-6}$ Vs/Am. This equation is known as the Modified Wheeler Formula.

$$L = \frac{\mu_0 N_L^2 d_{avg} c_1}{2} [\ln(c_2 / \rho) + c_3 \rho + c_4 \rho^2] \quad 4.19$$

where $C_1=1.27$, $C_2=2.07$, $C_3=0.18$, and $C_4=0.13$. This equation is known as the expression based on current sheet approximation.

$$L = \beta d_{out}^{\alpha_1} \omega^{\alpha_2} d_{avg}^{\alpha_3} n^{\alpha_4} s^{\alpha_5} \quad 4.20$$

where $\beta=1.62 \times 10^{-6}$, $\alpha_1= -1.21$, $\alpha_2= -0.147$, $\alpha_3= 2.40$, $\alpha_4= 1.78$, and $\alpha_5= -0.03$. This equation is derived based on experiment measurement and named as Data Fitted Monomial Expression.

$$L = 1.39 \times 10^{-6} (d_{out} + d_{in}) N_L^{3/5} \log_{10} \frac{4}{\rho} \quad 4.21$$

The expression that is cited and used in some wireless sensing literatures is derived by Bryan in 1954 [49], which is most common seen self inductance calculation of PSI.

Figure 4.5 and 4.6 show the comparison of the inductance approximation formulas listed above. It is indicated that the inductances show great agreements at ρ no less than 0.3 from both of the Figures.

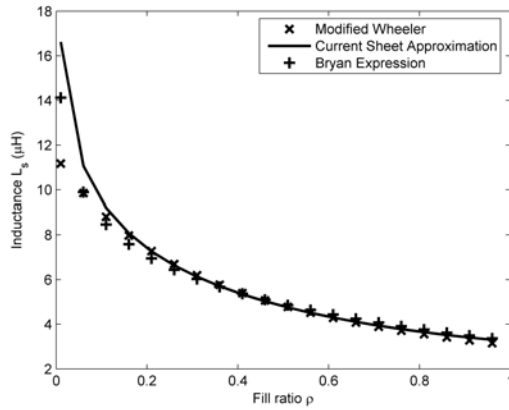


Figure 4.5 Calculated inductances vs. varying fill ratio ρ at $d_{avg}=61\text{mm}$.

From Figure 4.5, we can see those formula shows a great agreement in the calculated values of inductance. However, at small fill ratio calculation shows disparities in the value of inductance. For our application the fill ratio of the PSI are basically no more than 0.3. Therefore, the choice of those exist formula determines the sensor design and simulation results.

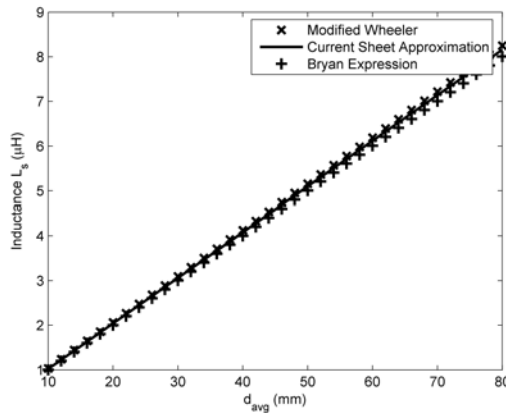


Figure 4.6 Comparison of calculated inductances with varying d_{avg} at $\rho=0.3$.

For different values of average diameter at fill ratio equals to 0.3, those calculations show great agreements in the calculated self inductance. Moreover, from Figure 4.5 and 4.6, it can be seen that the value of self inductance increases with the increasing average diameter and decreases with the increasing fill ratio. These simple, approximate expressions for spiral inductors are all based on geometric variables. Together with geometric variables in IDC, these are used to find the optimal sensor layout. From now on, all the later calculation of inductance will be based on Modified Wheeler Formula in numerical simulation and sensor layout optimization for its simplicity.

4.2.2 Strain Effect on Inductance

Following the same assumption when we carried out the analysis of the geometry and strain dependent capacitance of the interdigital capacitor, here in this section, the strain effect on the inductance change during the deformation will be discussed. Suppose the planar spiral inductor is attached to the bending beam. The strain on the top surface of the curved beam deforms the spiral inductor by the same amount in two ways: varying the gap and width/length of the turns. The width of the electrodes and gaps in between on the two sides of the turn perpendicular to the strain direction are varied by the strain. On the other hand, traces on the other two sides are varied in length by the strain. Figure 4.7 below indicates the geometric deformation that surface strain brings to the inductor.

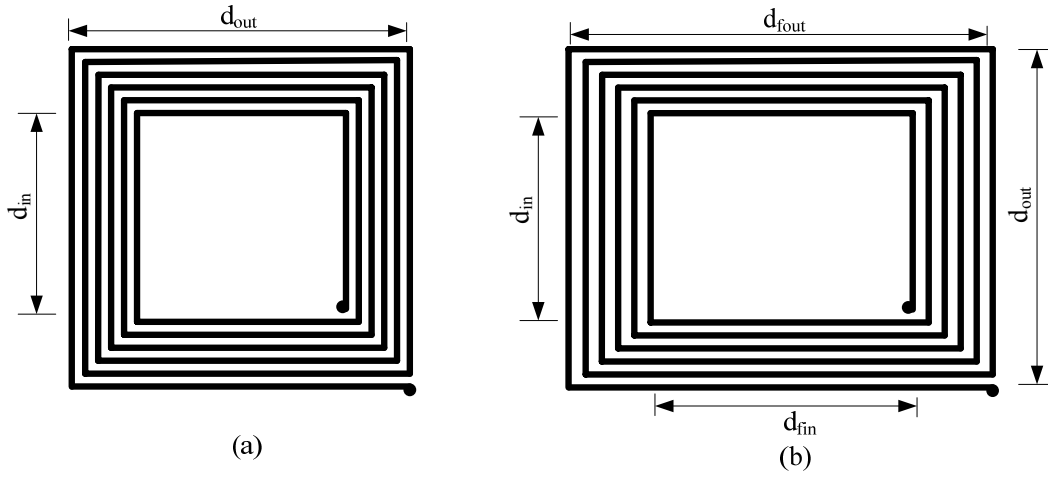


Figure 4.7 PSI deformation on bending beam a) before and b) after deformation.

In order to investigate the strain effect on PSI inductance, the same strain range from 0 $\mu\tau$ to 2500 $\mu\tau$ are applied to the beam as the one being assumed in IDC analysis.

$$d_{fin} = d_{in} (1 \pm \tau) \quad 4.22$$

$$d_{fout} = d_{out} (1 \pm \tau) \quad 4.23$$

where d_{fin} and d_{fout} is the final inner diameter and the final outer diameter after deformation.

So the effective inner and outer diameter of the changed PSI is given

$$d_{effin} = \sqrt{d_{fin} \cdot d_{in}} = d_{in} \sqrt{1 \pm \tau} \quad 4.24$$

$$d_{effout} = \sqrt{d_{fout} \cdot d_{out}} = d_{out} \sqrt{1 \pm \tau}$$

$$d_{effavg} = \frac{d_{effin} + d_{effout}}{2} = d_{avg} \sqrt{1 \pm \tau} \quad 4.25$$

$$\rho_{eff} = \frac{d_{effout} - d_{effin}}{d_{effout} + d_{effin}} = \rho \quad 4.26$$

Based on Equation 4.10, 4.11, and 4.13, the final inductance is given

$$L_{eff} = L \sqrt{1 \pm \tau} \quad 4.27$$

Assumptions are made before carrying out the analysis of strain effect on the value of inductance of the planar spiral inductor and the resulting resonant frequency shift. Capacitance is constant during the deformation and the resonant frequency is made to 15 MHz for undeformed sensor. The changes of inductance and resonant frequency with respect to the applied strain are shown in Figure 4.8.

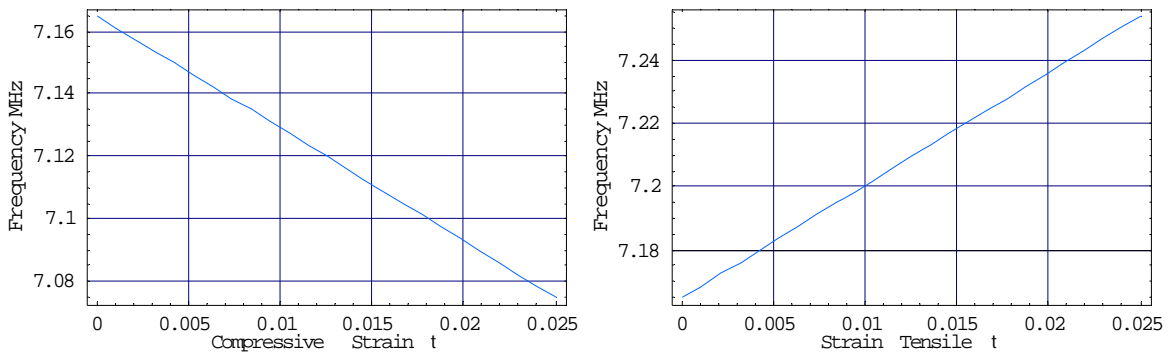


Figure 4.8 Strain effects on the inductance value of PSI with $w_L=1000\mu\text{m}$, $g_L=1000\mu\text{m}$, $d_{out}=78\text{ mm}$, and $N_L=8$.

4.3 Optimization of Sensor Design

After discussing the geometry dependent capacitance of the interdigital capacitor, inductance of the planar spiral inductor, strain effect on capacitance and on inductance, in order to get a sensor with best sensitivity, smallest size, longest detection distance and highest quality factor, the design consideration and method for the sensor together with the interdigital capacitor and the planar spiral inductor are dedicated in this section.

4.3.1 Optimization of Inductive Powering

The design goal of this inductive coupling power system for the sensor is to maximize the power generated on the sensor to get a recognizable signal, maximize the distance between the transmitter and the sensor, maximize the quality factor and minimize the geometric size. Therefore, the design process involves the optimization of the geometric variables for the planar spiral inductor, including the inner diameter d_{in} , the number of turns N_L and the track width w_L and spacing g_L . However, as a couple, the reader coil and the planar spiral inductor on the sensor can not be designed separately.

It seems like if we want to get a stronger magnetic field strength at a distance x to get a greater generated voltage on the sensor, we can increase the applied current; enlarge the coil radius and number of turns. However, frequency range and maximum magnetic field in short ranges and frequency range 9 kHz to 25 MHz have been restricted to prevent electromagnetic interference and also to limit human exposure to electromagnetic fields in standards such as EN300330 and by FCC regulation [50]. The current density and power density in air and the absorption rate for human body are specified in [51]. Allowable electric and magnetic field strengths are then derived from these basic restrictions for a commercialized radio frequency devices working at 13.56 MHz. At this frequency, FCC gives a limit of 0.16 A/m on the magnetic field strength which can be emitted by the radio frequency devices. Although the designed frequency sweeper is designed in a range of 10 MHz to 20 MHz not at a specific frequency point, this restricted magnetic field strength at the center of the coil in our frequency range is still adopted as the maximum value for the reader antenna design. In Equation 4.1, at distance $d=0$, the maximum magnetic field is set to 0.16 A/m. The graph

below shows the magnetic field strength with the distance for the coil with different radius, where $N \times I$ is set to the value so that the maximum field strength is 0.16 A/m at $d=0$. It can be seen that with the increasing distance the magnetic field decreases and with the increasing radius the magnetic field increases. In order to maximize the detection range, the radius of the reader coil is designed to be large.

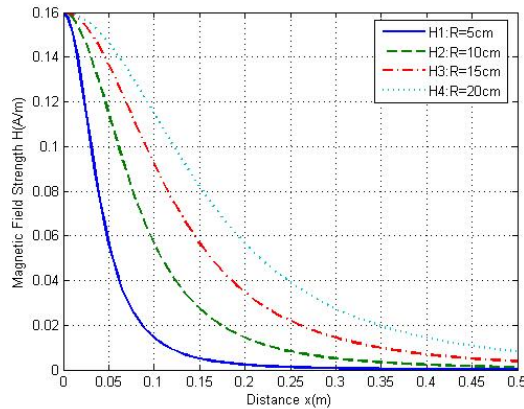


Figure 4.9 Magnetic field strength vs. distance with $I_I=0.16$ A/m at $N_R=1$.

It is shown in Figure 4.9 that with a bigger reader coil, the magnetic field strength is stronger than the one from smaller reader coil, which also means that with the same magnetic field strength the bigger reader coil can reach a further detection distance from the sensor than the one with smaller radius. Practically, reading performance does not necessarily increase when using a large antenna, although larger coils tend to yield wider coverage areas for the sensors. The maximum size of the reader coil is limited by the fact that in order to avoid transmission line effect the total length of the reader coil should be significantly less than the wavelength in frequency range 10 to 20 MHz which is approximately 15 m to 30 m [53]. Furthermore, the larger coil would receive more noise from the environment and result in a worse signal to noise (S/N) ratio. A balance should be attained between the detection

distance and the reliability. Thus, the reader coil designed in our investigation has a single turn and diameter of 15 cm. The total length of the coil is therefore significantly less than the wavelength and transmission line effects do not have to be considered. Then, the maximum current I_1 in reader coil can be calculated by taking these into Equation 4.8. At $x=0$ m, $H=0.16$ A/m, $d_R=150\times 10^{-3}$ m and $N_R=1$, we have maximum $I_1=1.1685$ A.

In order to guarantee the homogeneity of the magnetic field in the area A_S , the condition $A_S \leq A_R$ should be fulfilled. We have $d_{out} \leq d_R \times \sin(\pi/4) = 0.1006$ m at $x=0$. For $x \neq 0$, d_{avg} should be much smaller than 13.29 cm to validate all the involved equations by keeping a homogeneous magnetic field. However, the decreasing d_{avg} results in a decreasing voltage generated on the sensor due to the decreased mutual inductance and self inductance and make the signal less recognizable. The ratio of turns between the transmitter coil on the reader and the planar spiral inductor coil on the sensor is the other determinant of the voltage that can be induced by this inductive powering (Equation 4.9). Although the voltage V_2 can be increased by increase the number of N_L , this action would decrease the induced voltage linking in the opposite direction from sensor to reader. This would result in an even worse unreadable voltage signal. A balance should be also considered on the generated voltage on the sensor and the ‘voltage’ signal generated on the reader. Till now, for equation 4.9, to maximize the voltage induced on the sensor, constraints are set by limit the maximum values for N_L and d_{avg} . The natural resonant frequency of the sensor is set to 15 MHz which offers a frequency shift range from 10 MHz to 20 MHz in between. Problem would be simplified to a constrained optimization problem:

$$\text{Maximize: } V_{Q2} = \frac{j\omega\mu_0 d_{avg}^2 N_L \cdot I_1 \cdot N_R \cdot d_R^2}{8\sqrt{(d_R^2/4 + x^2)^3}} \text{ at } x=0$$

$$d_{in} \leq 0.1006 - 2g_L(N_L - 1) - 2w_L N_L$$

$$g_L \geq 5 \times 10^{-5}$$

$$\text{Subject to: } w_L \geq 5 \times 10^{-5}$$

$$N_L \geq 2$$

$$L_S = 4 \times 10^{-6}$$

where the constraints of the g_L and w_L are from the fabrication resolution which can be improved using precise microfabrication techniques.

TABLE 4.1 Optimal design results for maximizing the power on sensor.

	d_{in} (mm)	g_L (μm)	w_L (μm)	N_L
Optimum	36.9289	61.9337	50	6.0880
Rounding	37	60	50	6
V_{Q2} (V)	1.5965			

Generally, without constraint on the value of inductance, the optimization results for maximizing the power on sensor is shown in table below:

TABLE 4.2 Optimal design results for maximizing the power on sensor.

	d_{in} (mm)	g_L (μm)	w_L (μm)	N_L
Optimum	33.6000	50	50	335.4999
Rounding	37	50	50	336
V_{Q2} (V)	280.9612			

This design consideration results in the maximum value of V_{Q2} on the sensor. Actually, to maximize V_{Q2} equals to maximize M (equation 4.7). For track with strong conductivity, R_S of the sensor is measured around 2Ω , which is so small to be neglected, and Equation 4.17 can be simplified to the expression below

$$u_{Q2} = j\omega M I_1 \quad 4.28$$

where $\omega=2\pi f$, f is set to a frequency range 10 MHz to 20 MHz and I_l is the maximum current in the reader coil. Then, we get

$$|V_{Q2}| = \omega M I_1 \quad 4.29$$

Based on Equation 4.7, for a decided reader coil, to maximize M equals to maximize the product of $N_L A_S$, in which N_L is the number of turns and A_S is the average area of the sensor planar spiral inductor, respectively. As we mentioned, to minimize the size of the sensor A_S is one of the objectives. Then our objectives on inductive powering become

Maximize N_L

Minimize A_S

The other more general objective on PSI design is to maximize the quality factor. The quality factor of an inductor is defined as the ratio of peak magnetic energy minus peak electric energy to energy loss in one cycle which can be simplified as follow

$$Q_L = \frac{2f\pi L_S}{R_S} \quad 4.30$$

where R_S is the total resistance of the sensor, the summation of the resistance of PSI and IDC. The resistance of the PSI R_L due to the sheet resistance, skin effect, proximity effect and turn-bent resistance, which are briefly discussed by Musunuri et al [54]. The sheet resistance for spiral inductor varies between 0.03 and 0.1 Ω/m^2 . The series resistance of the inductor increases with frequency due to skin effect as

$$R_{sk} = \frac{\rho l}{2\pi f \delta (1 - e^{-h_l/\delta})} \quad 4.31$$

where ρ is the resistivity, f is frequency, h_l is the turn thickness and δ is the skin depth which is given by

$$\delta = \sqrt{\rho / (\pi f \mu_0)} \quad 4.32$$

It is shown that the skin effect is frequency dependent and it is calculated that skin depth is about 17 μm at 15 MHz, which is very close to the metal trace thickness of the spiral inductor. It can not be neglected. However, the resistance due to this skin effect is calculated about $2.0575 \times 10^{-11} \Omega$ at 19 MHz with inductance of 4 μH , which is very small compared to the total resistance which is about 6.3293 Ω . Therefore, the skin effect is neglected in our design.

Proximity effect takes place when a conductor is under the influence of a time varying magnetic field produced by a nearby conductor carrying time varying current. In [54], it is shown that the proximity effect between the turns of a spiral that are in the same plane can be neglected up to 1 GHz.

The resistance due to the turn-bend at each corner of the turn of the inductor has an impact on the total resistance. There are four 90° turns for each turn of the metal trace in the spiral inductor. The bend alters current flow to yield higher resistance. The total resistance of the spiral inductor including this bend resistance is given by

$$R_L = R_{st} \left[\frac{(4N_L - 2)(d_{in} + g_L N_L)}{w_L} + (2N_L - 1)(2N_L - 4) + 4N_L R_t \right] \quad 4.33$$

where R_{st} is the sheet resistance of the metal in Ω/square (0.03 to 0.05, typically), and R_t is the turn-bend factor (2.5, typically).

The series resistance of the interdigital capacitor due to the skin effect is given

$$R_C = \frac{4l_c \sqrt{\rho \pi \mu_0 f}}{3 [N_c \omega_c + (N_c - 1) g_c]} \quad 4.34$$

The total resistance is

$$R_S = R_L + R_C \quad 4.35$$

Therefore, in order to maximize the quality factor, one can maximize the inductance and minimize the resistance. Practically, the spiral inductor should have a lower number of turns with wider conductive trances to get a lower resistance. However, more number of turns results in a greater value of L_S meanwhile. Figure 4.10 shows the Q factor as a function of geometric variables: w_L and N_L at different frequencies.

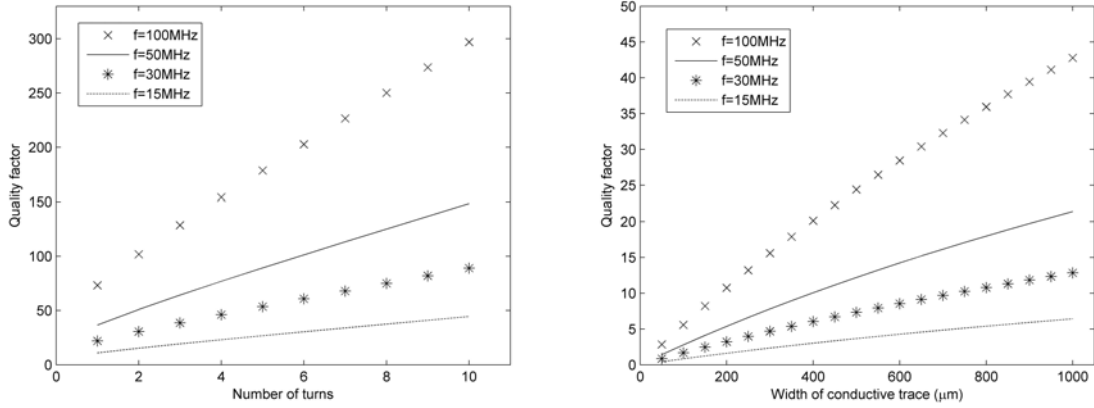


Figure 4.10 Q versus w_L at $N_L = 4.5321$ and versus N_L at $w_L = 741.6971\mu\text{m}$ with $d_{in} = 32.9177\text{mm}$ and $g_L = 50\mu\text{m}$.

Problem to maximize the Q -factor can be described as below

$$\text{Maximize: } Q_L = \frac{2\pi f L_S}{R_S}$$

$$d_{in} \leq 0.1006 - 2g_L(N_L - 1) - 2w_L N_L$$

$$g_L \geq 5 \times 10^{-5}$$

$$\text{Subject to: } w_L \geq 5 \times 10^{-5}$$

$$N_L \geq 2$$

$$L_S = 4 \times 10^{-6}$$

TABLE 4.3 Optimal design results for maximizing the Q -factor on PSI.

	d_{in} (mm)	g_L (μm)	w_L (mm)	N_L
Optimum	32.9177	50	7.4170	4.5321
Rounding	32.92	50	7.42	4.5
Q-factor	31.7572			

The optimization results show us that the maximum Q factor for a spiral inductor with a self inductance about $4 \mu\text{H}$ is about 32. It is also discovered in the results that this maximum Q factor is realized by applying wider trace and lower number of turns. After we discuss the consideration on IDC design in next section, a briefly expression for the optimization problem with objectives and constrains will be given.

4.3.2 Consideration on Strain Sensing

The general goal of the strain sensing element design is to find a maximum sensitivity, a linear sensing range and a minimum geometric size. Based on the analysis of the strain effect on the IDC capacitance, it is shown that the change in capacitance shows great sensitivity with big η . Actually, the influence of r and ε_2 on the capacitance change are the other important parameters, which will be talked about in chapter 5 sensitivity enhancement. The reason that we do not need to give special treatment to those two parameters here when we do the sensor design is because r is already very small (≤ 0.1) and the application of the finite strain sensitive layer with ε_2 would not shift the resonant frequency too much to get out of the sweep frequency range.

Geometry constraints includes that the finger length of the IDEs can not be bigger than the inner diameter of the SPI, the summation of the total finger width and total gap width is smaller than the inner diameter of the SPI. The manufacturing facility limits the fabrication resolution that the width of the gap and electrode can be no smaller than $100 \mu\text{m}$. Number of interdigital electrode pairs is more than 2. The capacitance of the IDC together with the

appropriate PSI with an inductance L_S will make the resonant frequency to 15 MHz.

Therefore, the geometric optimization problem for IDC is described below:

$$\begin{aligned}
 &\text{Minimize: } d_{out} = d_{in} + 2g_L(N_L - 1) + 2w_L N_L \\
 &\quad L_S \cdot C_S = 1/\omega_0^2 \\
 &\quad g_C \geq 1 \times 10^{-4} \\
 &\quad w_C \geq 1 \times 10^{-4} \\
 &\quad l_C \leq d_{in} - 2(g_C + w_C) \\
 &\quad N_C(g_C + w_C) \leq d_{in} \\
 &\text{Subject to: } N_C \geq 4 \\
 &\quad d_{in} \leq 0.1006 - 2g_L(N_L - 1) - 2w_L N_L \\
 &\quad g_L \geq 5 \times 10^{-5} \\
 &\quad w_L \geq 5 \times 10^{-5} \\
 &\quad N_L \geq 2 \\
 &\quad l_C \geq 0 \\
 &\quad N_L(g_C + w_C) = l_C
 \end{aligned}$$

TABLE 4.4 Optimal design results for minimizing sensor dimension.

	d_{in} (mm)	g_L (μm)	w_L (μm)	N_L	l_C (mm)	g_C (μm)	w_C (μm)	N_C
Optimum	13.8544	50	50	10.5240	13.3205	52.8916	80.5949	99.7890
Rounding	13.85	50	50	10.5	13.32	50	80	100
d_{out}	15.8592 mm							

As noticed in Figure 3.7, the capacitance changes greater with the same amount of strain applied with a smaller fill ratio than the one with a bigger fill ratio. Therefore, the objective on maximize the strain sensing sensitivity can be simplified to find the maximal metal ratio to all the reasonable constraints. This objective will be realized together with all the other objectives and discussed in the last section.

4.3.3 Multi-objective Optimization

The optimization involved in our sensor design is a multi-objective optimization problem, which is because the optimization problem involves more than one objective function. Actually, most search and optimization problems naturally involve multiple objectives. The extremist principle mentioned above cannot be applied to only one objective, when the rest of the objectives are also important. Moreover, objectives in optimization problems are always conflicting and each objective corresponds to a different optimal solution. One of the most important solutions is *trade-off*. The irony question comes that none of the solutions is the best with respect to each of the objectives. Without further information, no solution from the set of optimal solutions can be said to be better than any other.

Although multi-objectives result in a set of optimal solutions, from a practical standpoint only one solution is needed from all of those choices. Approach for the solving this dilemma is to find the trade-off, which includes more considerations on making a choice. An ideal and simpler multi-objective optimization procedure, called a preference-based multi-objective optimization by Deb in [52], can be described in the schematic below in Figure 4.11.

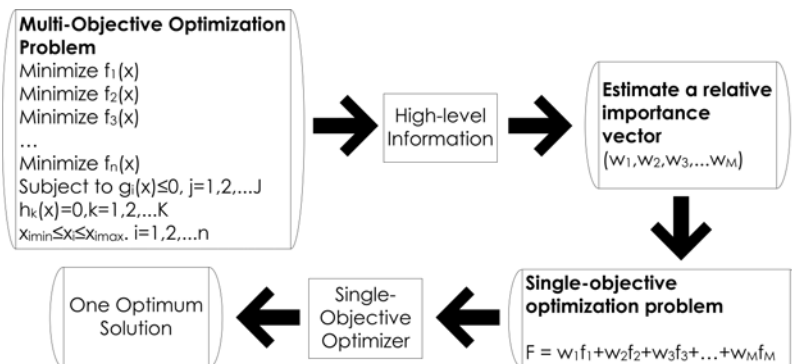


Figure 4.11 Schematic of a preference-based multi-objective optimization procedure.

It can be seen that the trade-off solution obtained by using the preference-based strategy is largely sensitive to the relative preference vector w used in forming the composite function. A change in this preference vector would result in a different solution. This classical multi-objective optimization method which converts multiple objectives into a single objective by using a relative preference vector of objectives helps to make the problem straightforward. Once all the objective goals involve in the problem are ready, the most important step is to find a particular preference vector and the composite function.

With this technique in mind, let us review our design problem. In section 4.3.1, objective goals include maximize the inductive power on the sensor, maximize the quality factor of the planar spiral inductor. The objectives can be extended to have more design considerations which depend on the particular applications. In section 4.3.2, objectives that are being mentioned includes that minimize the geometric dimension of the entire sensor, maximize the sensitivity of the sensor performance. Again, more objectives can be added depending upon the applications. As noticed, minimizing the geometric dimensions would cause a decreasing inductive coupling and maximizing the quality factor would decrease the length of the spiral inductor which will also decrease the voltage generated on the sensor. These are known as the conflicting objectives and the others are non-conflicting objectives which are basically all nonlinear. Multi-objective nonlinear programming is utilized to handle large number of objectives and complicated constraints and helps to avoid artificial fix ups. By using the technique of preference vector, which is actually a weighted sum approach, the simplified composite function is achieved. Search optimum point is carried out using Penalty Search.

The weighted vector should be carefully decided, which is actually based on application and all of the related objectives. In our case, minimize the sensor size and maximize the sensitivity about the measurands seems to be the most important objectives than maximize the detecting distance and signal strength. Some more important characteristics also include maximize the Q factor of the PSI for data transmission and also specific requirement for various applications.

4.3.4 Design Results and Discussions

The numerical experiments are carried out using nonlinear programming and multi-objective optimization with penalty search in MATLAB. Any specific requisitions for different applications can be possibly included in the objectives. Among all these objectives, minimize the sensor size, maximize detecting distance and maximize the Q factor are the most important ones that need to be carefully designed, which affect the choice of the weighted vector in the optimization process. Again, these assumed objectives are just for our specific design consideration. Authors can add any geometric dependent objectives.

- Objectives:** Minimize sensor size;
Maximize voltage generated on sensor;
Maximize sensor quality factor;
Maximize the strain sensitivity;
- Subject to:** All of the geometry constraints;
All of the manufacturing facility constraints;
Working frequency constraints

TABLE 4.5 Multi-objective optimization sample results

Experiment.1 $w = \{1, 0, 0, 0\}$												
	$d_{in}(mm)$	$g_L(\mu m)$	$w_L(\mu m)$	N_L	$l_C(mm)$	$g_C(\mu m)$	$w_C(\mu m)$	N_C	$d_{out}(mm)$	$U_{Q2}(V)$	Q	η
Optimum	13.85	50	50	10.52	13.32	52.89	80.59	99.79	15.86	0.43	1.01	0.60
Experiment.2 $w = \{0.99, 0, 0, 0.01\}$												
	$d_{in}(mm)$	$g_L(\mu m)$	$w_L(\mu m)$	N_L	$l_C(mm)$	$g_C(\mu m)$	$w_C(\mu m)$	N_C	$d_{out}(mm)$	$U_{Q2}(V)$	Q	η
Optimum	18.99	50	72.17	6.63	18.50	61.84	60.19	151.63	20.51	0.48	1.02	0.49
Experiment.3 $w = \{0.97, 0, 0, 0.03\}$												
	$d_{in}(mm)$	$g_L(\mu m)$	$w_L(\mu m)$	N_s	$l_C(mm)$	$g_C(\mu m)$	$w_C(\mu m)$	N_c	$d_{out}(mm)$	$U_{Q2}(V)$	Q	η
Optimum	11.34	107.62	50	35.49	8.19	50	736.00	10.43	22.31	1.87	2.07	0.94
Experiment.4 $w = \{0.895, 0, 0.005, 0.1\}$												
	$d_{in}(mm)$	$g_L(\mu m)$	$w_L(\mu m)$	N_L	$l_C(mm)$	$g_C(\mu m)$	$w_C(\mu m)$	N_C	$d_{out}(mm)$	$U_{Q2}(V)$	Q	η
Optimum	34.23	50	4286.39	7.66	27.55	50	1621.89	16.48	100.60	6.48	31.39	0.97
Experiment.5 $w = \{0.89, 0, 0.01, 0.1\}$												
	$d_{in}(mm)$	$g_L(\mu m)$	$w_L(\mu m)$	N_L	$l_C(mm)$	$g_C(\mu m)$	$w_C(\mu m)$	N_C	$d_{out}(mm)$	$U_{Q2}(V)$	Q	η
Optimum	35.10	50	5777.28	5.63	30.84	50	1013.81	28.99	100.60	4.82	31.62	0.96
Experiment.6 $w = \{0.7995, 0.0005, 0.1, 0.1\}$												
	$d_{in}(mm)$	$g_L(\mu m)$	$w_L(\mu m)$	N_L	$l_C(mm)$	$g_C(\mu m)$	$w_C(\mu m)$	N_C	$d_{out}(mm)$	$U_{Q2}(V)$	Q	η
Optimum	35.85	50	8566.86	3.76	33.95	50	425.35	71.42	100.60	3.26	31.83	0.89
Experiment.7 $w = \{0.79, 0.01, 0.1, 0.1\}$												
	$d_{in}(mm)$	$g_L(\mu m)$	$w_L(\mu m)$	N_L	$l_C(mm)$	$g_C(\mu m)$	$w_C(\mu m)$	N_C	$d_{out}(mm)$	$U_{Q2}(V)$	Q	η
Optimum	30.88	50	4776.35	7.23	26.17	50	1127.00	22.24	100.60	5.81	31.53	0.96

Example results of the geometric variables and objectives at different weighted vectors are shown in the table above. In the first experiment, we are using $w=\{1,0,0,0\}$, ones can see that the results show the minimum size of the sensor is about 1.6 cm. In order to increase the strain sensitivity, it is shown that ratio η is greatly increased in experiment 2--3. Ones can maximize the width and minimize the number of turns to improve the Q factor in experiment 4--5. It is shown that the width and the number of turns are greatly increased to get a bigger voltage on sensor in experiment 6--7. The weighted vector should be carefully selected based on the application requirements and objectives. In order to simplify the selection of w , our optimization method also allows ones to specify minimum requirements to the variables, such as the minimum Q factor or the minimum voltage generated on sensor.

The effective design of planar resonators for wireless sensing applications requires an efficient optimization process to obtain a geometry that optimizes the application requirements. We have developed an optimization model, based on a weighted vector technique and penalty function, to harmonize the often conflicting objectives: minimize the sensor size, maximize the detection distance, maximize the quality factor, and maximize the

strain sensitivity for the passive wireless sensing. Through the selection of weighted vector, the single or multi-objective optimization is realized to get a rapid configuration to the geometric variables of planar resonator. The technique can provide designers with a systematic and efficient approach to achieve the optimization of the device based on the application requirements.

5 SENSITIVITY ENHANCEMENT

Piezoelectric effects are the ability of a material to respond to a voltage applied across it by deforming promptly, and the ability of the material to generate a voltage across opposing faces when a deformation is applied to it. Pyroelectric effects are generally similar, except that they involve thermal processes instead of mechanical processes. For many years, piezoelectric materials have been used in a wide range of sensor and actuator applications. Among these materials, piezoelectric polymers, discovered 30 years later after the discovery of piezoelectricity in crystal, have the advantage of being usable as mechanically flexible sensors and actuators with large areas and various shapes as well as in transducers with good acoustical coupling to air or water. Furthermore, these polymers are interesting because of their various piezoelectricity as well as pyroelectricity. The dipoles rotational mechanism in the polymer is the prerequisite for these properties. Piezo- and pyro-electricity occur based on a change of the dipole density during the application of mechanical strain/stress, electrical field and temperature. Moreover, this dipole density change varies the permittivity of piezoelectric materials. This chapter starts with theoretical derivation of the strain dependent permittivity in piezoelectric material. Experimental investigation on the strain dependent dielectric permittivity $\varepsilon(\tau)$ have been carried out.

5.1 Strain-dependent Permittivity

The largest part of the piezoelectric response is due to a change in the density of the oriented crystallite dipole moments. The dipole orientation is measured by polarization which

is a function of temperature, stress (or strain), electric field for piezoelectric material and frequencies. Under the condition of constant temperature and zero electric field, the polarization P results from an applied stress σ or strain τ . A linear relationship that exists between P and the applied stress or strain field shows the phenomenon theoretically in piezoelectric materials. Due to material anisotropy, P is a vector with three orthogonal components in the 1, 2, and 3 directions [55].

$$P_i = d_{ij}\sigma_j = e_{ij}\tau_j \quad 5.1$$

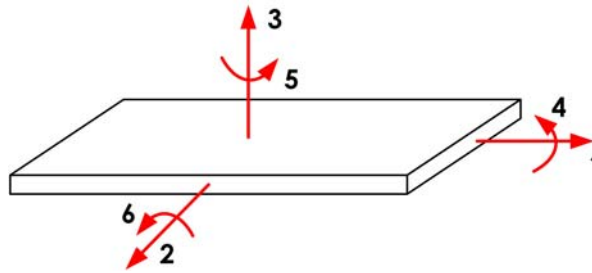


Figure 5.1 Tensor directions.

The polarization acts as a contribution on the intrinsic electric field which changes the effective electric field and thus the capacitance. In order to understand the strain effect on the dielectric permittivity, let us derive the most general form of the linear relation of a piezoelectric dielectric material in an electric field from the classical thermodynamic relations. The thermodynamic potential in piezoelectric material can be expressed

$$\Phi = U - ST - \tau_{ik}\sigma_{ik} - D_i E_i \quad 5.2$$

where Φ is the thermodynamic potential per unit volume, S is the entropy per unit volume, T is the temperature of the unit volume, σ_{ik} and τ_{ik} are strain and stress tensors, E_k and D_i are electric field and electric displacement respectively. For an isothermal process, the differential of the thermodynamic potential is given

$$d\Phi = -\tau_{ik}d\sigma_{ik} - D_i dE_i \quad 5.3$$

And we have

$$dD_i = \left(\frac{\partial D_i}{\partial \sigma_{ik}} \right)_{\tau,s} d\sigma_{ik} + \left(\frac{\partial D_i}{\partial E_i} \right)_{\sigma,s} dE_i \quad 5.4$$

On the other hand, for any dielectric materials, the linear relationship between the electric displacement and electric field is derived using Green's theorem

$$\text{div}E = \frac{4\pi\alpha}{\epsilon_0} - \frac{4\pi}{\epsilon_0} \text{div}P \quad 5.5$$

where E is the electric field, α is the charge density, ϵ_0 is the vacuum permittivity, and P is the dipole moment per unit volume or the polarization of the dielectric.

$$\text{div}(\epsilon_0 E + 4\pi P) = 4\pi\alpha \quad 5.6$$

$$D = \epsilon_0 E + 4\pi P \quad 5.7$$

In addition, P is proportional to E for polarization materials written in tensor form to keep consistency

$$P_i = \chi_{ik} \epsilon_0 E_k \quad 5.8$$

Relation in Equation 5.7 has a consequence for polarization materials

$$D_i = (4\pi\chi_{ik} + 1)\epsilon_0 E_k = \epsilon_{ik} E_k \quad 5.9$$

Dipole may exist in absence of an external electric field. The application of an electric field has the effect of orienting these molecules in the dielectric material parallel to the field, and the resulting dipole moment is likewise proportional to the external field. For piezoelectric or pyroelectric material in a given electric field, the dipole moments undergo external strain or thermal agitation, and these agitations work against the establishing of resulting dipole moments. As indicated in Equation 5.1, the dipole moment in piezoelectric

material has an external term which is proportional to applied strain or stress field. The total dipole moment or polarization then has the expression below

$$P_i = \chi_{ik} \varepsilon_0 E_k + e_{i,jk} \tau_{jk} \quad 5.10$$

Adding the piezoelectric terms to Equation 5.7, we have

$$D_i = \varepsilon_0 E_k + 4\pi (\chi_{ik} \varepsilon_0 E_k + e_{i,jk} \tau_{jk}) = \varepsilon_{ik}^\sigma E_k + 4\pi e_{i,jk} \tau_{jk} \quad 5.11$$

where ε_{ik}^σ indicates the dielectric permittivity at zero applied stress. The second term on the right side of the equation acts as an additional part on the apparent dielectric permittivity

Now the change of electric permittivity due to mechanical input can be calculated similarly to Equation 5.1 by looking for the effective electric field. From the definition of dielectric permittivity, the effective electric field affected by the external loads generates an effective or apparent permittivity. In other words, polarization orientation due to mechanical loads affects the permittivity of the piezoelectric materials.

As we know, most of the piezoelectric polymers that are used for electro-mechanical transducer application are pre-poled, which makes the polymers are sensitive in some directions, while the others not. These anisotropic properties are even enhanced during the deformation of the material by introducing additional polarization due to the external field. The introduced polarization appends the other component on the electric field. In equations above, although polarization is generated because of the external electric field, it is noticed that the material response to the external field and the induced polarization, total polarization, and applied field are all parallel. These are known as the isotropic materials. In the anisotropic piezoelectric polymer, the material response depends on the relative direction of

the applied field and the strain induced polarization. The magnitude and the direction of the strain induced polarization dynamically change the material response.

Because polarization can not follow an electric field in a high frequency field, permittivity has a dependence on the frequency. This dependence is known as dielectric dispersion. In the microwave region greater than 10 GHz, it becomes impossible for dipolar polarization to follow the electric field. For the frequency range bigger than 10 THz, electronic polarization loses its response to the electric field. In our application as we mentioned, interrogation field has a frequency range from 10 MHz to 20 MHz with constant field strength. The statistic polarization at constant mechanical load is aligned parallel to the electric field and follows the change of the electric field. This enables a static constant permittivity over all of the frequency range.

A sheet of piezoelectric polymer (PVDF) as a dielectric layer is attached to the top of IDC. With the applied tensile or compressive strain applied to the sensor in 1-direction as indicated in Figure 5.1, Equation 5.11 can be written as the form below

$$D_3 = \varepsilon_{33}^{\sigma} E_3 + 4\pi e_{31} \tau_1 \quad 5.12$$

where e_{31} is positive for PVDF, and τ_1 is positive for tensile strain and negative for compressive strain. Therefore, the strain dependent permittivity is about to increase with tensile strain and decrease with compressive strain. Moreover, in Chapter 3 and Chapter 4, the strain affections on the value of capacitance and inductance are investigated. When the electrodes are parallel to the strain direction, the changes of the capacitance and inductance influence the variation of frequency in the same way: capacitance and inductance increasing with the tensile strain and decreasing with the compressive strain. The strain dependent permittivity helps to magnify the change in capacitance and substantially amplify the

frequency shift. Compared to the sensor without PVDF, sensors with the PVDF dielectric material exhibit a better sensitivity.

Assume the dielectric permittivity has a linear relationship with the applied strain, although practically the polarization goes saturated with the increasing loads.

$$\varepsilon_{33} = \frac{\partial D_3}{\partial E_3} = \varepsilon_{33}^{\sigma} \frac{\partial E_3}{\partial E_3} + 4\pi e_{31} \frac{\partial \tau_1}{\partial E_3} = \varepsilon_{33}^{\sigma} + 4\pi e_{31} d_{31} \quad 5.13$$

The capacitance change at parallel configuration with PVDF with the applied strain compared to the one without PVDF can be expressed below

$$C_{PVDF} = \left(1 + \frac{4\pi e_{31} d_{31}}{\varepsilon_{33}^{\sigma}} \right) \cdot C \quad 5.14$$

Therefore, the sensitivity is improved by $(1 + 4\pi e_{31} d_{31} / \varepsilon_{33}^{\sigma})$.

Based on this theoretical analysis, experimental investigations have been held. The stress dependence of the dielectric constant in PVDF has not been so concerned that this investigation has no early reference to compare with.

5.2 Experiment Investigation

The effects of tensile strain and temperature on the dielectric permittivity of the previously poled PVDF thin film were studied by the means of microstrip transmission line method at ultra high frequency range from 500 MHz to 1300 MHz. Vector Network Analyzer (VNA) and GPIB board connecting VNA to PC data acquisition were used in measuring the S-parameters in real time, and dielectric constants were calculated based on the interconnection model of the transmission line method.

Microstrip transmission line method [65, 66] employs vector network analyzer (VNA) and transmission line built on the PVDF film to measure all of the complex reflection and transmission coefficients for characterizing PVDF material. Frequency variations of transmission parameters were extracted directly from S-parameter measurement which is based on the classical Telegrapher's transmission line equation. The complex permittivity of the PVDF film can be calculated using propagation constant measurement. The relationship between the propagation factor and the S-parameters are shown below in Equation 5.15 [56].

$$e^{-\gamma l} = \left\{ \frac{1 - S_{11}^2 + S_{21}^2}{2S_{21}} \pm \left[\frac{(S_{11}^2 - S_{21}^2 + 1)^2 - (2S_{11})^2}{(2S_{21})^2} \right]^{\frac{1}{2}} \right\}^{-1} \quad 5.15$$

where l is the length of the transmission line and γ is the complex propagation constant. The effective permittivity can be calculated

$$\varepsilon_e^* = \frac{\lambda_0}{\lambda_e} \quad 5.16$$

where λ_0 and λ_e is the wavelength in the free space and in the material which can be calculated

$$\lambda_0 = \frac{v_C}{f} \quad 5.17$$

$$\lambda_e = \frac{2\pi}{\beta} \quad 5.18$$

where β is the phase factor which is the imaginary part of the complex propagation constant; v_C is the light speed in free space and f is the measure frequency. The relative permittivity of the material then can be calculated

$$\varepsilon = \frac{2\varepsilon_e^* - (1 - q)}{1 + q} \quad 5.19$$

where q is the geometry coefficient which can be calculated

$$q = \frac{1}{\sqrt{1+12h/w}} \quad 5.20$$

where w is the width and h is the thickness of the transmission line.

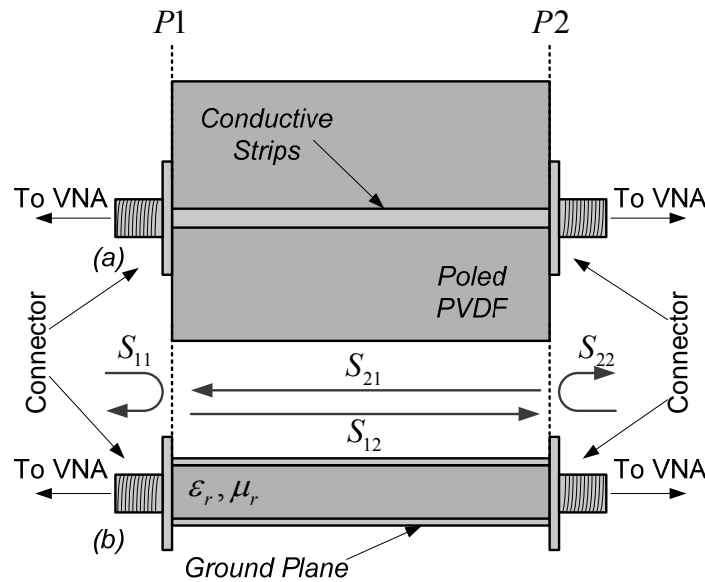


Figure 5.2 Transmission line test fixtures.

In order to perform S-parameter measurements, an experimental setup was designed and implemented, as shown in Figure 5.2. The samples of unmetallished PVDF films from Precision Acoustics Ltd., 110×10^{-3} m in thickness and 25×10^{-3} m in width, were cut to 0.02 m in length, and anchored horizontally using double-coated adhesive tape onto a rigid support. A tray to carry weights shown in Figure 5.3 was attached to the end of the film strip. Transmission line was built on one side of the film and ground on the other side using copper foil tape with conductive adhesive. Cables that being connected to the Agilent 8719 ES network analyzer were adhered on the table to make sure that there was no movement between the cable and transmission line during the loading process. PC was connected by GPIB connector to record all of the S-parameters in the frequency range from 500 MHz to

1300 MHz. At the same time, a temperature probe was used to record temperature close to the midpoint of the film.

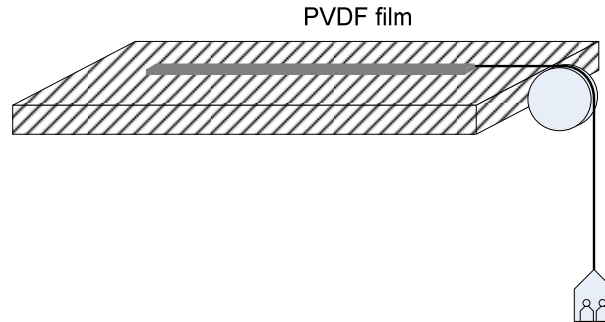


Figure 5.3 Experimental Setup.

The S-parameters and temperatures of the stressed or heated PVDF film were recorded after the test condition being kept at least 1 minute.

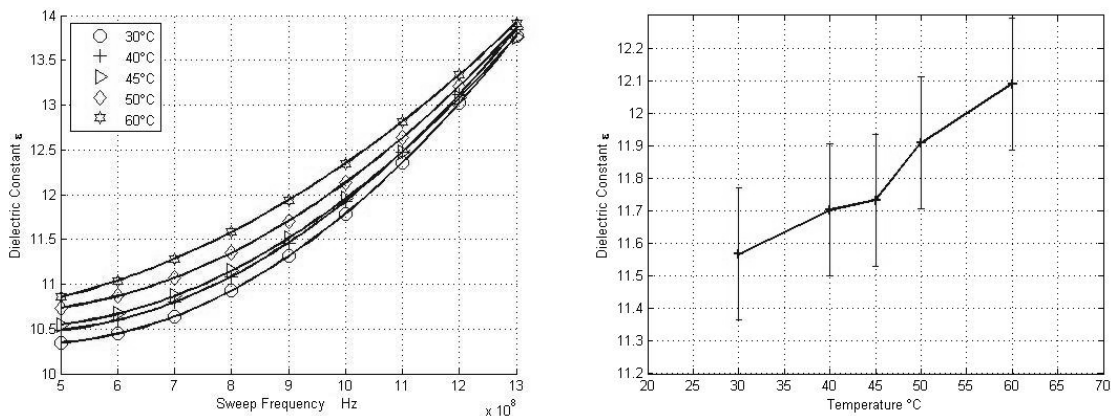


Figure 5.4 The variation of the dielectric constant with the increasing temperature.

Figure 5.4 shows the frequency responses of the static dielectric constant ϵ at atmospheric pressure. There is frequency dependence at the temperature range from 30 °C to 60 °C. The $\epsilon(T)$ increases with elevating temperature because of the dipolar contributions which become activated at higher temperatures. Our measurement result of the dielectric constant at 24 °C show a good agreement with the datasheet from the manufacturer. Our results in Figure 5.4 extend a higher frequency range than these earlier studies but still show

a clearly linear response. This increasing temperature reduces the tension on the molecules, increases the mobility, and consequently increases the value of the static dielectric constant by increasing the dipolar orientation.

Figure 5.5 shows the effective tensile strain dependence of PVDF dielectric constant $\epsilon(\tau)$ at room temperature of 24 °C and a constant humidity for the same sample used in the temperature tests. The application of the tensile stress which is perpendicular to the polarization field results in a change in the polarization. The positive tensile stress would generate a negative polarization which acts an additional part on the dielectric constant. As noted, Figure 5.5 shows a great linear result on the change of dielectric constants versus the increasing effective strain. The strain dependence of the ϵ of PVDF has not been so concerned that no early data can be compared with the present $\epsilon(\tau)$ results.

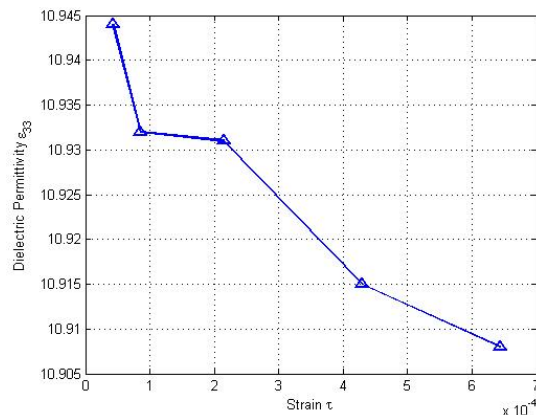


Figure 5.5 The variation of the dielectric constant with the increasing stress.

The results from this study concluded that the influence of the intrinsic polarization in poled PVDF on the dielectric constant is due to the stress or strain field, elevating temperature, or applied electric field. All these external fields create an additional field-proportional polarization and the effect of this polarization can be considered as an additional part of the electric field and the dielectric constant.

6 SENSOR FABRICATION

Based on sensing analysis, inductive power and entire sensor optimization, in this chapter we will discuss sensor fabrication using fabricating microelectromechanical system (MEMS) technique. Actually, MEMS refers to a collection of sensors and actuators that can sense its environment and have ability to react to change in that environment with the use of a microcircuit control. This system needs micropower supply, microrelay, and microsignal processing units. Microcomponents make the system faster, more reliable, cheaper and capable of incorporating more complex functions. Micromachining is the fundamental technology for the fabrication of MEMS devices. Basically, bulk micromachining and surface micromachining are the two major micromachining processes of silicon based MEMS fabrication. We will start with the introduction on photolithography one of the most important approach in bulk micromachining. Afterward, based on the sensor design given in Chapter 4, the sensor prototypes are fabricated.

6.1 Pattern Design

Various sensor prototype patterns (shown in Figure 6.1) are designed in Microsoft Visio and printed on transparent plastic papers.

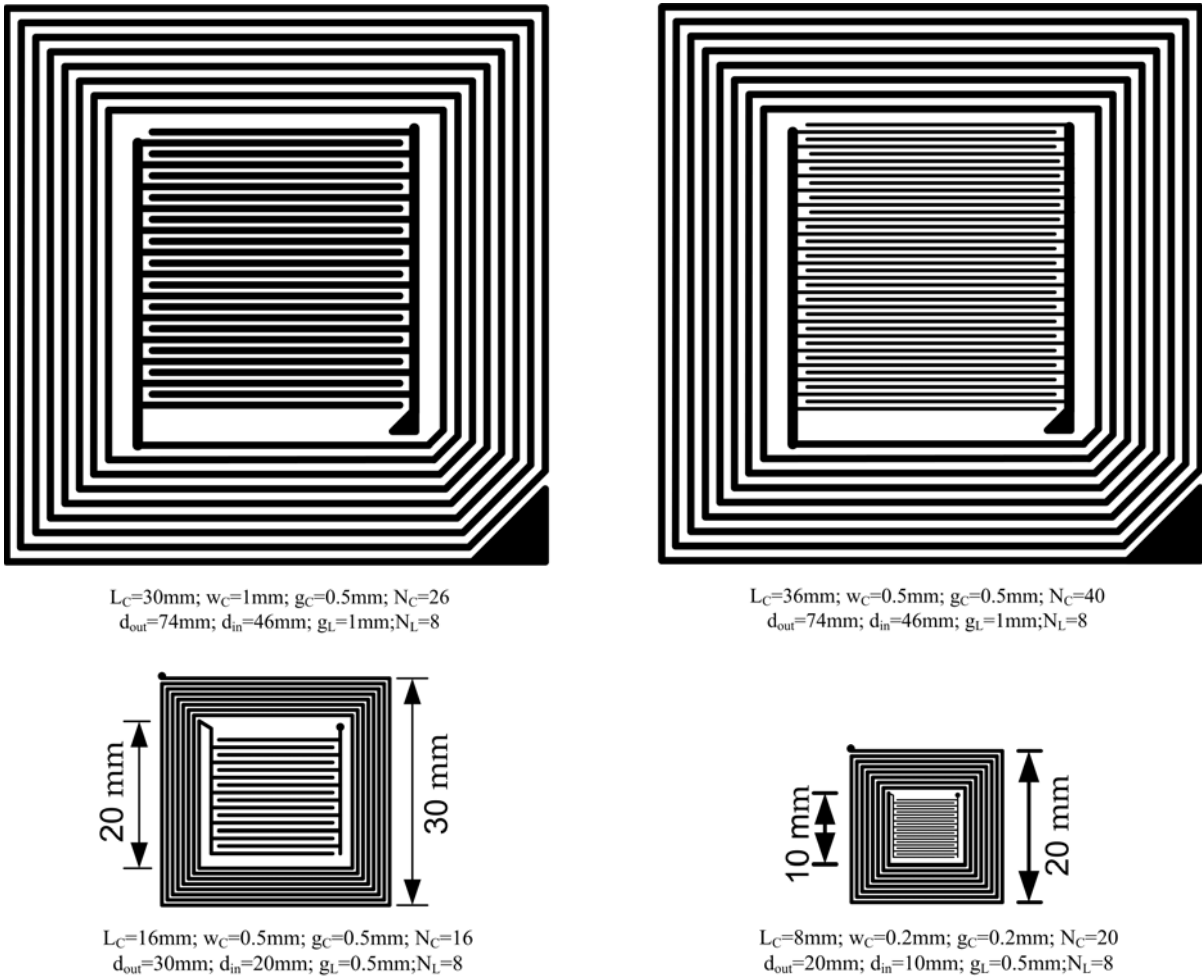


Figure 6.1 Sensor prototype patterns.

6.2 Materials

The pattern-transfer target material for the main circuit of the sensor is DuPont Pyralux AC single-side copper-clad laminate which is an all-polyimide composite of polyimide film on copper foil. Pyralux laminated composites are typically used to produce high reliability, high density circuit of flexibility, rigid-flex, and all-flexible multilayer constructions. Standard Pyralux AC copper-clad products are listed below. Polyimide base substrate thickness are available from 25 μm to 45 μm , rolled-annealed (RA) copper foil weights from

18 μm to 35 μm , and electro-deposited (ED) copper foil weights from 18 μm to 35 μm .

Typical properties are shown in Table 6.2.

TABLE 6.1 Single-sided Pyralux AC product offerings.

Product Codes	Copper thickness μm	Copper type	Polyimide thickness μm
AC182500R	18	RA	25
AC352500R	35	RA	25
AC182500E	18	ED	25
AC352500E	35	ED	25
AC354500E	35	ED	45

TABLE 6.2 Pyralux AC materials properties.

Property	Typical value
Adhesion to Cu (Peel Strength) N/mm (lb/in)	1.19 (6-7)
Dimensional Stability %	-0.02~-0.04
Dielectric Constant (at 1 MHz)	3.7
Dissipation Factor (at 1 MHz)	0.0014
Dielectric Strength kV/mm (kV/mil)	(4.9)
Volume Resistivity megaohms	10^{10}
Surface Resistance megaohms	10^5
Moisture Absorption %	0.94
Propagation Tear Strength g	3.0
Tensile Strength Mpa (kpsi)	(28)
Elongation %	21

6.3 Sensor Fabrication

Sensor fabrication process is shown in the following with noticeable matters suggested within those listed corresponding procedures.

1. The laminated copper clad is cleaned with an acetone 50% solvent to remove the contaminants on the surface. Clean surface condition would offer a better contact for the applied photoresist and provide a good circuit condition. The cleaned copper clad is placed to a flat and rigid plastic plate, because the copper clad is too flexible to be deformed by the

pressure air from the vacuum pump. In this case, the copper clad should be carefully attached without any distortion on the clad and make sure that the clad is flat. The reason that a flat clad and a rigid support is needed is to ensure a uniform application of the photoresist.

2. Turn on the yellow filtered light with all the other light off before open the bottle seal of photoresist. Apply a thin layer of photoresist on the surface of the copper clad and make it spread all over the surface instead of just dropped on one point on the surface. Turn on the vacuum pump and ensure the plastic support with the copper clad is aligned with the center line of the aperture from the spin. Unbalanced placement of the plastic plates will cause the plates slip of the support during the high speed spinning. Accelerate the spin speed from 0 rpm to 1300 rpm slowly and keep the speed at 1300 rpm for 120 seconds to make sure a uniform thickness of photoresist layer applied on the copper clad. After that, reduce the speed slowly until the plate stops spinning before turning off the vacuum pump. Remove the copper clad together with the support plate carefully. Any incautious scratch would break the designed circuit. Put the copper clad into the pre-heated oven at 80 °C for 30 minutes and cool to ambient temperature.

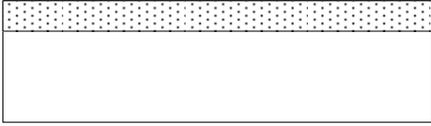
3. The transparent photographic film containing the pattern of the desired circuit is aligned on the soft baked copper clad. Make sure that the ink side on the pattern film is the side that attached to the photoresist. Turn on the vacuum pump until the pattern film is perfectly attached to the copper clad. The reason for this is because of the thickness of the pattern film would cause an UV light cut off on the copper clad which will make the feature smaller than the desired pattern. Turn on the UV light and start the timer for 90 seconds.

4. Remove the mask pattern film and replace the copper clad into the developer solvent which is 1:1 solution of AZ developer and deionized water. Hold the clad with tweezers and agitate mildly until the photoresist which is exposed to the UV light has been fully dissolved leaving a legible patterned part on the copper which is the same as the mask pattern. The development should be done uniformly to make sure that there is not over-development on one part and under-development on the others. Plunge the developed copper clad with photoresist immediately to the deionized water and rinse the clad completely with running water. Dry it before placing it into the hard baking oven. Make sure the clad is absolutely dry is important.

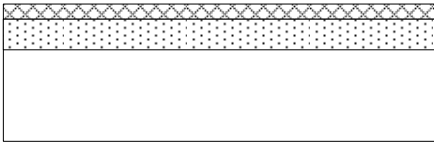
5. Leave the copper clad into the hard baking oven at 120 °C for 60 minutes. Cool it and immerse it into the solution of E1-G PCB board etchant. Hold the clad with tweezers and agitate mildly until the copper which is not covered by the hard-baked photoresist is completely etched away. The etchant can be heated and maintain the temperature at 45 °C to 50 °C if it is needed. Because of the homogeneity of the etchant in all the directions, it is possible that the etchant will cut through the part covered by the photoresist and broken the circuit. Therefore, it is critical to make a uniform etching by agitating continuously and equally. Rinse the etched copper clad with running water and strip the photoresist with the acetone solvent. Clean the copper clad and dry it before use.

Major procedures are briefly shown below in Figure 6.3

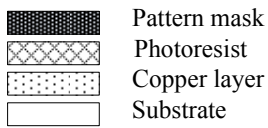
1. Clean the copper layer



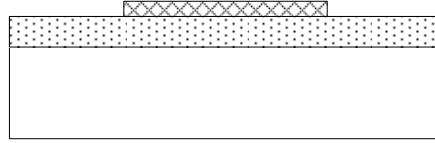
2. Develop PR and soft bake it



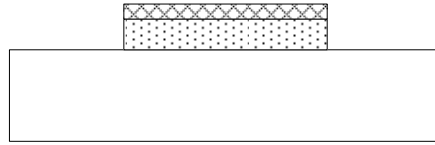
3. Mask the substrate and PR and Expose in UV



4. Remove the mask, develop PR and hard bake it



5. Etch the Cu layer



6. Strip the PR

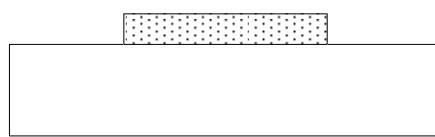
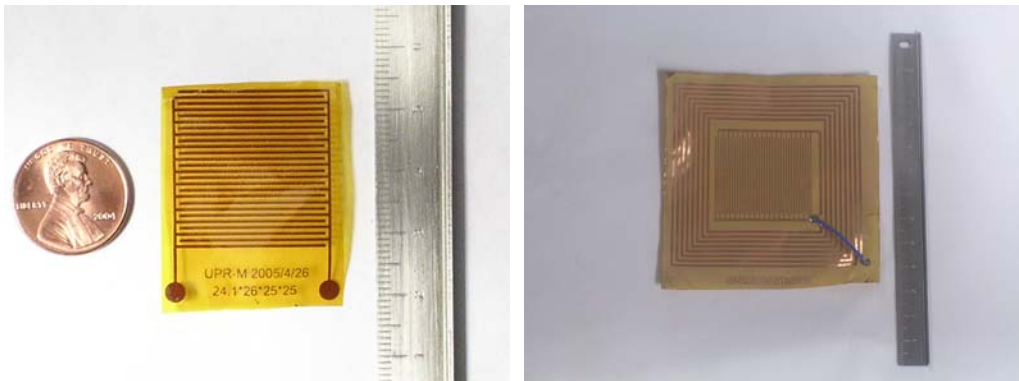


Figure 6.2 Illustration on the sensor fabrication using photolithography.

Fabricated sensors are selected shown in Figure 6.4 below.



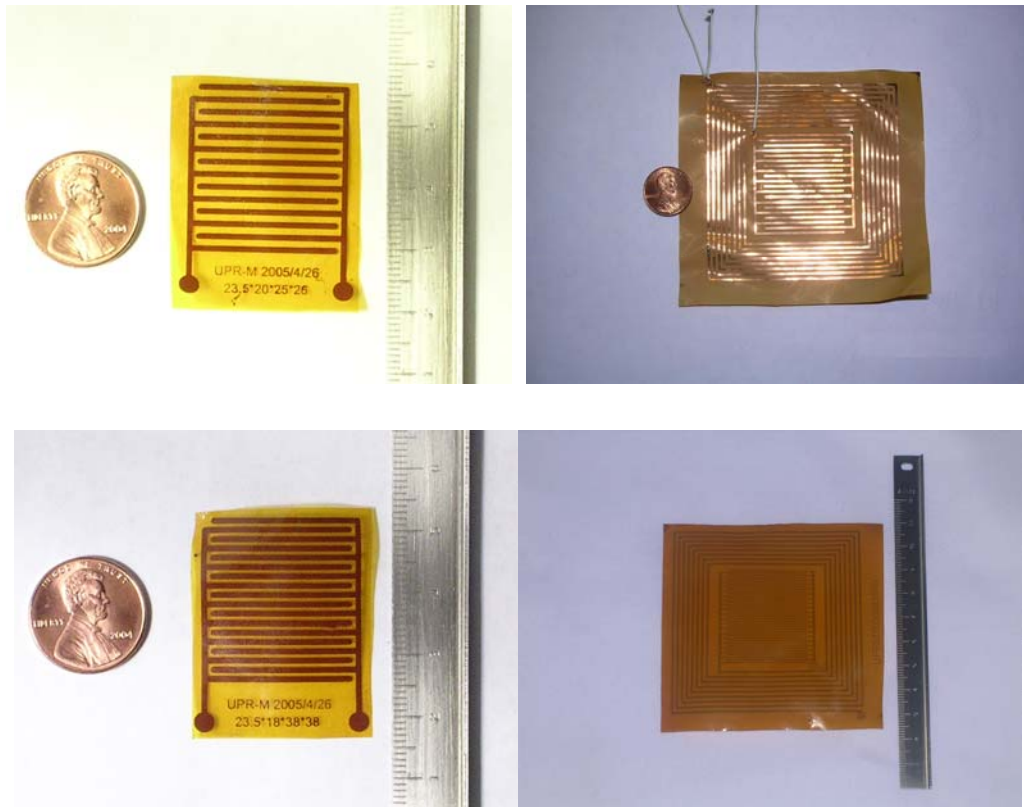


Figure 6.3 Fabricated sensor prototypes.

7 SENSOR READER DESIGN

The proposed novel strain sensor is a passive, wireless, and powerless sensor that can be embedded into structures and devices. Figure 1.5 shows the schematic of the passive strain sensing system. Basically, the reader is composed of a signal generator (transmitter), a signal processor (receiver), and a spiral coil (antenna). The design concept of the transmitter is to generate a strong enough electromagnetic field in the reader antenna by amplifying the current in the antenna and at the same time makes the current working in RF frequency. The voltage measured across the reader coil antenna will be amplified by the reader and these voltage signals will be acquired by the Data Acquisition Card DAQCard-6024E from National Instruments which is designed for laptop application and our reader. MATLAB code for data processing is used to communicate with the DAQCard. Five major parts of the reader: power supply, transmitter, receiver and data acquisition are discussed individually in this chapter.

7.1 Power supply

Regulated power supply is designed to convert high voltage AC mains electricity to a suitable low voltage supply for the oscillator, voltage controlled oscillator (VCO), and operational amplifiers. Transformer helps to get a low voltage AC output. A full bridge rectifier, which is made of four individual diodes, changes the low voltage AC output to a varying DC output. Smoothing filter, which is performed by a large value electrolytic

capacitor, is used to smooth the varying DC to a DC output with a small ripple which is almost suitable for electronics. Voltage regulator is used to provide a very smooth with no ripple DC output and with a fixed voltage.

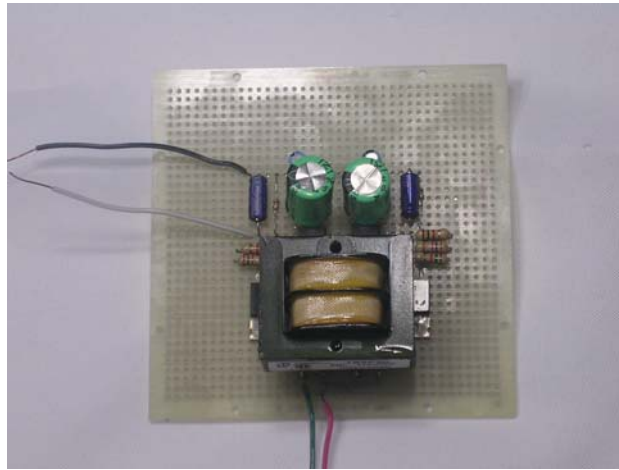


Figure 7.1 Fabricated power supply circuit.

7.2 Transmitter

In order to sweep through the necessary frequency range, the transmit circuit of the sensor reader must be able to produce an appropriate sweep signal. The sensor is designed to resonate at 15MHz, and so we planned our transmit circuitry to sweep from below this frequency to higher frequencies, which eventually settled to a low of near 10MHz to a high of near 20MHz.

In order to produce the sweep signal, we use a voltage-controlled oscillator. LTC-1799 from Linear Technology is chosen. This chip takes as input an analog voltage, which determines the frequency of a square wave that it outputs. The input to the oscillator came from a circuit that produces a linear ramp signal. This signal varied linearly from one user-

adjustable voltage to another. The ramp itself was generated using a 555 timer chip. The time-variant current signal from the voltage controlled oscillator is amplified by a current amplifier before fed into the reader antenna. The main part of the current amplifier is the transistor.

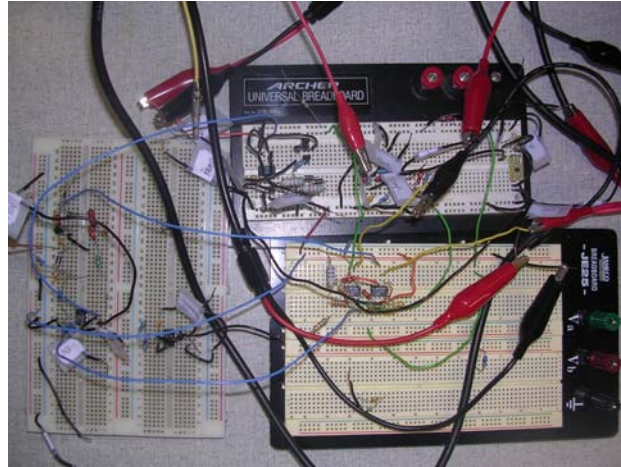


Figure 7.2 Prototype of the transmitter circuit.

7.3 Receiver

The voltage across the reader antenna is measured and integrated by Miller integrator which is mainly composed by an operational amplifier (op amp) which is one of the versatile electronic circuits. The voltage signal from the antenna is shown in Figure 7.3. This voltage signals then are sent to the Miller integrator. The output voltage signal is and integrated which is shown below.

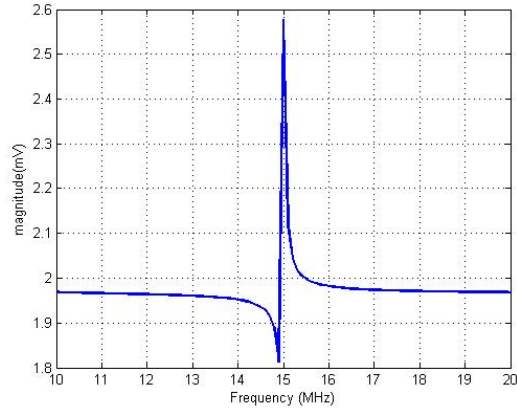


Figure 7.3 The output signal of the Miller integrator.

The signal after being amplified and integrated is easier to be analyzed and the resonant frequency of the sensor as well as the shifting of the resonant frequency because of the related strain can be easily determined by measuring the maximum value of the signal.

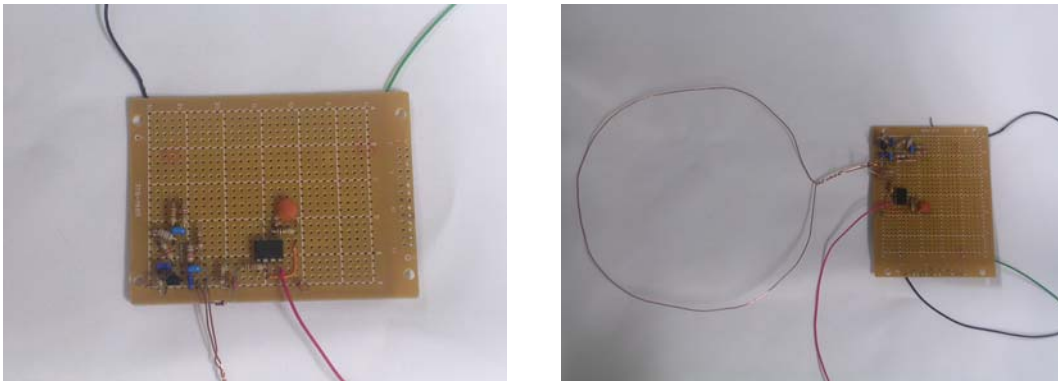


Figure 7.4 Fabricated current and voltage amplifier circuit with coil antenna.

7.4 Data Acquisition and Display

Integrated voltage signal from the Miller integrator is directly connected to the data acquisition board (Figure 7.5).



Figure 7.5 Data acquisition board.

Data display interface to communicate with the DAQ board in real-time is programmed in Matlab based on the data acquisition toolbox offered in Matlab. The frequency response of the voltage in the sweeping frequency range is displayed graphically and the resonant frequency of the sensor where the maximum magnitude of the voltage appears is shown.

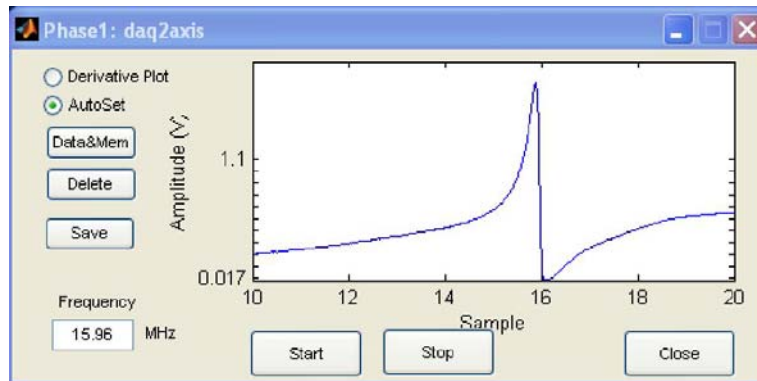


Figure 7.6 Data display interface programmed in MATLAB.

8 SENSOR CHARACTERIZATIONS

Several sensor prototypes were fabricated and installed on the cantilever beam with constant surface strain for strain measurement calibration and performance investigations. The proposed strain sensor is calibrated by standard strain gauge attached to the beam. Discussions are primarily provided based on abundant experimental results. This chapter starts with a brief description of the bending beam test setup. Strain measurement and sensor calibration will be discussed.

8.1 Loading System Setup

8.1.1 Beam Bending Behavior

Classical cantilever beam bending system will be utilized in the strain measurement setup and sensor calibration. Based on a simple parallel sided cantilever beam with a single localized load at the free end, the axial stress on the beam surface is proportional to the bending moment which can be expressed by

$$\sigma(x) = \frac{G(x) \cdot c}{J} = \frac{6Fx}{wh^2} = \frac{Fx}{Y} \quad 8.1$$

where $\sigma(x)$ is the bending stress on the beam surface in N/m^2 at a distance x from the point of the load application F in N, $G(x)$ is the bending moment at distance x in-lbs (mN), c is the distance from neutral axis to the beam surface in m, J is the moment of inertial of beam cross-section in m^4 , Y is the section modulus of beam in m^3 , w is the beam width in m and h is the beam thickness in m.

Apparently, the surface stress varies linearly from zero at the point of load application to a maximum at the clamped end, if the beam is parallel sided, so that the section modulus, Y , is constant. The surface of the cantilever beam is in a uniaxial stress state and therefore, from Hook's Law for this case,

$$\varepsilon(x) = \frac{\sigma(x)}{e} = \frac{Fx}{eY} \quad 8.2$$

The surface strain $\varepsilon(x)$ also varies linearly along the length of a straight, parallel sided cantilever beam.

8.1.2 Beam Design

The objective of the beam design is to eliminate the position effect on the strain measurement. A beam with constant surface strain is desired to be employed in the sensor characterization. Hence, it can be seen that, in order to get a uniform strain on the surface for any predetermined load, F , x is needed to vary from zero to l and the section modulus must vary directly with x , so that,

$$\frac{x}{Y(x)} = \frac{\sigma(x)}{w(x)[h(x)]^2} \quad 8.3$$

In other words, the width and/or thickness of the beam must be functions of x and vary along the beam. But a beam that varies in thickness is difficult and expensive to fabricate; it is more common to vary the width in order to achieve constant bending strain along the beam length. The section modulus can be made proportional to x by making the width proportional to x , and holding the thickness constant.

$$w(x) = Kx \quad 8.4$$

$$\varepsilon(x) = \frac{6Fx}{eKxh^2} = \frac{6F}{eKh^2} \quad 8.5$$

Thus, the strain is constant on the beam surface from one end of the beam to the other (except for localized effects in the vicinity of the loading point and the clamped end, which effects are not considered here). The constant-strain cantilever beam we have just designed is shown below

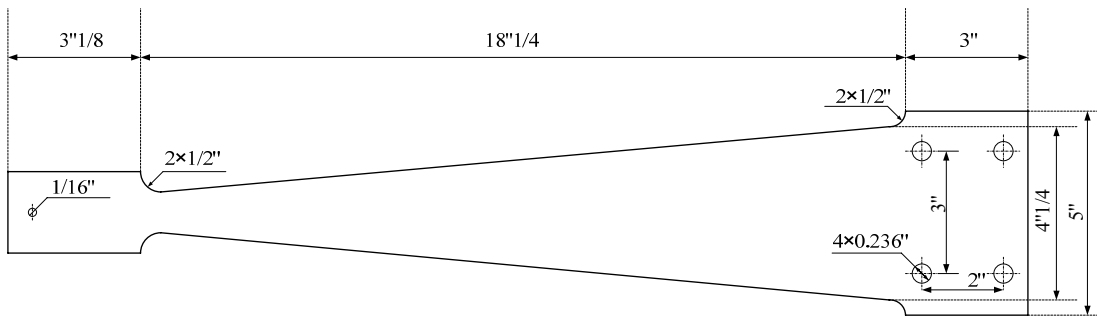


Figure 8.1 Test beam design.

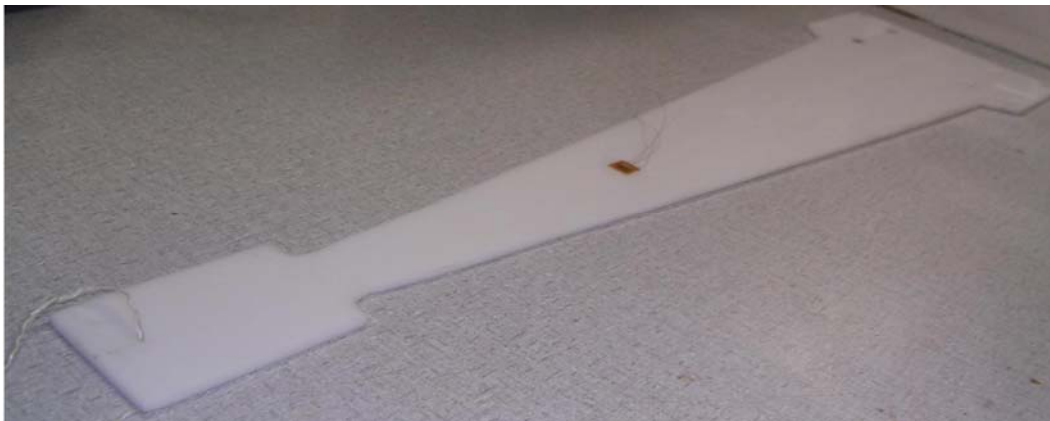


Figure 8.2 White Delrin beam with position independent surface strain.

8.1.3 Bending Test Setup

Fabricated beam with a position-independent surface strain with a clamped end and a free end applied load is shown in the Figure 8.3 below.



Figure 8.3 Sensor calibration setup.

Proposed passive wireless sensor and strain gage for calibration are attached to the beam by special adhesive for strain measurement. Sensor reader separated by a certain distance for wireless data communication and remote power is placed right above the sensor (Figure 8.4).

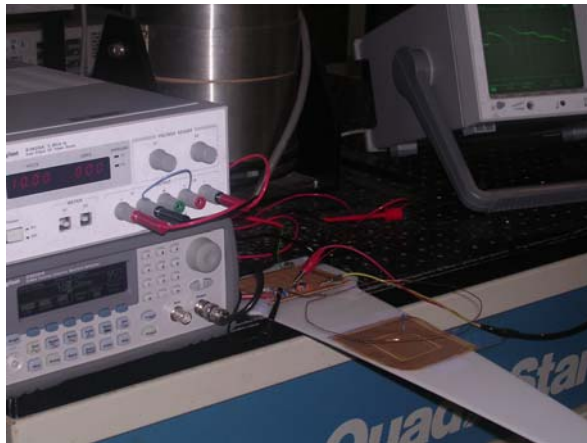


Figure 8.4 Sensor calibration setup.

Weights are applied to the free end of the constant-strain beam. In order to eliminate the influence of the self-weight and small plastic deformation in the beam, instead of using weight for the calibration, strain gauges are employed in the test. Related experimental results and system characterization are shown in the next section.

8.2 Sensor Performances Characterization

8.2.1 Distance and Angle vs. Resonant Frequency

Firstly, during the deformation of the beam, the sensor is getting far away from the center of the reader antenna and the relative angle between the reader antenna and the sensor is changing from parallel to a certain angle. These influences of the relative position of the sensor and reader antenna are studied.

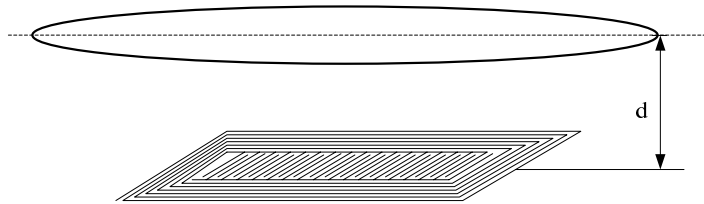


Figure 8.5 Sketch for distance and resonant frequency investigation.

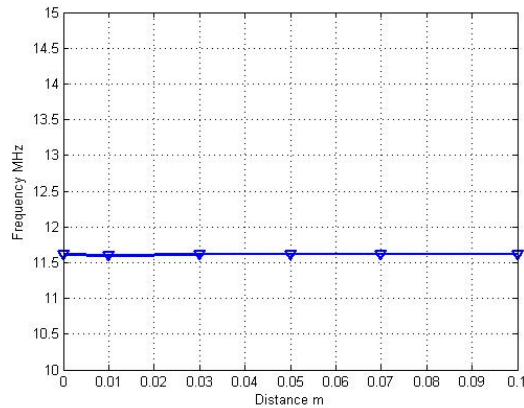


Figure 8.6 Distance vs. resonant frequency.

It can be seen that the varying distance does not change the frequency measurement but the signal strength. The reader offers a maximum interrogation distance up to 11 cm.

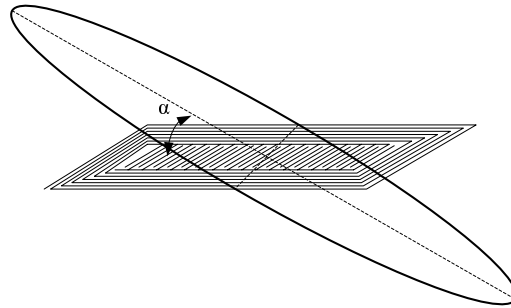


Figure 8.7 Sketch for angle and resonant frequency investigation.

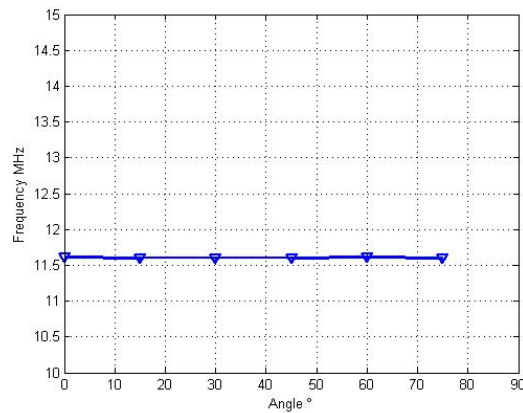


Figure 8.8 Angle vs. resonant frequency.

The center of the reader antenna keeps on the center of the sensor during the angle change. It is shown that the relative angle of the sensor and reader antenna does not change the measured resonant frequency but the magnitude of which at angle $\alpha=90^\circ$, the magnitude gets to almost zero.

8.2.2 Strain vs. Resonant Frequency

The strain and resonant frequency was measured in three cases as indicated in section 3.1.3 shown in Figure 3.6. These three cases are indexed by the relative direction of the IDE fingers and the surface strain, which include parallel, perpendicular and random angle directions.

1. Parallel direction

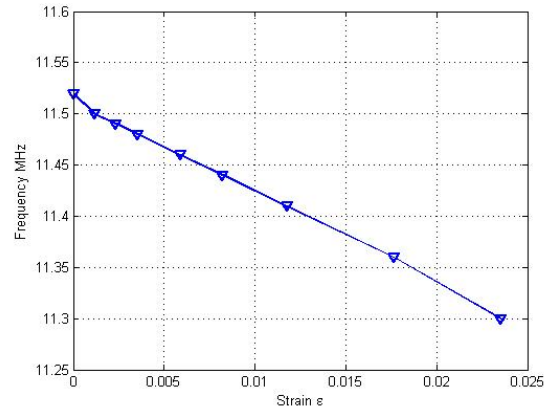


Figure 8.9 Frequency shift vs. surface strain with sensor at parallel direction.

2. Perpendicular direction

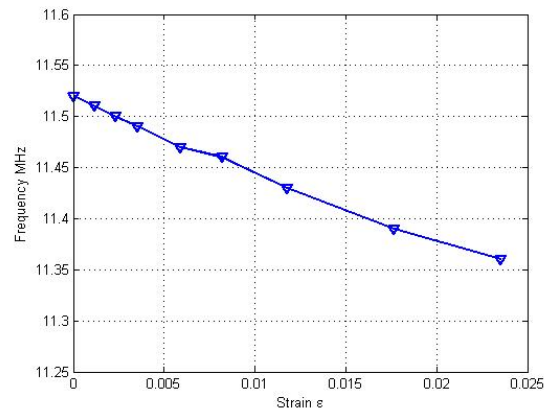


Figure 8.10 Frequency shift vs. surface strain with sensor at perpendicular direction.

2. Random angle direction

These above results are measured without strain sensitive material attached to the sensor. This is because the wavelength of the interdigital capacitor is a lot greater than the thickness of the PVDF material, which makes the capacitance in PVDF layer play a very insignificant role in the total capacitance.

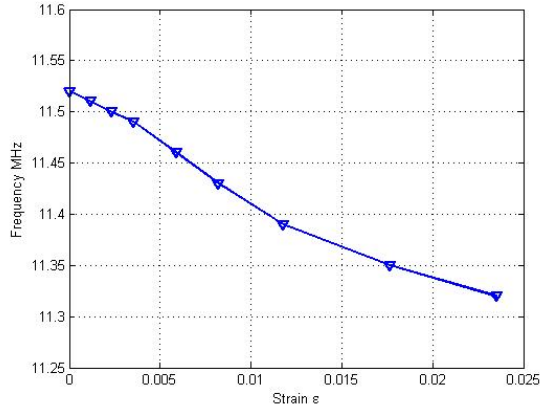


Figure 8.11 Frequency shift vs. surface strain with sensor at 45°.

8.2.3 Environment Related Effects

Although the sensor is designed at a specific resonant frequency, this resonant frequency can be slightly changed due to the flexible substrate and different dielectric permittivity of the attached material under test. Therefore, sensors should be calibrated by measuring the initial resonant frequency. Furthermore, humidity and temperature should also be highly considered if the strain sensitive material is attached. This is because the piezoelectric material is always pyroelectric materials with properties of humidity absorption as we demonstrated in Chapter 5. In this case, reference sensors are needed to extract strain information from complicated disturbances. This is simply realized by subtract the signal of the on-site sensor and the reference sensors to eliminate temperature and humidity effects. Of course, the reference sensors have exactly the same structure configurations and also attached to the same materials but undeformed within the same environments, which is the most critical parts of the calibration. The inductive coupling suffers the same restrictions such as the occlusion and presence of metal. Therefore, the sensor can only be attached to composite materials, wood, plastics except metal.

9 CONCLUSIONS REMARKINGS

9.1 Brief Thesis Summary

In this thesis, various current modern strain sensing techniques based on different physical principles, such as piezoresistive, piezoelectric, piezo-optical and etc., have been widely reviewed. Among these techniques, examples of wireless sensing techniques have been briefly discussed and principles used for wireless sensing are compared. The wireless strain sensor based on thick film planar resonator using inductive coupling is proposed. The strain effects on the resonant frequency of the sensor have been deeply explored by carrying out solving analytical solutions and simulations in finite element solvers. Furthermore, strain-dependent dielectric permittivity in piezoelectric polymer (PVDF) was investigated both theoretically and experimentally. In order to optimize the sensing performances, geometric optimizations were executed to search for the best configuration of a minimized sensor size, maximized sensing distance, maximized Q factor and maximized strain sensitivity. Nonlinear programming was carried out based on Multi-objective methods. Sensor prototypes based on our optimization results were successfully fabricated in our lab to prove the concept of strain sensing and wireless communication. Wireless reader, which acts like a transmitter for activating the sensor and a receiver for receiving strain information, was designed and constructed. Computer program to process the data in real time to monitor the strain state was made in MATLAB. A friendly graphic interface was also developed. Fabricated sensors were attached to a cantilever beam with position-independent strain. Meanwhile, strain gauges were utilized to calibrate the proposed wireless sensor. The results of calibration on a

cantilever beam with position-independent surface strain showed a great linearity and sensitivity.

9.2 Research Contributions

During this one year and a half thesis work, primary goals of this research have been successfully achieved, which can be simply concluded below.

- An innovative wireless strain sensing mechanism based on a thick film LC resonant circuit has been successfully developed;
- Prototypes of proposed sensors and associated electronics has been designed, optimized and fabricated;
- The sensor prototypes have been characterized and calibrated to prove the concept of sensing and wireless communication.

Specifically, the contributions of this research made to the community include:

First of all, the strain effect in planar resonator has been fully investigated which disclosed a new potential application of the planar resonator to the strain sensing field in nondestructive evaluation, structure health monitoring, damage detection, and failure prevention. These passive strain sensors can be fabricated at a low-cost (no more than 50 cents) so that they are able to be widely embedded in to structures or devices to monitoring a large area and also critical points. The wireless measurement results of the prototype sensor show a great linearity and sensitivity. The proposed strain sensor provides a simple planar

structure and a stable accurate strain measurement with a wireless and powerless feature, which enables a long-term embedded strain detection and integrated wireless communication.

Secondly, functions of strain sensitive materials have been discussed generally in many previous literatures. However, neither basic theoretical nor experimental supports have been discovered within our efforts. A network analyzer and transmission line method were employed to study the strain, temperature, and frequency dependence of the dielectric constant by measuring the S-parameters of a thin transmission line built on the PVDF film. The rotational dipoles offer information for the understanding of the temperature and strain behavior of the poled PVDF film by the linear relationship between the polarization and strain (and temperature). At the same time, PVDF film shows a great stability when the strain field was released and most of the polarization returns to the original direction by giving the original dielectric constant. Actually, the tensile strain and temperature dependence $\varepsilon(\tau, T, f)$ is dominated by the strain and temperature dependence polarization. The applications of the piezo- and pyro- dielectric properties of poled PVDF will be extended to the design of solid-state capacitance sensing and power-harvesting system etc.

Thirdly, planar resonators comprised of an interdigital capacitor and a spiral planar coil has been utilized in various wireless sensing schemes. However, no sensor design techniques or considerations have been mentioned in previous literatures. The effective design of planar resonators for wireless sensing applications requires an efficient optimization process to obtain a geometry that optimizes the application requirements. We have developed an optimization model, based on a weighted vector technique and penalty function, to harmonize the often conflicting objectives: minimize the sensor size, maximize the detection distance, maximize the quality factor, and maximize the strain sensitivity for the passive

wireless sensing. Through the selection of weighted vector, the single or multi-objective optimization is realized to get a rapid configuration to the geometric variables of planar resonator. The technique can provide designers with a systematic and efficient approach to achieve the optimization of the device based on the application requirements.

9.3 Future Works and Recommendations

There are couples of researches can be extended as future works, which can be concluded as the followings:

- Because of the limited resolution of our fabrication facilities, the sensor prototype used in our experiments is just a big version. In order to investigate the performances of this minimized sensor with strain sensitive material, such as the sensitivity, dynamic range, linearity and etc, the minimized sensor less than 10 mm with feature size no more than 50 μm has to be fabricated.
- In order to eliminate the environment effects, such as temperature and humidity, we proposed one possible solution that is to use exactly the same sensor attached to the same materials exposed to the same environment. Simplification can be made by connecting a series of some parallel connected interdigital capacitors to one single spiral inductor. Thus, monitoring a series of resonant frequencies through one reader antenna and processing circuits, environment effects can be efficiently eliminated.
- In order to measure strain in metal materials, we can disassemble the interdigital capacitor from the spiral inductor and embed it into the metal materials while place the

inductor outside the metal shield. In this way, the strain measurement would not be constrained by the method of inductive powering and communication.

- Low-cost minimized sensor tags can be fabricated in a large amount and embedded into structures or devices to form a sensor network, in which each of the sensor nodes are basically identified by their inherent resonant frequencies. Sensors can be used to measure various measurands simultaneously, for example, chemical gas, humidity, temperature, strain and stress, and acceleration, etc. Relatively big antenna at a portable reader with microprocessors for data processing should be fabricated.

References

- [1]. Klaus Bethe, "The Scope of The Strain Gage Principle", *VLSI and Microelectronic Applications in Intelligent peripherals and their Interconnection Networks Proceedings*, pp.31-38, May 1989.
- [2]. N. M. White and J. D. Turner, "Thick Film Sensors: Past, Present and Future", *Meas. Sci. Technol.*, vol.8, pp.1-20, 1997.
- [3]. K. I. Arshak, F. Ansari, D. McDonagh and D. Collins, "Development of a Novel Thick-film Strain Gauge Sensor System", *Meas. Sci. Technol.*, vol.8, pp.58-70, 1997.
- [4]. Lisa C. Martin, John D. Wrbanek, and Gustave C. Fralick, "Thin Film Sensors for Surface Measurements", *NASA/TM-2001-211149*, 2001.
- [5]. Jih-Fen Lei, Lisa C. Martin and Herbert A. Will, "Advances in Thin Film Sensor Technologies for Engine Applications", *NASA Technical Memorandum 107410*, June 1997.
- [6]. Jih-Fen Lei and Herbert A. Will, "Thin-Film Thermocouples and Strain-Gauge Technologies for Engine Applications", *Sensors and Actuators A*, pp.187-193, 1998.
- [7]. F. Löffler, C. Sievert, and C. Ascher, "Manganin Thin Film Sensor for Force Sensing", *Surface and Coating Technology*, Elsevier Science, pp.1287-1292, 2003.
- [8]. Hany R. Tamim and Horacio V. Estrada, "Temperature Dependence of In-Doped Silicon Strain Gages", *IEEE Proceedings of Southeastcon*, vol.2, pp.1101-1105, April 1991.
- [9]. L. Que, M.-H. Li, L. L. Chu and Y. B. Gianchandani, "A Micromachined Strain Sensor with Differential Capacitive Readout", *IEEE International Conference on MicroElectroMechanical Systems*, pp.552-557, January 1999.
- [10]. Michael Suster, Jun Guo, Nattapon Chaimanonart, Wen H. Ko, and Darrin J. Young, "Low-Noise CMOS Integrated Sensing Electronics for Capacitive MEMS Strain Sensors", *IEEE Custom Integrated Circuits Conference*, pp.693-696, October 2004.
- [11]. John C. Butler, Anthony J. Vigliotti, Fred W. Verdi and Shawn M. Walsh, "Wireless, Passive, Resonant-Circuit, Inductively Coupled Inductive Strain Sensor", *Sensors and Actuators A*, vol.102, pp.61-66, 2002.
- [12]. IEEE Standard on Magnetostrictive Materials: Piezomagnetic Nomenclature (Revision of IEEE Std 319-1971), *IEEE Std 319*, 1990..
- [13]. Dimitris Kouzoudis and Craig A Grimes, "The Frequency Response of Magnetoelastic Sensor to Stress and Atmospheric Pressure", *Smart Materials and Structures*, vol.9, pp.1-5, 2000.
- [14]. D. Erts, B. Polyakov, E. Saks, H. Olin, L. Ryen, K. Ziegler, and J. D. Holmes, "Semiconducting nanowires: properties and architectures", *Solid State Phenomena*, vol.99-100, pp.109-116, 2004.
- [15]. Chun-Yu Li and Tsu-Wei Chou, "Strain and pressure sensing using single-walled carbon nanotubes", *Nanotechnology*, vol.15, pp.1493-1496, 2004.
- [16]. J. Chuang, D. J. Thomson, G. Bridges, "Wireless strain sensor based on resonant RF cavities", *Smart Structure and Materials, Proc. of SPIE*, vol.5390, pp.574-584, 2004.
- [17]. Y. Zhou, R. M. C. So, W. Jin, H. G. Xu and P. K. C. Chan, "Dynamic Strain Measurements of a Circular Cylinder in a Cross Flow using a Fibre Bragg grating Sensor", *Experiments in Fluids*, vol.27, pp.359-367, 1999.
- [18]. P. Choquet, F. Juneau and F. Dadoun, "New Generation of Fiber-Optic Sensor for Dam Monitoring", *Proceedings of the International Conference on Dam Safety and Monitoring*, October 1999.

- [19]. David A. Hare and Thomas C. Moore, "Characteristics of Extrinsic Fabry-Perot Interferometric (EFPI) Fiber-Optic Strain Gages", *NASA/TP-210639*, December 2000.
- [20]. Tuan A. Tran, William V. Miller III, Kent A. Murphy, Ashish M. Vengsarkar and Richard O. Claus, "Stabilized Extrinsic Fiber-Optic Fizeau Sensor for Surface Acoustic Wave Detection", *Journal of Lightwave Technology*, vol.10, No.10, pp.1499-1506, October 1992.
- [21]. Y. J. Rao, C. X. Zhou, and T. Zhu, "SFDM/CWDM of Fiber-Optic Fizeau Strain Sensors", *IEEE Photonics Technology Letters*, vol.7, No.6, pp. 1259-1261, June 2005.
- [22]. Chin-Yi Liaw, Yan Zhou, and Yee-Loy Lam, "Theory of an Amplified Closed-Sagnac-Loop Interferometric Fiber-Optic Gyroscope", *IEEE Journal of Quantum Electronics*, vol.35, No.12, pp.1777-1785, December 1999.
- [23]. Yan Han, Qun Li, Xiaoming Liu, and Bingkun Zhou, "Architecture of High-Order All-Fiber Birefringent Filters by the Use of the Sagnac Interferometer", *IEEE Photonics Technology Letters*, vol.11, No.1, pp.90-92, January 1999.
- [24]. Gang Chen, Jiu U. Kang, and Jacob B. Khurgin, "Frequency discriminator Based on Ring-Assisted Fiber Sagnac Filter", *IEEE Photonics Technology Letters*, vol.17, No.1, pp.109-111, January 2005.
- [25]. Stephanus J. Spammer, Pieter L. Swart and Anatoli A. Chtcherbakov, "Merged Sagnac-Michelson Interferometer for Distributed Disturbance Detection", *Journal of Lightwave Technology*, vol.15, No.6, pp.972-976, June 1997.
- [26]. Eric Udd, "Sagnac Distributed Sensor", *United States Patent*, US 4898468, February 1990.
- [27]. G. Vendroux and W. G. Knauss, "Submicron Deformation Field Measurements: Part 2. Improved Digital Image Correlation", *Experimental Mechanics*, vol.38, No.2, pp.86-92, June 1998.
- [28]. David W. Manthey and Daeyong Lee, "Vision-Based Surface Strain Measurement System", *Journal of the Minerals, Metals & Materials Society*, vol.47, No.7, pp.46-49, 1995.
- [29]. James P. Hubner, Peter G. Ifju, Kirk S. Schanze, David A. Jenkins, Bruce F. Carroll, Yingsheng Wang, Phillip He, Anthony Brennan and Wissam El-Ratal, "Full-field strain measurement using a Luminescent coating", *Society for Experimental Mechanics*, vol.43, No.1, pp.61-68, March 2003.
- [30]. Fabiano Fruett, "Piezjunction Effect in Silicon, its consequences and Applications for Integrated Circuits and Sensors", Master's thesis, September 2001.
- [31]. Li Cao, Tae Song Kim, Susan C. Mantell, and Dennis L. Polla, "Simulation and Fabrication of Piezoresistive Membrane Type MEMS Strain Sensors", *Sensors and Actuators*, vol.80, pp.273-279, 2000.
- [32]. A. V. Mamishev, K. S. Rajan, Y. Du and M. Zahn, "Interdigital Sensors and Transducers", *Proceedings of the IEEE*, vol.92, No.5, pp.808-845, May 2004.
- [33]. E. Endres and S. Drost, "Optimization of the geometry of gas-sensitive interdigital capacitors", *Sensors and Actuators B: Chemical*, vol.4, pp.95-98, May 1991.
- [34]. Rui Igreja and C. J. Dias, "Analytical Evaluation of the Interdigital Electrodes Capacitance for a Multi-Layered Structure", *Sensors and Actuators A*, vol.112, pp.291-301, January 2004.
- [35]. Toru Ueno, Kazuya Mori, and Tetsuo Yoshida, "Capacitive Strain Sensors and Method for Using the Same", *United States Patent*, No.US6532824B1, March 2003.
- [36]. Klaus Finkenzeller, *RFID Handbook*, 2nd Ed., John Wiley & Sons, 2003.
- [37]. Diana S. Young, "Wireless Sensor System for Measurement of Violin Bowing Parameters", *Proceedings of the Stockholm Music Acoustics Conference*, pp.111-114, August 2003.
- [38]. Seth Edward-Austin Hollar, "COTS Dust", Master's thesis, University of California, Berkeley, 2000.

- [39]. Brett Warneke, Matt Last, Brian Leibowitz, and Kristofer S.J. Pister, "Smart Dust: Communicating with a Cubic-Millimeter Computer", *IEEE Computer*, vol.34, No.1, pp.44-51, January 2003.
- [40]. <http://sensorwebs.jpl.nasa.gov/>
- [41]. Joseph Polastre, Robert Szewczyk, and David Culler, "Telos: Enabling Ultra-low Power Wireless Research", *IPSN*, pp.364-369, April 2005.
- [42]. W.Ye, J. Heidermann, and D. Estrin, "An Energy-Efficient MAC Protocol for Wireless Sensor Networks", *in Proc. IEEE INFOCOM*, vol.3, pp.1567-1576, 2002.
- [43]. Gernot Schimetta, Franz Dollinger, and Robert Weigel, "A Wireless Pressure-Measurement System Using a SAW Hybrid Sensor", *IEEE Transactions on Microwave Theory and Techniques*, vol.48, No.12, pp.2730-2735, December 2000.
- [44]. Alfred Pohl, "A Review of Wireless SAW Sensors", *IEEE Transactions on Ultrasonics, Ferroelectrics, and Frequency Control*, vol.47, No.2, pp.317-332, March 2000.
- [45]. Matthai Philipose, Joshua R. Smith, Bing Jiang, Alexander Mamishev, and Sumit Roy, "Battery-Free Wireless Identification and Sensing", *IEEE Pervasive Computing*, vol.4, No.1, pp.37-45, March 2005.
- [46]. Olivier Chevalerias, Terence O'Donnell, Daithí Power, Neil O'Donovan, Gerald Duffy, Gary Grant, and Seán Cian O'Mathuna, "Inductive Telemetry of Multiple Sensor Modules", *IEEE Pervasive Computing*, vol.4, No.1, pp.46-52, March 2005.
- [47]. Sunderarajan S. Mohan, Maria del Mar Hershenson, Stephen P. Boyd, and Thomas H. Lee, "Simple Accurate Expression for Planar Spiral Inductances", *IEEE Journal of Solid-State Circuits*, vol.34, No.10, pp.1419-1424, October 1999.
- [48]. C. Patrick Yue and S. Simon Wong, "Physical Modeling of Spiral Inductors on Silicon", *IEEE Transactions on Electron Devices*, vol.47, No.3, pp.560-567, March 2000.
- [49]. H. E. Bryan, "Printed Inductors and Capacitors", *Tele-Tech. Electron. Industries*, vol.14, pp.68-69, 1954.
- [50]. EN300330: Radio Equipment and systems; short range devices, technical characteristics and test methods for radio equipment in the frequency range 9 KHz to 25 MHz and inductive loop systems in the frequency range 9 KHz to 30 MHz.
- [51]. Federal communications commission, Office of Engineering and Technology Rules Part 15: Radio Frequency Devices.
- [52]. Kalyanmoy Deb, *Multi-Objective Optimization using Evolutionary Algorithms*, Wiley, New York.
- [53]. T.O'Donnell, O.Chevalerais, G. Grant, and S.C.O'Mathuna, "Inductive Powering of Sensor Modules", *20th Annual IEEE on Applied Power Electronics Conference and Exposition*, vol.3, pp.2024-2029, March 2005.
- [54]. Surya Musunuri, Patrick L. Chapman, Jun Zou, and Chang Liu, "Design Issues for Monolithic DC-DC Converters", *IEEE Transactions on Power Electronics*, vol.20, No.3, pp.639-649, May 2005.
- [55]. J. S. Harrison and Z. Ounaies, "Piezoelectric Polymers", *ICASE Report*, NASA/CR-2001-211422.
- [56]. William R. Eisenstadt, and Yungseon Eo, "S-Parameter-Based IC Interconnect Transmission Line Characterization", *IEEE Transactions on Components, Hybrids, and Manufacturing Technology*, vol.15, No.4, pp.483-490, August 1992.
- [57]. Mark C. Zaretsky, Lama Mouayad and James R. Melcher, "Continuum Properties from Interdigital Electrode Dielectrometry", *IEEE Transactions on Electrical Insulation*, vol.23, No.6, pp.897-917, December 1988.

- [58]. A. V. Mamishev, B. C. Lesieutre and M. Zahn, "Optimization of Multi-Wavelength Interdigital Dielectrometry Instrumentation and Algorithms", *IEEE Transactions on Dielectrics and Electrical Insulation*, vol.5, No.3, pp.408-420, June 1998.
- [59]. B. C. Lesieutre, A. V. Mamishev, Y. Du, E. Keskiner, M. Zahn and G. C. Verghese, "Forward and Inverse Parameter Estimation Algorithms of Interdigital Dielectrometry Sensors", *IEEE Transactions on Dielectrics and Electrical Insulation*, vol.8, No.4, pp.577-588, August 2001.
- [60]. A. V. Mamishev, A. R. Takahashi, Y. Du, B. C. Lesieutre and M. Zahn, "Parameter Estimation in Dielectrometry Measurements", *Journal of Electrostatics*, vol.56, pp.465-492, February 2002.
- [61]. A. V. Mamishev, A. R. Takahashi, Y. Du, B. C. Lesieutre and M. Zahn, "Assessment of Performance of Fringing Electric Field Sensor Arrays", *Annual Report Conference on Electrical Insulation and Dielectric Phenomena*, pp.918-921, October 2002.
- [62]. A. V. Mamishev, S. R. Cantrell, Y. Du, B. C. Lesieutre and M. Zahn, "Uncertainty in Multiple Penetration Depth Fringing Electric Field Sensor Measurements", *IEEE Transactions on Instrumentation and Measurement*, vol.51, No.6, pp.1192-1199, December 2002.
- [63]. A. V. Mamishev, K. S. Rajan, Y. Du and M. Zahn, "Interdigital Sensors and Transducers", *Proceedings of the IEEE*, vol.92, No.5, pp.808-845, May 2004.
- [64]. Bing Jiang and A. V. Mamishev, "Robotic Monitoring of Power Systems", *IEEE Transactions on Power Delivery*, vol.19, No.3, pp.912-918, July 2004.
- [65]. [Http://www.zeusinc.com/nesletter/dielectric.html](http://www.zeusinc.com/nesletter/dielectric.html)
- [66]. H. von Seggern and S. Fedosov, "Conductivity Induced Polarization in a Semicrystalline Ferroelectric Polymer", *IEEE Transaction on Dielectrics and Electrical Insulation*, Vol.11, pp.232-241, April 2004.

APPENDIX A. PROGRAM FOR PERMITTIVITY CALCULATION

```

% The following program extract the characteristic impedance and effective permittivity of a microstrip
% line using the S-parameters
S = []; %S-parameter's input from excel
% we assigned the S-parameters matrix values to the individual parameters
f=S(:,1); % frequency%
% M11=S(:,2);O11=S(:,3); % Magnitude and phase of S11
% M12=S(:,6);O12=S(:,7); % Magnitude and phase of S12
% M21=S(:,4);O21=S(:,5); % Magnitude and phase of S21
% M22=S(:,8);O22=S(:,9); % Magnitude and phase of S22

% we convert them to rectangular format
S11=S(:,2)+1i*S(:,3);
S21=S(:,4)+1i*S(:,5);
S12=S(:,6)+1i*S(:,7);
S22=S(:,8)+1i*S(:,9);
%S11=M11.*(cos(O11*pi/180)+1i.*sin(O11*pi/180));
% S12=M12.*(cos(O12*pi/180)+1i.*sin(O12*pi/180));
% S21=M21.*(cos(O21*pi/180)+1i.*sin(O21*pi/180));
% S22=M22.*(cos(O22*pi/180)+1i.*sin(O22*pi/180));

% we compute the K factor
K=((S11.^2-S21.^2+1).^2-(2*S11).^2)/(2*S21).^2).^0.5; % we compute the K factor
Zo=50; % reference impedance

% we compute the characteristic impedance
Z=(Zo^2*((1+S11).^2-S21.^2)/((1-S11).^2-S21.^2)).^0.5;

% we compute the equation 2.44
exp_gamma_lp=((1-S11.^2+S21.^2)/(2*S21)+K).^(-1); % for K positive
exp_gamma_ln=((1-S11.^2+S21.^2)/(2*S21)-K).^(-1); % for K negative
l=25e-3+0e-3; % line length of probe
w=2e-3;
d=110e-6;

% we compute the phase constant (gamma)
gamma_p=-log(exp_gamma_lp)/l; % for K positive
gamma_n=-log(exp_gamma_ln)/l; % for K negative
beta=abs(imag(gamma_p));
alpha=real(gamma_p);
% beta=zeros(length(gamma),1);
% beta(1)=(gamma(1));
% for i=2:1:length(gamma),
% if (gamma(i) < (gamma(i-1))),
% beta(i)=2*max((gamma))-gamma(i));
% else
% if beta(i-1) > max(gamma),
% beta(i)=2*max((gamma))+gamma(i));
% else
% %if imag(gamma(i)) > imag(gamma(i-1)),
% beta(i)=(gamma(i));
% end

```

```
% end
% end
lamda0=3e8./f; % wavelength in the free space
lamdag=2*pi./beta; % wavelength in the substrate

% we compute the effective permittivity of the set
perm_rel=(lamda0./lamdag).^2;
q=1/(1+12*d/w)^0.5;
er=(2*perm_rel-(1-q))/(1+q)
```

APPENDIX B PROGRAMS FOR SENSOR OPTIMIZATION

```

%This program gives all the objective functions and related knowns.
function f = multioptimization(x)
%Minimize sensor geometric demension
miu = pi*4e-7;
Rr = 75e-3;
Nr = 1;
f0 = 15e6;
w0 = 2*pi*f0;
f = 14e6;
w = 2*pi*f;
I1 = 1.1685;
K1 = 2.34; K2 = 2.75;
% tao = 600,%conductivity
% skindepth = sqrt(2/(w*mu*tao));%skindepth
t = 18e-6;%turn thickness
xx = 0.1;%separate distance
Rs = 0.04;
Rt = 2.5;
miu = pi*4e-7;
f0 = 19e6;
K1 = 2.34; K2 = 2.75;
weightedvector = [0.97, 0.00, 0.0, 0.03];
f = weightedvector*[x(1)+2*x(2)*(x(4)-1)+2*x(3)*x(4);...
    -miu*Nr*w*I1*(x(1)+x(2)*(x(4)-1)+x(3)*x(4))^2*x(4)*Rr^2/(2*sqrt((Rr^2+xx^2)^3));...
    -2*pi*f0*K1*miu*x(4)^2*(x(1)+x(2)*(x(4)-1)+x(3)*x(4))^2/(x(1)+(K2+1)*...
    (x(2)*(x(4)-1)+x(3)*x(4)))/(Rs*((4*x(4)-2)*(x(1)+x(2)*x(4))/x(3)+...
    (2*x(4)-1)*(2*x(4)-4)+4*x(4)*Rt));...
    -x(7)/(x(6)+x(7))];

%This program gives the nonlinear constraints
%x = [d_in g_L w_L N_L L_C g_C w_C N_C];
%d_in = inner diamter of PSI
%g_L = gap of PSI
%N_L = turns of PSI
%L_C = length of IDC fingers
%g_C = gap of IDC
%w_C = finger width of IDC
%N_C = number of IDC fingers
function [c, ceq] = multioptimizationconfun(x)

%input
K1 = 2.34; K2 = 2.75;
miu = pi*4e-7;
f0 = 15e6;
er1 = 1;
er2 = 3;
e0 = 8.854e-12;
eta = x(7)/(x(6)+x(7));
k00 = sin(pi*eta/2);

```

```

k0 = sqrt(1-k00^2);
C1 = 1.27; C2 = 2.07; C3 = 0.18; C4 = 0.13;

% Nonlinear inequality constraints
c = [x(8)*(x(6)+x(7))-x(1);...
     x(1)+2*x(2)*(x(4)-1)+2*x(3)*x(4)-0.1006];
% ;...
% (K1*miu*x(4)^2*(x(1)+(x(2)+x(3))*x(4))^2/(x(1)+(K2+1)*(x(2)+x(3))*x(4))-10e-6

%set resonant frequency to 15MHz
% Nonlinear equality constraints
ceq = [K1*miu*x(4)^2*(x(1)+x(2)*(x(4)-1)+x(3)*x(4))^2/(x(1)+(K2+1)*(x(2)*(x(4)-1)+x(3)*x(4)))*...
       (0.5*e0*(er1+er2)*(x(8)-1)*x(5)*ellipke(abs(k00))/ellipke(abs(k0)))-...
       1/((2*pi*f0)^2);x(8)*(x(6)+x(7))-x(5)];

%f = 1/(2*pi*sqrt((K1*miu*x(4)^2*(x(1)+(x(2)+x(3))*x(4))^2/(x(1)+(K2+1)...
% *(x(2)+x(3))*x(4)))+(0.5*e0*(er1+er2)*(x(8)-1)*x(5)*ellipke(abs(k00))...
% /ellipke(abs(k0)))));

% ceq = [0.5*C1*miu*x(4)^2*(x(1)+x(3)*x(4)+x(2)*(x(4)-1))*(log(C2*(x(1)+x(3)*x(4)...
% +x(2)*(x(4)-1))/(x(3)*x(4)+x(2)*(x(4)-1))) + C3*(x(1)+x(3)*x(4)...
% +x(2)*(x(4)-1))/(x(3)*x(4)+x(2)*(x(4)-1)) + C4*((x(1)+x(3)*x(4)...
% +x(2)*(x(4)-1))/(x(3)*x(4)+x(2)*(x(4)-1))^2)*...
% (0.5*e0*(er1+er2)*(x(8)-1)*x(5)*ellipke(abs(k00))/ellipke(abs(k0)))-...
% 1/((2*pi*f0)^2);x(8)*(x(6)+x(7))-x(5)];

%This program gives all the linear constraints
x0 = [1 1 1 1 1 1 1 1];
options = optimset('LargeScale','off','TolFun',1e-8,...
                  'TolX',1e-4,'MaxFunEvals',1e6,'TolCon',100,'MaxIter',1e6);

%linear inequal constraints
A = [-1 0 0 0 0 0 0 0;...
     0 -1 0 0 0 0 0 0;...
     0 0 -1 0 0 0 0 0;...
     0 0 0 -1 0 0 0 0;...
     0 0 0 0 -1 0 0 0;...
     0 0 0 0 0 -1 0 0;...
     0 0 0 0 0 0 -1 0;...
     0 0 0 0 0 0 0 -1;...
     -1 0 0 0 1 4 4 0];
b = [0;-5e-5;-5e-5;-2;0;-5e-5;-5e-5;-4;0];
[x, fval] = ...
fmincon(@multioptimization,x0,A,b,[],[],[],[],@multioptimizationconfun,options)

```

APPENDIX C PROGRAMS FOR DATA DISPLAY INTERFACE

```
function varargout = daq2axis(varargin)

% DAQ2AXIS GUI is meant to serve as an example for MATLAB users in the Test & Measurement area
%
% DAQ2AXIS continuously displays data to an axis during a data
% acquisition session
%
% The products required to run DAQ2AXIS are:
%   MATLAB 6.5 (R13)
%   Data Acquisition Toolbox 2.2
%
% DAQ2AXIS contains the following components:
%   Push Button
%   Axis
%
% See also DAQ2AXISFIELD, DAQ2AXISFIELDPLAY, SOUNDRECORDERDEMO.

% Edit the above text to modify the response to help daq2axis

% Last Modified by GUIDE v2.5 14-Jun-2005 16:31:07

% Begin initialization code - DO NOT EDIT
gui_Singleton = 1;
gui_State = struct('gui_Name',    mfilename, ...
                  'gui_Singleton', gui_Singleton, ...
                  'gui_OpeningFcn', @daq2axis_OpeningFcn, ...
                  'gui_OutputFcn', @daq2axis_OutputFcn, ...
                  'gui_LayoutFcn', [] , ...
                  'gui_Callback', []);
if nargin & isstr(varargin{1})
    gui_State.gui_Callback = str2func(varargin{1});
end

if nargout
    [varargout{1:nargout}] = gui_mainfcn(gui_State, varargin{:});
else
    gui_mainfcn(gui_State, varargin{:});
end
% End initialization code - DO NOT EDIT

% --- Executes just before daq2axis is made visible.
function daq2axis_OpeningFcn(hObject, eventdata, handles, varargin)
% This function has no output args, see OutputFcn.
% hObject    handle to figure
% eventdata  reserved - to be defined in a future version of MATLAB
% handles    structure with handles and user data (see GUIDATA)
% varargin   command line arguments to daq2axis (see VARARGIN)
```

```

% Choose default command line output for daq2axis
handles.output = hObject;

% Preliminary GUI settings
set(hObject,'Renderer','Zbuffer','DoubleBuffer','on','BackingStore','on');

% Make sure that the DAQ toolbox is installed on the system
if ~exist([matlabroot '\toolbox\daq'],'dir')
    errordlg('You must have the Data Acquisition Toolbox installed to run this demo','Error','modal');
    return
end

% Create an analoginput object using the winsound adaptor
daq_object = analoginput('nidaq');
chan=addchannel(daq_object,[0 2]);
set(daq_object.Channel,'SensorRange',[-5 5]);
set(daq_object.Channel,'InputRange',[-10 10]);

% Initialize the axes for the data
num_samples = 1000;
axes(handles.axes);
plot_handle = plot([(10.00:10/(num_samples-1):20);(10.00:10/(num_samples-1):20)],zeros(num_samples,2));
axis([10 20 -10.0 10.0]);
ylabel('Amplitude (V)');xlabel('Sample');

% Update handles structure
handles.daq_object = daq_object;
handles.plot_handle = plot_handle;
handles.data_handle=handles.plot_handle;
handles.num_samples = num_samples;
handles.plot_memory = [];
%zeros(num_samples,1)
guidata(hObject,handles);

% Set some properties and the callback of the DAQ object:

%set(daq_object,'InputType','SingleEnded',...
% 'SampleRate',10000,...
% 'SamplesPerTrigger',inf,...
% 'SamplesAcquiredFcn',num_samples,...
% 'SamplesAcquiredFcn',{@update_plot,handles});
set(daq_object, 'InputType','SingleEnded');
set(daq_object, 'SampleRate', num_samples/0.1);
set(daq_object, 'SamplesPerTrigger', num_samples);
set(daq_object, 'TriggerChannel', daq_object.Channel(2));
set(daq_object, 'TriggerType', 'Software');
set(daq_object, 'TriggerCondition', 'Rising');
set(daq_object, 'TriggerConditionValue', 0.15);
set(daq_object, 'TriggerDelayUnits', 'Samples');
set(daq_object, 'TriggerRepeat',inf);
set(daq_object, 'SamplesAcquiredFcn',{@update_plot,handles});

% UIWAIT makes daq2axis wait for user response (see UIRESUME)

```

```

% uiwait(handles.figure1);

% --- Outputs from this function are returned to the command line.
function varargout = daq2axis_OutputFcn(hObject, eventdata, handles)
% varargout cell array for returning output args (see VARARGOUT);
% hObject handle to figure
% eventdata reserved - to be defined in a future version of MATLAB
% handles structure with handles and user data (see GUIDATA)

% Get default command line output from handles structure
varargout{1} = handles.output;

% --- Executes on button press in start.
function start_Callback(hObject, eventdata, handles)
% hObject handle to start (see GCBO)
% eventdata reserved - to be defined in a future version of MATLAB
% handles structure with handles and user data (see GUIDATA)
if(strcmp(handles.daq_object.running,'On'))
    return;
else
    start(handles.daq_object);
end

% --- Executes on button press in stop.
function stop_Callback(hObject, eventdata, handles)
% hObject handle to stop (see GCBO)
% eventdata reserved - to be defined in a future version of MATLAB
% handles structure with handles and user data (see GUIDATA)

stop(handles.daq_object);

% --- Executes on button press in close.
function close_Callback(hObject, eventdata, handles)
% hObject handle to close (see GCBO)
% eventdata reserved - to be defined in a future version of MATLAB
% handles structure with handles and user data (see GUIDATA)

% If the winsound object is running, stop it then delete and clear it
if(strcmp(handles.daq_object.running,'On'))
    stop(handles.daq_object);
end
delete(handles.daq_object);
clear handles.daq_object;

% Close the figure
delete(handles.figure1)

%%%%%%%%%%%%%%%%%%%%%%%%%%%%%%%%%%%%%%%%%%%%%%%%%%%%%%%%%%%%%%%%%%%%%%%%
%%%%%%%%%%%%%%%%%%%%%%%%%%%%%%%%%%%%%%%%%%%%%%%%%%%%%%%%%%%%%%%%%%%%%%%%
% --- Hand-written callback function for DAQ object

```

```

function update_plot(hObject, eventdata, handles)
% hObject handle to daq_object
% eventdata reserved - to be defined in a future version of MATLAB
% handles structure with handles and user data (see GUIDATA)

% Get the most recent data and set the plot data
data = getdata(handles.daq_object,handles.num_samples);
data_diff = diff(data);
if (get(handles.Derivative_plot,'Value') == 1),
    % radiobutton is pressed
    ga = max(-data(:,1))/max(data_diff(:,1));
    data(:,2) = [ga*data_diff(:,1); 0];
    data(:,1) = -data(:,1);
else
    % radiobutton is not pressed
    data(:,1) = -data(:,1);
    data(:,2) = 0;
end
[peek,pos] = max(data_diff(1:900,1));
frequency = (pos/get(handles.daq_object, 'SampleRate'))*10/0.1+10;
for i = 1:length(handles.plot_handle)
    set(handles.plot_handle(i),'YData',data(:,i))
end
set(handles.resonant_frequency,'String',frequency)
%handles.data_memory=data(:,1);
%set(handles.magnitude,'String',peek)

function resonant_frequency_Callback(hObject, eventdata, handles)
% hObject handle to resonant_frequency (see GCBO)
% eventdata reserved - to be defined in a future version of MATLAB
% handles structure with handles and user data (see GUIDATA)

% Hints: get(hObject,'String') returns contents of resonant_frequency as text
% str2double(get(hObject,'String')) returns contents of resonant_frequency as a double

% --- Executes during object creation, after setting all properties.
function resonant_frequency_CreateFcn(hObject, eventdata, handles)
% hObject handle to resonant_frequency (see GCBO)
% eventdata reserved - to be defined in a future version of MATLAB
% handles empty - handles not created until after all CreateFens called

% Hint: edit controls usually have a white background on Windows.
% See ISPC and COMPUTER.
if ispc && isequal(get(hObject,'BackgroundColor'), get(0,'defaultUicontrolBackgroundColor'))
    set(hObject,'BackgroundColor','white');
end

% --- Executes on button press in autosest.
function autosest_Callback(hObject, eventdata, handles)
% hObject handle to autosest (see GCBO)
% eventdata reserved - to be defined in a future version of MATLAB
% handles structure with handles and user data (see GUIDATA)

```

```

% Hint: get(hObject,'Value') returns toggle state of autoset
if (get(handles.autoset,'Value') == 1),
    if (strcmp(handles.daq_object.running,'Off'))
        return;
    else
        x = peekdata(handles.daq_object,handles.num_samples);
        ylower = min(-x(:,1));
        yupper = max(-x(:,1));

        % If Nans are returned base the limit off the other.
        if isnan(ylower) & isnan(yupper)
            ylower = -0.01;
            yupper = 0.01;
        elseif isnan(ylower)
            ylower = yupper - (abs(yupper)/2);
        elseif isnan(yupper)
            yupper = ylower + (abs(ylower)/2);
        end

        % Handle the case when the limits are equal.
        if ylower == yupper
            ylower = ylower - (abs(ylower)/2);
            yupper = yupper + (abs(yupper)/2);
        end

        % If they are still equal (if they both were zero).
        if ylower == yupper
            ylower = -0.01;
            yupper = 0.01;
        end
        set(handles.axes, 'YLim', [floor(ylower) ceil(yupper)],...
            'YTick', linspace(ylower, yupper, 11),...
            'YTickLabel', {num2str(ylower,2), ",", " ", ",",...
                ",", " ", num2str(yupper,2)});
    end
else
    ylower = -10;
    yupper = 10;
    set(handles.axes, 'YLim', [ylower yupper],...
        'YTick', linspace(ylower, yupper, 11),...
        'YTickLabel', {num2str(ylower,2), ",", " ", ",",...
            ",", " ", num2str(yupper,2)});
end
% --- Executes on button press in data_memoria.
function data_memoria_Callback(hObject, eventdata, handles)
% hObject handle to data_memoria (see GCBO)
% eventdata reserved - to be defined in a future version of MATLAB
% handles structure with handles and user data (see GUIDATA)
if(strcmp(handles.daq_object.running,'On'))
    set(gca,'NextPlot','add')
    plot_memory=plot([(10.00:10/(handles.num_samples-1):20)],get(handles.plot_handle(1),'YData'),'r');
    set(gca,'NextPlot','replace')
    handles.plot_memory=[handles.plot_memory; get(plot_memory,'YData')];
end

```

```

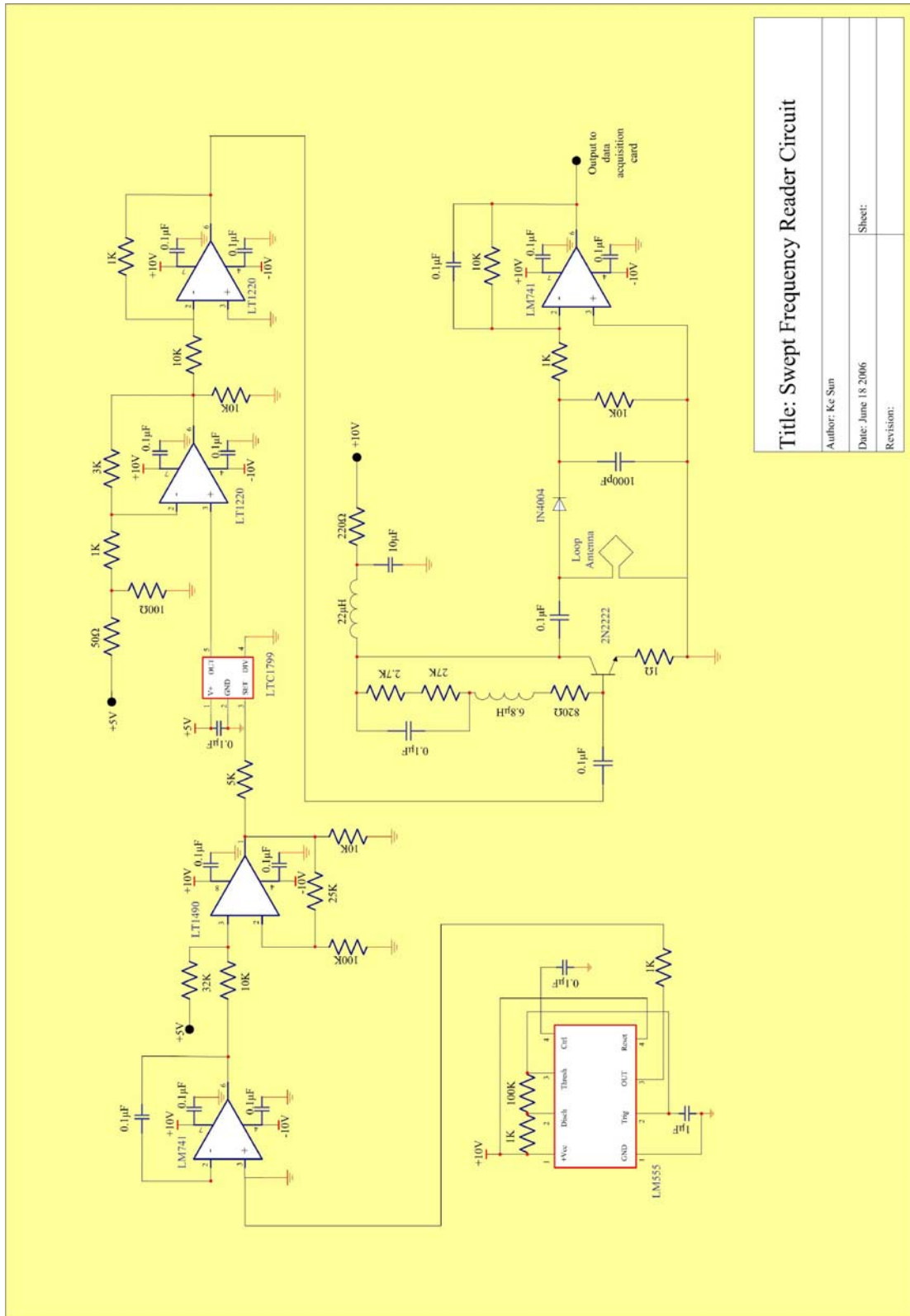
    %length(handles.plot_memory(:,1));
    guidata(hObject,handles);
end

% --- Executes on button press in memory_delete.
function memory_delete_Callback(hObject, eventdata, handles)
% hObject    handle to memory_delete (see GCBO)
% eventdata  reserved - to be defined in a future version of MATLAB
% handles    structure with handles and user data (see GUIDATA)
h = get(gca,'Children');
if length(h)>2
    delete(h(1));
    handles.plot_memory = [handles.plot_memory(1:((length(handles.plot_memory(:,1))-1)),:);];
else
    handles.plot_memory = [];
end
if (length(get(gca,'Children'))==2)
    handles.plot_memory = [];
end
guidata(hObject,handles);

% --- Executes on button press in save.
function save_Callback(hObject, eventdata, handles)
% hObject    handle to save (see GCBO)
% eventdata  reserved - to be defined in a future version of MATLAB
% handles    structure with handles and user data (see GUIDATA)
if (handles.plot_memory ~= 0)
    data_file = fopen('data.txt','w');
    A = mat2str(handles.plot_memory,5);
    fprintf(data_file,'Date = %11s;\n',date);
    fprintf(data_file,'d=%5s;\n',A);
    fclose(data_file);
end

```

APPENDIX D CIRCUIT DIAGRAM OF READER



Title: Swept Frequency Reader Circuit
 Author: Ke Sun
 Date: June 18, 2006
 Sheet:
 Revision:

